MULTI-SCALE EXPERIMENTS IN TURBULENT SUBCOOLED BOILING FLOW THROUGH A SQUARE CHANNEL WITH A SINGLE HEATED WALL

A Dissertation

by

CARLOS EDUARDO ESTRADA PÉREZ

Submitted to the Office of Graduate and Professional Studies of
Texas A&M University
in partial fulfillment of the requirements for the degree of

DOCTOR OF PHILOSOPHY

Chair of Committee,	Yassin A. Hassan
Committee Members,	Kalyan Annamalai
	William H. Marlow
	Sy-Bor Wen
Head of Department,	Andreas A. Polycarpou

December 2014

Major Subject: Mechanical Engineering

ABSTRACT

In this work, visualization experimental techniques that provide whole-field and multi-scale measurements of the liquid turbulence parameters, liquid and heater wall temperatures, and gas phase local parameters, were used to study subcooled boiling flow through a square channel. The explored visualization techniques were: 1) Particle tracking velocimetry (PTV), which provides velocity measurements of the liquid phase, 2) High-speed shadowgraphy (HSS) which is used to study the dispersed phase dynamics. 3) Laser induced fluorescence thermometry (LIF) to measure whole-field liquid temperature fields. 4) High-speed infrared thermometry (IR-T), to study the impact of the boiling level on the heated wall temperature. A series of sensitivity studies were performed with which, knowledge for the optimal implementation of each technique was gained. Identification and quantification of uncertainties allowed to optimize the experimental conditions to achieve reliable and accurate liquid velocity measurements with the PTV technique. New procedures were designed to measure the average bubble velocity, bubble size, and void fractions. The single-nucleation site experiments provided optimal characteristics for the study of the bubble and liquid dynamics by means of PTV-shadowgraphy technique. This experiment simplified the quantification of the relationship that exist between the vapor and liquid parameters. From these results, new relationships and correlations are proposed to describe the near-wall liquid velocity behavior depending on local two-phase flow parameters. For the LIF thermometry, sensitivity studies were performed to evaluate the effects of excitation wavelength, dyes concentration ratios, solution pH, and selected emission bands on the temperature sensitivity of the two-color two-dye LIF thermometry technique. Temperature sensitivities of about 4% per °C were obtained, which is

better than the traditionally used RhB-Rh60 solution which provides sensitivities of about 2% per °C. The present study is intended to lay down the experimental and data analysis foundations required to improve the understanding of subcooled flow boiling. This study also provides reliable and accurate experimental information for development and validation of two-phase flow computational models.

DEDICATION

To my parents Luis Estrada Martinez and Cecilia Perez de Estrada for their unconditional love and support, to my siblings Quique, Cecy and Jorge for their encouragement, and to my sweetheart Fabiola Rangel for her love, understanding and support.

To God through whom I had the knowledge and strength to accomplish his task.

ACKNOWLEDGEMENTS

Over the past years I have received support and encouragement from a great number of individuals to conclude my graduate studies. First, I would like to express my gratitude to my mentor, Dr. Yassin Hassan for his patience, guidance, and friendship. I would also like to thank my committee members, Drs. Kalyan Annamalai, William Marlow and Sy-Bor Wen for their suggestions and valuable insight to my research.

I also want to thank all my colleagues and friends for all their encouragement and insights during my time at Texas A&M.

Above all, I would like to thank God for all the blessings.

TABLE OF CONTENTS

LIST OF FIGURES

FIGURE Page

LIST OF TABLES

TABLE Page

1. INTRODUCTION

Subcooled flow boiling can be found in engineering systems that rely on its high heat transfer capacity. It is found in electronic cooling, nuclear and chemical reactors, heat exchangers, etc. In most practical applications, subcooled flow boiling is generally characterized to be highly turbulent, due in part, to the liquid mixing and stirring by the vapor bubbles during their life cycle. In this way, the vapor bubbles modify the local liquid transport properties, which in turn will change the bubbles behavior and flow regimes in regions downstream.

The understanding of the energy and momentum transfer mechanisms within typical boiling systems is required to determine equipment design practices and safety operational ranges to avoid excessive mechanical or thermal stresses. For example, in the nuclear industry, the void fraction, which is an important flow boiling parameter, is not only strongly linked with the system heat transfer and liquid turbulence, but also plays a key role on the modification of the neutrons moderation which in turn may impact the nuclear core reactivity, and may lead to instabilities at certain operational conditions.

Notwithstanding the importance of subcooled flow boiling for industry and research, most of the developed models in the subject, were based on results from point measurement probes that are either intrusive or lack spatial resolution. The complexity of the phenomena and the dependence on the experimental conditions have made it difficult to implement multi-scale and non-intrusive experimental techniques.

State-of-the-art measurement techniques are required to quantify momentum and heat transfer parameters that are important for the description of subcooled flow boiling. These measurement techniques have to provide information at the

different scales of interests. This to allow first, from the temporal point of view, measurements of long-lived parameters with high statistical significance, while also providing, at the same experimental conditions, information of the short lived or dynamic parameters. From the spatial point of view, the experimental scales can range from micro-scales typical of near-wall measurements to the macro-scales required to determine flow regimes development. Furthermore, parameters from both phases, liquid and vapor, have to be simultaneously measured to account for their interactions To tackle this experimental challenges, this work explores the feasible implementation of visualization techniques that can provide whole-field and multi-scale measurements of the liquid turbulence parameters, liquid and heater wall temperatures, and gas phase parameters.

The explored visualization techniques are: 1) Particle tracking velocimetry (PTV) to quantify the influence that boiling parameters have on the liquid phase turbulence statistics, 2) High-speed shadowgraphy with to study the gas phase dynamics. 3) Laser induced fluorescense thermoemtry (LIF) to measure whole-field liquid temperature fields. 4) High-speed infrared thermometry (IR-T), to study the impact of the boiling level on the heated wall temperature,

Each of these techniques are explored in depth so as to determine their applicability ranges, limitations and accuracy. A series of sensitivity studies were performed with which knowledge for the optimal implementation of each individual techniques was gained. Furthermore, the compatibility between techniques was also considered in order to perform subcooled boiling flow experiments without interference between the measuring techniques. The present study is intended to lay down the experimental and data analysis foundations required to improve the understanding of subcooled flow boiling, and to provide reliable and accurate experimental information for development and validation of two-phase flow computational models.

2. LITERATURE REVIEW

In this section, a review of the literature is presented, special interest is given to studies on which visualization techniques are implemented in similar conditions to those found in subcooled boiling flow. First, a summary of PTV experimental studies is presented, those on which PTV is applied on two-phase turbulent flows or those which focused on the uncertainty quantification of PTV are included. LIF articles that explain the basic principles and limitations of the technique are also presented, followed by a review of two-phase flow visualization experiments that use shadowgraphy technique. Finally some studies that compare visualization and point measurement techniques shed light into the limitations of each technique.

2.1 Particle Tracking Velocimetry

On visualization studies, the analysis of near-wall turbulent flow requires algorithms that efficiently track the tracer particles suspended in the fluid flow. This is especially important in the near-wall regions because image noise together with high velocity gradients decreases the accuracy of particle tracking algorithms. In the study of turbulent flows, the availability of high power laser sources together with fast digital processors led to quite important advances of sophisticated whole field velocimetry techniques such as Particle Image Velocimetry (PIV) and Particle Tracking Velocimetry (PTV). These techniques are non-intrusive, full-field flow visualization techniques that provide quantitative and qualitative information of the flow under study with high accuracy and spatial resolution. The common measuring principle behind these methods is that instantaneous fluid velocities can be evaluated by recording the position of images produced by small tracers suspended in the fluid,

at successive time instants. The underlying assumption is that these tracers closely follow the fluid motion with minimal lag. This assumption holds true for a wide variety of flows provided that the tracers are small enough and/or that their density approaches that of the fluid. Besides their common goal, PIV and PTV do not share the same historical development and practice. An important difference is that in PIV, the concentration of tracers is rather high and the measurement of the âĂIJlocalâĂİ fluid velocity results from an average over many tracers contained in a measurement volume. This volume is usually regularly spaced and its size determines the spatial resolution. This is in contrast with PTV, where the velocity is determined at random locations using the images produced by a single tracer. In the case of PIV techniques, correlation-based algorithms are the most popular methods in use today. Some algorithms use the Fast Fourier Transform (FFT), which accelerates the processing speed (Willert and Gharib, 1991a). The FFT correlation method, while very efficient, can suffer from the out-of-pattern effect (McKenna and McGillis, 2002). This effect can be reduced by introducing an image shifting technique (Westerweel et al., 1997). One limitation of PIV correlation-based algorithms is the spatial resolution. Because flow scales smaller than the sub-image dimensions used to obtain the correlation cannot be captured, the result from an auto/cross-correlation operation represents the mean displacement of all particles within the sub-image domain. Attempting to increase spatial resolution by choosing small sub-image dimensions may lead to erroneous determination of velocity gradients, since faster moving particles leave the sub-image region and the remaining slower moving particles act to bias the displacement estimate toward slower velocities. This effect limits the overall spatial resolution and the capability of discerning, with accuracy, regions with high velocity gradients, such as those found nearby vortices centers or close to boundaries.

PTV has a higher theoretical spatial resolution and performs better in regions with

high velocity gradients than PIV. PTV theoretical spatial resolution is proportional to the discernible individual particle pairs between frames; increasing the seeding density in the flow would increase the spatial resolution. However, in highly seeded flows, discerning individual particles close to each other becomes difficult, therefore PTV algorithms perform better for low seeding densities, for which the distance a particle travels between exposures is small compared to the average distance to its nearest neighbor. Most of the error on PTV algorithms relates with the capability of particle detection and centroid location. Until now there is not a single procedure that can be used for the wide range of applications in which PTV can be applied. Moreover, PTV algorithms are more influenced by out-of-plane noise than the correlation-based PIV counterpart (Stellmacher and Obermayer, 2000). Particle appearance/disappearance on the search regions deforms the matching patterns for particle tracking, contributing thus to increase the out-of-plane noise. Although PTV novel methodologies are being continuously introduced and improved (Feng et al., 2007; Guasto et al., 2006; Ido and Murai, 2006; Ruan and Zhao, 2005), the use of well-established models for particle detection, centroid determination and matching allows for applying previously gained experience to update and/or improve the algorithms employed for such tasks, so one can take advantage of advances in hardware. Moreover, the use of already known application software implies previous testing with actual experimental data in different and frequently difficult conditions, thus allowing for better quality control. The main goal of this work is to develop a PTV method based on improved and well-established algorithms, capable of overcoming most of the common problems associated with near-wall measurements, where particularly difficult experimental conditions are normally faced by imaging-based techniques. Some problems encountered in these measurements are non-uniform illumination due to laser wall reflections, lens aberrations, low density of seeding particles, and high velocity gradients. In this

improved PTV method, the problems mentioned are faced by the use of enhanced particle detection and centroid estimation algorithms, which allowed for higher particle density concentration and a noticeable reduction on the total error associated with particle displacement between frames. It has been recently shown that PIV measurements may require correction in order to accurately determine turbulence quantities as mean turbulent kinetic energy and energy dissipation rate (Lavoie et al., 2007). Since PTV can achieve higher spatial resolution in near-wall turbulence measurements than PIV, reliable and robust algorithms must be employed to reach the full potential of the PTV technique. In this work, the PTV algorithm performance is evaluated and compared with classical PIV correlation-based algorithms by using artificial images first. Bias and total error for particle displacement are computed and compared against similar PIV results. Then, additional comparisons with LDV measurements and DNS results are presented and discussed.

2.2 Laser Induced Fluorescence

For the design and safety analysis of high energy heat transfer systems, such as nuclear reactors and industrial heat exchangers, there is a need of experimental investigations to validate and improve current models and correlations to better describe the complex flow phenomena involved. e.g., The Reynolds decomposition analysis of turbulent heat and mass transfer, give rise to closure problems on which terms such as the turbulent transport of momentum $\langle v_i v_j \rangle$ and the turbulent transport of heat $\langle v_i T' \rangle$ are unknowns, and a closure is necessary. The determination of these terms requires the instantaneous and simultaneous measurements of velocity and temperature, at the same location, with high frequency resolution. Most of the measurements of this terms have been performed by means of intrusive sensors at

high frequency but with a low spatial resolution. Multiple techniques to provide simultaneous, non-intrusive, whole-field measurements of temperature and velocity have been developed, however, these techniques have not been explored intensively. For brevity just the must significant are listed next. Laser Induced Fluorescence (LIF) is a non-intrusive technique used to measure whole-field scalar properties of fluids. Details on the principles of laser-induced fluorescence can be found in various references such as reference (Pringsheim and Schulman, 1950). Briefly, a laser source is used to excite an electronic absorption transition of a species present in the flow of interest. A fraction of the laser light is absorbed, followed by a spontaneous emission of light at a different wavelength (Karasso and Mungal, 1997), the light emitted by the dye is called fluorescence, and it is dependent on many variables such as incident laser intensity, dye concentration, absorption coefficient, quantum efficiency, pH, and temperature. Therefore, with a careful conditioning of experiments, LIF can be used as an indirect measure of fluids pH, concentration, temperature, etc. The use of LIF as a temperature measuring tool, started with the single-dye/one-color LIF technique (Coolen et al., 1999; Lavieille et al., 2000; Lemoine et al., 1999; Ross et al., 2001; Sakakibara et al., 1997; Seüntiens et al., 2001), however this technique showed to have significant errors related to the laser light intensity fluctuations. To correct for this problem, a ratiometric technique was implemented, on which the laser fluctuations induced errors are reduced. This technique was called two-color LIF. The two-color LIF technique can be implemented using two different approaches, the two-color/single-dye LIF (Bruchhausen et al., 2005; Castanet et al., 2003; Lavieille et al., 2001, 2002) and two-color/two-dye LIF (Coppeta and Rogers, 1998; Funatani et al., 2004; Hishida and Sakakibara, 2000; Kim et al., 2003; Natrajan and Christensen, 2009; Sakakibara and Adrian, 1999, 2004). Two-color/two-dye LIF technique combined with PIV, have been the preferred approach to make simultaneous 2-D whole-field

measurements of temperature and velocity, although this technique requires complex calibration procedures, this technique provides small errors (about 0.2 °C), and a wide temperature measurement range (about 70 °C). In the present study, two-color/two-dye LIF is used for whole-field 2-D temperature measurements. The main difference between this and previous studies is in the dye selection: traditionally the organic dyes selected to perform two-color/two-dye LIF measurements are Rhodamine-B and Rhodamine-110 (Sakakibara and Adrian, 2004). Rhodamine-B provides a fluorescence emission dependent on temperature while Rhodamine-110 provides an emission independent of temperature. In this work, Rhodamine-110 is replaced by Fluorescein-27, which provides a second dye dependent on temperature. By using two temperature dependent dyes, the temperature sensitivity of the technique is increased (Sutton et al., 2008).

2.3 High Speed Shadowgraphy and Optical Probe Sensors

To study the dispersed-phase on multi-phase flows, researchers have mainly relied on two techniques: visualization experiments and experiments with point measurement sensors. The preferred visualization technique among researchers is the shadowgraphy technique, which is easy to implement and can be applied at very high frequencies, however, visualization techniques are limited to very low void fractions. Therefore point measurement probes account for those conditions on which visualization techniques are impractical, i.e., point measurement probes are preferred for high void fraction conditions. Although for low void fractions and/or small bubbles sizes, the large point measurement probes produce erroneous results of bubble dynamics. Therefore in this part of the review, are presented comparative studies of shadowgraphy applications versus optical sensor experiments to gain a

better understanding of the scopes and limitations that these techniques present.

2.3.1 Shadowgraphy

In contrast with PTV, shadowgraphy is a visualization method that does not require particle seeding and a laser as its illumination source. Usually, halogen lamps or light emitting diodes (LEDs) are sufficient to serve as the light source for illumination. This method does not require costly or high-powered lasers and is a simple method to obtain bubble dynamics; it is a non-intrusive method and provides means to estimate dispersed flow velocity measurements. Bubble velocity, size, and void fraction can be obtained with this method. Lindken and Merzkirch (2002) performed an experiment in which they applied PIV and shadowgraphy. They injected bubbles at a Reynolds number of 1,400 into a square tank filled with stagnant liquid and measured the bubble and liquid velocity with a camera. Even though they were able to measure the velocity of the two phases simultaneously, the distributions of void fractions and bubble sizes were not reported. Zaruba et al. (2005) measured the velocity and size of bubbles in a rectangular bubble column 10 cm in width and 2 cm in depth. The bubbles were inserted through an aquarium porous stone with a range of superficial gas velocities of 1-6 mm/s. The only method utilized was similar to shadowgraphy. The velocity was calculated by tracking the center of mass of each bubble. To measure the size of the bubbles, a method was proposed in which only spherical and elliptical bubbles were considered. Due to its limitation, they concluded that the method would have to be improved. Their results did not include any information pertaining to the liquid's velocity.

2.3.2 Optical Probe

The optical probe takes advantage of the different physical properties between the dilute and dispersed phases. The optical fiber of the probe is manufactured from glass.

When light travels through the fiber, internal reflection allows the light to propagate through the fiber. There is a light source on the non-tip end of the optical probe. Since glass has a higher index of refraction than the gas and water, whenever the tip of the probe senses a bubble (a different medium), the light is refracted back through the fiber. There is no refraction of light when the probe-tip senses water because the probe was calibrated in the gas and not water. Therefore it will only produce a signal when in contact with a bubble. A detecting system can be assembled so that a signal is produced from the refracted light. This signal will have a rising edge when the probe-tip enters the bubble and a falling edge when the tip will exit the bubble. Based on the amount of time the tip was inside the bubble and the distance between entering and exiting the bubble, parameters such as velocity and size can be calculated. Statistics on this signal can provide void fraction distributions (Vejražka et al., 2010). Even though optical probes have spatial limitations, they have been used and studied in the past and are accurate tools to obtain bubble properties. If the experimental conditions required for an apparatus made of non-transparent material or if the void fraction may be large, imaging techniques may not be usable (Chaumat et al., 2005). An optical probe, in this case, will provide the parameters being sought.

Multiple studies are based on these techniques, but only relevant studies will be mentioned. Revankar and Ishii (1992) presented the radial profiles of the void fraction, bubble velocity, bubble chord length, and interfacial area concentration at various gas flow rates using a double sensor probe. Experiments were performed inside a 5.08 cm inner diameter pipe and the superficial gas velocity ranged from 0.0034–0.1212 m/s with no liquid flow. The void fraction, interfacial area concentration, and Sauter mean diameter were compared with photographic measurements analyzed by tracing the bubble projections on paper. Kiambi et al. (2003) compared bubble parameters measured from a double optical probe and from flow visualization. Their test section

was a tank with a 15 cm square cross-section. The gas velocity was kept at low rates so as to produce bubble sizes of 2.15 mm and 4.5mm from capillary tubes of diameters 0.33 mm and 1.00 mm, respectively. From the flow visualization, multiple virtual probes were configured and introduced into the path of the bubbles reconstructed from the images, although it is unclear exactly how the virtual probe technique was performed. No liquid measurements were acquired in their experiment. Their results showed that the optical probe underestimated the void fraction and overestimated the interfacial velocity. The same methods, namely optical probe and imaging, were implemented by Chaumat et al. (2005) in a study measuring two-phase flow inside a 25 cm square cross-section tank. The gas flow rate varied between 0.8–4.0 mL/s. Their results showed that as the bubbles became larger (proportional to the increase of flow rate) the deviation in the results between the probe and visualization grew. The liquid phase was not measured in their experiments. Other experiments have also employed a dual-tip optical probe, such as the one used in this study, to measure two-phase flow parameters (Chaumat et al., 2007; Johansen et al., 2010; Lima Neto et al., 2008; Rensen and Roig, 2001). Although intrusive methods and techniques have delivered valuable information, the lack of spatial resolution resulting from point measurements has limited the understanding of two-phase flows; therefore, many visual measurement techniques have been implemented to improve data. Due to the increase in spatial resolution, the techniques have helped obtain qualitative information. Thanks to the development of high speed camera electronics, visualization techniques have evolved into powerful tools capable of delivering whole-field quantitative information with temporal resolutions comparable to that of point measurement techniques (Khan et al., 2011). Examples of such non-intrusive techniques include PIV, PTV, LDV, and magnetic resonance velocimetry (MRV). LIF also has been applied along with PIV to measure two-phase flows Dahikar et al. (2010); Sathe et al. (2010). Since

the point measurement instruments are spatially limited, they are unable to provide whole-field (2-D) data and may not be used as frequently as PIV and other such methods. In this work, a comparison between shadowgraphy technique and optical sensors measurements is presented as a sensitiity study to test the limitations of both techniques. This will help to select optimal experimental conditions to accurately measure liquid and bubbles dynamics in subcooled flow boiling.

2.4 Subcooled Flow Boiling

To overcome some of the limitations inherent of point measurement techniques, full-field visualization techniques have been used on multiple two-phase flow studies (Dominguez-Ontiveros et al., 2006; Hassan et al., 2005; Koyasu et al., 2009; Ortiz-Villafuerte and Hassan, 2006). However, there appears to be a scarcity of subcooled boiling experimental studies that can capture instantaneous whole-field measurements. As an answer to the need of high quality and reliable experimental information of subcooled boiling flow, Estrada-Perez and Hassan (2010) performed whole-field particle tracking velocimetry experiments in a rectangular vertical channel with a single heated wall. They focus on the liquid turbulence modification due to wall heating. Their results confirmed the behavior found in previous studies and provided new information due to the full-field nature of the technique. The new provided information has already been used towards the development of near-wall liquid velocity modeling and for CFD simulations validation (Končar and Matkovič, 2012).

Although a large number of studies are available in the literature, subcooled flow boiling is still not completely understood. Due to experimental and technical difficulties, most of these studies are often oriented to measure parameters of only one phase, i.e. either liquid or vapor parameters, with experimental approaches

that are also limited to either long-term averages, such as average void fraction distribution, average velocity profiles, etc. or instantaneous or fast occurring events, such as bubbles departure frequency, bubble growth rate, etc. Furthermore, there had been limited attempts to capture simultaneously the full-field wall heat transfer mechanisms and the interaction with the liquid and vapor dynamics.

The present study is a continuation of the experimental endeavor started by Estrada-Perez and Hassan (2010), and has the objective of extending the measurements reliability when conducting simultaneous particle tracking velocimetry (PTV), high speed shadowgraphy (HSS) and infrared thermometry (IR-T) for the study of subcooled flow boiling phenomena. Although these techniques have been previously validated at multiple experimental conditions (Kähler et al., 2012; Khan, 2012; Kim et al., 2012), there has not been any attempt to perform all these techniques simultaneously to study subcooled flow boiling. Therefore, issues related to the scope and limitations of these techniques have to be addressed before attempting meaningful subcooled boiling measurements. To this end, a series of sensitivity studies and uncertainty analysis were performed, from which recommendations for the proper implementation of visualization techniques for the study of two-phase flows are given. This work also provides subcooled boiling flow experimental measurements which are based on these recommendations.

There are multiple studies on subcooled boiling flow, but for sake of brevity, only those relevant to this study are classified in the following groups: 1) studies that focus on measuring average liquid turbulence quantities and 2) studies that focus on the measurement of bubbles dynamics parameters. Most of the studies that focus on measuring average turbulence quantities rely on point measurement probes and generally focus on the study of the liquid turbulence and local void properties.

2.4.1 Average Liquid Turbulence Parameters

There has been multiple experimental efforts to study subcooled flow boiling. However, a handful of works had attempted to measure the liquid turbulence modification due to boiling flow parameters (Lee et al., 2002; Roy et al., 1997; Yun et al., 2010, 2008). These experiments exhibit a common measuring approach of utilizing point measurement probes. Roy et al. (1997) utilized a two-component Laser Doppler Velocimetry (LDV) system to measure both, the liquid and boiling bubbles velocities. They also used a dual-sensor fiber optical probe (FOP) and a Constant Temperature hot film Anemometer (CTA) to measure vapor bubble-related quantities and vapor/liquid temperatures. Lee et al. (2002) provided measurements of local void fraction and velocity profiles of both phases. Their measurements were based on a two-conductivity probe for the local void fraction and vapor velocity, and a Pitot tube method for the local liquid velocity. Situ et al. (2004) measured the flow structure of subcooled boiling flow in an annulus. They used a double-sensor conductivity probe method to measure local void fraction, interfacial area concentration and interfacial velocities. Yun et al. (2008) performed subcooled boiling experiments in a 3×3 rod bundle. They use a double sensor conductivity probe for the vapor phase measurements and a Pitot tube for the local liquid velocity. Rather than presenting their results as local profiles, they presented interpolated 2D maps of liquid velocity, void fraction, interfacial area concentration, interfacial velocity, and bubble Sauter mean diameter for several conditions. Yun et al. (2010) performed subcooled boiling experiments through a concentric annulus, they used a double sensor optical fiber probe for the local measurement of void fraction, bubbles velocities, Sauter mean diameter and the interfacial area concentration, and in separate experiments using a specially designed Pitot probe and a K-Type thermocouple, they measured the local

liquid velocity and temperature.

2.4.2 Bubble Dynamics in Subcooled Flow Boiling

When studying the bubble dynamics in subcooled boiling flow, most of the studies rely on visualization techniques. A summary of such works is presented next. Abdelmessih et al. (1972) used high speed photography to investigate the effect of fluid velocity on the growth and collapse of vapor bubbles in slightly subcooled distilled water in an open loop. The measurements included the description of typical parameters describing the lifetime of a bubble: bubble nucleation frequency, growth, and collapse. Similarly Ünal (1976) with high speed film photography measured maximum bubble diameters at different subcooling levels and flow rates. Their results fitted previously proposed correlations for the bubbles diameters. Klausner et al. (1993) used high speed digital photography to measure bubble departure diameters. Also, a theoretical analysis was performed to predict that the expected bubbles departure diameter is strongly influenced by the flow velocity and the wall superheat. Bibeau and Salcudean (1994) performed bubble dynamics measurements using high speed photography. They concluded that bubbles generated near the onset of nucleate boiling conditions slide for longer distances compared to those at different conditions. The maximum bubble diameter and condensation time are shown to be influenced by the location relative to the onset of significant void. Thorncroft et al. (1998) performed a visualization study of vapor bubble growth and departure in vertical upflow and downflow forced convection boiling. They observed significant differences on the boiling bubbles behavior depending on the liquid flow direction. They observed that the vapor bubble sliding process was an important enhancing mechanism of the heat transferred from the heater wall to the liquid. Chen et al. (2011) studied the effects of channel size on subcooled boiling. They found an increase of both,

heat transfer and bubble nucleation frequency when the channel dimensions were reduced. They also observed bubbles merging on the nucleation site due to increases on heat flux. Ahmadi et al. (2012) observed that at high liquid subcooling close to the onset of nucleate boiling conditions, all nucleated bubbles departed from the heater wall and condensed. For lower subcooling levels, bubbles reattached to the wall after lift-off, consequently the bubble lifetime was increased. Chu et al. (2011) measured the bubble lift-off diameters and bubble nucleation frequency in terms of heat flux, mass flux, and degree of subcooling. From this data they suggested a correlation for the bubble nucleation frequency and bubble lift-off diameters. Euh et al. (2010) focused on measurements of bubble departure frequency as a function of pressure, heat flux, flow rate and subcooling level. They developed an automatic image processing technique to obtain the bubble departure frequency. Their measured data was compared with bubble frequency models available in existing literature and an improved version was proposed. Zhou et al. (2013) analyzed the behaviour of single bubbles in a narrow vertical rectangular channel. They showed that at high subcooled conditions nucleated bubbles stick to the wall and slide slowly. From their analysis they suggested that thermophoresis contributes largely to promote the bubble detachment from the wall and that this contribution increases at conditions with high liquid temperature gradients.

3. MEASURING TECHNIQUES

3.1 Particle Tracking Velocimetry

In this section, the components of the PTV algorithm that are new or relevant for the present study are described. A more detailed description of the PTV processing is given by Estrada-Perez (2004). The previous home-developed PTV software has been used in applications (Hassan and Blanchat, 1991; Hassan et al., 1992a,b), although continuously updated and improved throughout the years, it was able to handle only low- to medium-concentration seeded flows. An average error on particle centroid location of about 0.1 pixel for near-wall measurements led to displacement errors as high as 0.4 pixel (Dominguez-Ontiveros et al., 2006; Ortiz-Villafuerte and Hassan, 2006). In order to be able to work with highly seeded flows and reduce the magnitude of the different error sources, as in particle detection, particle centroid estimation, and particle matching improved algorithms were introduced in the latest version of the PTV algorithm. That is, most of the algorithm features were modified towards enhancing a PTV algorithm suitable for near-wall measurements.

In this work, the improved particle detection algorithm is based on a combination of applying a pixel gray-scale thresholding and an extension of the particle mask correlation method. In this new procedure, the particle centroid estimation is based on a combination of techniques that can be implemented depending on the characteristics of the particle images (shape, size, intensity, density, etc.). The techniques used are: three-point Gaussian interpolation (3PGI), 2D Gaussian regression (2DGR), as well as the center of mass technique (CMT). For particle matching, the whole range of pixel gray-scale values is considered for cross correlating particles candidate matching, more information is available to perform the correlation, which is less influenced by

the gray scale threshold parameter used in the binarization of the images. Another improvement in this work is the use of the multi-region analysis technique which has been successfully applied to the analysis of a turbulent channel flow (Ortiz-Villafuerte and Hassan, 2006). In this work, the multi-region analysis is extended to handle multiple-shapes regions, so any polygon shape can be selected. Furthermore, the parameters for particle detection and centroid estimation can differ from region to region, as well as the particle tracking parameters. This procedure reduces not only the number of computations, but also the probability of finding spurious vectors. The next sections give a detailed explanation of the PTV algorithm.

3.1.1 Particle Detection and Centroid Estimation

The particle detection algorithm is based on both, a particle mask correlation method (Takehara, 1998) and gray-scale thresholding. The particle mask is an ideal brightness pattern of a particle image. In this work the brightness pattern is generated form the following equation:

$$I(x,y) = I_o \exp\left[-\frac{1}{2r_o^2}\left(\frac{(x-x_0)^2}{a^2} + \frac{(x-x_0)(y-y_0)}{b^2} + \frac{(y-y_0)^2}{c^2}\right)\right] \tag{3.1}$$

where $I(x,y)$ is the gray scale intensity in the (x,y) position, (x_0,y_0) is the object centroid location, I_0 is the maximum intensity of the object, a, b, and c are shape modifier parameters, and r_0 is the particle radius. Eq. (3.1) is particularly useful when searching non-circular particle images. In comparison, it is common to use the standard 2D Gaussian distribution (McKenna and McGillis, 2002; Takehara, 1998), that is, without the term affected by the parameter c. While the ideal particle image shape is close to a perfect Gaussian, experimental images are affected by camera lenses aberration and wall reflections that cause particle images to look closer to

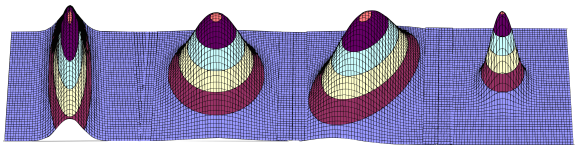

Figure 3.1: Shapes available for the particle centroid location algorithm.

elliptical shapes. The shape parameters (a, b and c) allow selecting different brightness patterns, as shown in Fig. 3.1, thus helping to detect more particle images than if only circular shapes were considered. This extended mask technique also helps diminishing the particle overlapping problem. The shape parameters depend on image quality, so they have to be set by the software user in a trial and error procedure. Although the parameters selection may appear at first quite subjective, it is not completely so. By setting values for a, b and c, (and also guess values for other parameters as search area for particle matching and choosing the centroid computation method) the user then goes through the whole process (already automatized in a batch process) until all relevant statistics of the flow are computed for an image data set and thus, making any necessary changes to one or to all three parameters. Clearly, the user must have some knowledge about the flow under research. Generally, determining a first optimum choice for the shape parameters does not take longer than one or two hours, since each "run" takes only a few minutes to provide with the statistics of the flow. Once the results are considered satisfactory fine tuning is performed and the parameters are set for a whole image data set.

After the ideal particle mask is selected, it is scanned over the entire image plane. At each pixel location, a cross correlation coefficient is calculated between the ideal particle mask and the image plane. Once a correlation coefficient plane is obtained, a pixel filtering procedure is applied to discriminate the particle pixels from those belonging to the background. Pixels with gray-scale and correlation coefficient values

larger than chosen thresholds are taken to belong to a particle. Once a particle is identified, its centroid is estimated. Three different centroid estimator techniques are tested (3PGI, 2DGR, and CMT), one at a time during the first trial, in order to find out which provides the most acceptable results. It is important to note that these techniques use the results of the modified mask correlation technique as a base (first) estimate of the particle centroid location in pixel units, since the central pixel (in particle mask) has the largest correlation coefficient computed within the particle image. The 3PGI (Willert and Gharib, 1991b) is the most commonly used among researchers due to its simplicity and high accuracy, and is expressed as:

$$\epsilon_x = \frac{\log\left[I\left(x_0 - 1,\, y_0\right)\right] - \log\left[I\left(x_0 + 1,\, y_0\right)\right]}{2\log\left[I\left(x_0 - 1,\, y_0\right)\right] - 2\log\left[I\left(x_0,\, y_0\right)\right] + \log\left[I\left(x_0 + 1,\, y_0\right)\right]} \tag{3.2}$$

Where ϵ_x is the sub-pixel correction on the x direction, (x_0, y_0) is the particle centroid position in pixel units, and I is the pixel gray-scale value. A similar procedure is done to obtain the sub-pixel correction on the y direction, ϵ_y. The particle centroid position with sub-pixel accuracy (x_c, y_c) is calculated using:

$$x_c = x_0 + \epsilon_x \tag{3.3}$$

and

$$y_c = y_0 + \epsilon_y \tag{3.4}$$

The sub-pixel corrections can also be calculated with the 2DGR (nine-point regression) technique, which works well for Gaussian-shaped particle images, circular or elliptical and in any orientation (Nobach and Honkanen, 2005). The CMT, also known as center of gravity technique, is more suitable for cases where particle images

deviate largely from a Gaussian distribution, so the other two techniques fail. However the CMT is largely affected by the particle detection procedure because it computes the particle centroid based on the gray-scale values and positions of all the pixels that represent the particle image. The location coordinates in the center of mass technique are computed from:

$$x_c = \frac{\sum_{k=1}^{k} x_k I\left(x_k,\, y_k\right)}{I\left(x_k,\, y_k\right)} \tag{3.5}$$

and

$$y_c = \frac{\sum_{k=1}^{k} y_k I\left(x_k,\, y_k\right)}{I\left(x_k,\, y_k\right)} \tag{3.6}$$

where K is the total number of pixels belonging to the object. The centroid is, for this technique, also known as the first order moment.

3.1.2 Particle Centroid Estimation Accuracy

To test and compare the performance of the improved algorithms against the original software applications for PTV, different tests were used using synthetic data. First, to determine the influence of the particle radius on the performance of the particle centroid estimator techniques, ten tests were used. In each test, an 8-bit artificial image with 500ÃŮ500 pixels was generated, having 50 particles generated with a Gaussian gray-scale distribution given by Eq. (3.1) and randomly located within the black background of the image. The small amount of simulated particles was chosen to reduce error due to particle overlapping. Each test was performed with a different particle size. There was no combination of different particle sizes in the tests. Although this is not realistic, it helps to know the limits of the software, and thus allowing for selecting appropriate sizes for tracer particles at different experimental

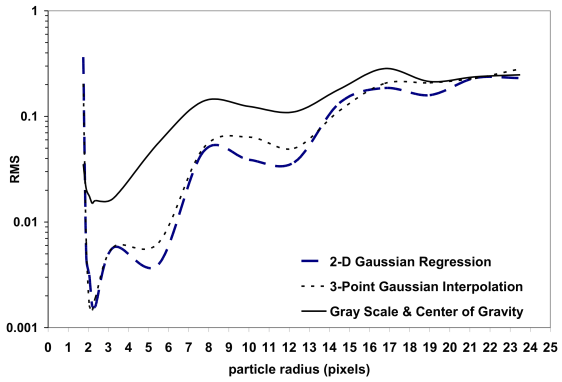

Figure 3.2: RMS bias of particle centroid estimation.

conditions.

The root mean square (RMS) error of the particle centroid estimation calculated for different particle radius for the three techniques described above is shown in Fig. 3.2. The 2DGR and the 3PGI techniques behave similarly. Initially, their RMS errors drop off with increasing particle diameter, reaching a minimum at a particle radius of 1.8 pixels, before increasing again for larger radius. The CMT showed a minimum RMS value for a particle radius of about 3 pixels, but this minimum was significantly higher, about one order of magnitude, than those presented by the 3PGI and the 2DGR. These results for the center of gravity technique agree quite well with those obtained by other authors (Udrea et al., 2000), showing errors around 0.01 pixels for simulated ideal particle images.

To test the influence of particle densities on the performance of the particle centroid estimator techniques, ten new tests were done. Artificially generated 8-bit images and varying particle densities were used, (number of particles) / (500×500 pixels), while keeping a constant particle radius of 1.8. This value was chosen because it was the optimum particle radius, according to Fig. 3.2, and also to reduce possible particle overlapping. The RMS error of the particle centroid estimation calculated

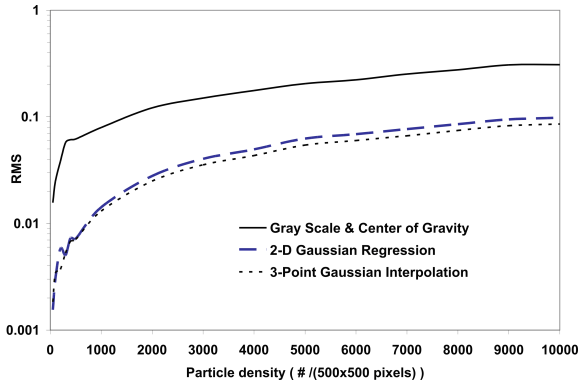

Figure 3.3: RMS bias of particle centroid estimation for different particle densities.

for different particle densities is shown in Fig. 3.3. 2DGR is more likely to fail when analyzing high particle density cases because particle overlap increases the non-Gaussian image shapes and because it uses 9 pixels for the centroid location estimation, instead of the 5 pixels used by the 3PGI. The CMT performs the worst, but for cases commonly encountered in real experimental conditions (particle radii in the range from 1.5 to 4 pixels) its RMS error remains bellow 0.1. Fig. 3.3 is clearly just an indication of the expected profile RMS error, since in actual data images, particles have a wide variety of sizes, therefore increasing the possibility of overlapping.

From the aforementioned tests, a better indication about which method to use for the analysis of actual experimental data can be drawn. 3PGI seems a natural candidate to analyze images with high density and small circular particle-shapes, while the 2DGR seems preferable to analyze images where aberration conditions are noticeable, changing the particle images from circular to elliptical shapes. Moreover, the 2DGR has a smaller peak-locking for non-circular particle images (Nobach and Honkanen, 2005). When large deviations from Gaussian particle-shapes are encountered, both the 2DGR and 3PGI fail, thus CMT is recommended. From the

previous conclusions, it was decided that in the following, the particle identification and particle centroid location determination were to be performed using the extended particle mask correlation technique in conjunction with the 2DGR. From the results shown above, a quite remarkable improvement both on the spatial resolution and error reduction could be expected for future PTV-based experimental measurements, since the CMT was used in the previous (original) PTV software application.

3.1.3 Particle Tracking Algorithm

The particle tracking algorithm used in this study, is based on direct spatial correlation, or template matching (McKenna and McGillis, 2002). This is practically a straightforward manner to compute the cross-correlation. However, this approach is also the most numerically intensive. Specifically, it computes a correlation coefficient between two sub-images that are inside a pair of single-exposed PIV images, let us say images A and B. The correlation coefficient between the sub-images I_A and I_B is computed using:

$$C_{I_A I_B}(x_0,\, y_0) = \frac{\sum_{i=1}^{a}\sum_{j=1}^{b}\left(I_A(i,\, j) - \overline{I_A}\right)\left(I_B(i,\, j) - \overline{I_B}\right)}{\left[\sum_{i=1}^{a}\sum_{j=1}^{b}\left(I_A(i,\, j) - \overline{I_A}\right)^2\right]^{1/2}\left[\sum_{i=1}^{a}\sum_{j=1}^{b}\left(I_B(i,\, j) - \overline{I_B}\right)^2\right]^{1/2}} \tag{3.7}$$

where(x_0, y_0) is the central pixel of a particle on frame A, I_A is a sub-image with size $a \times b$, centered at (x_0, y_0) on frame A, I_B is also a sub-image of size $a \times b$, but centered at the central pixel of a candidate particle on frame B. The sub-images I_A and I_B are called correlation windows. In this study, only squared correlation windows are considered, i.e. $a = b$. The candidate particles are all the particles inside a region on frame B, called the candidate window. The candidate particle with the highest correlation coefficient value represents the pair of the particle selected on

frame A.

Size and shape of the candidate window are defined by the user and previous knowledge of the flow can be used in order to determine its size. Previous knowledge means that experimental conditions are known, as velocity vector field, and if possible the field turbulence intensity, that can be used to set maximum and minimum possible displacements in adequate directions. If there is no knowledge at all of the flow field, then an iterative process is to be used, until the user is satisfied with both image visualization and computed flow statistics

3.1.4 Particle Tracking Accuracy

A procedure similar to the one presented by Astarita and Cardone (2005) to analyze the error of PIV algorithms was performed here, so a comparison could be formed between PIV and PTV. Synthetic images were used to estimate the influence of particle concentration and displacement on the tracking algorithms performance. Gui and Wereley (2002) identified three types of errors: bias (β), random (σ) and total error (δ). By using synthetic images, the exact displacement field is known, thus the errors can be quantified as follows:

$$\beta = u - \overline{u} \tag{3.8}$$

$$\sigma = \sqrt{\frac{1}{N}\sum_{i=1}^{N}\left(u_i - \overline{u}\right)^2} \tag{3.9}$$

$$\delta = \sqrt{\frac{1}{N}\sum_{i=1}^{N}\left(u_i - u\right)^2} \tag{3.10}$$

where $\overline{u}$ is the mean measured displacement value, u is the exact imposed displacement, u_i the measured displacement, and N is the number of samples.

Sets of 100 images were generated, with a common particle radius of 1.8 pixels. Four different particle densities were considered (2500, 5200, 8200 and 10000 particles per image), in 512×512 pixel images. The first three densities are close to those reported by Astarita and Cardone (2005), they used an interrogation window size of 32ÃŮ32 pixels. In this work, considering the same interrogation window size, the number of particles per interrogation window (NI) was 9.76, 20.31, 32.03, and 39.06, respectively. A fixed value for the u and v components of the velocity in each set was selected. The total error δ from the PTV analysis, as a function of the imposed displacement for different image densities, is shown in Fig. 3.4. The results show first, that the total error increases as the imposed displacement grows and second, the total error also increases with increasing particle density. The first result is also found for PIV analysis (Astarita and Cardone, 2005), but the second result shows one core difference between PIV and PTV: it is well known that PIV performs better for high particle densities, while PTV performs better for low particle densities. The main reason for this can be explained due to particle overlapping which tends to reduce the accuracy of the particle centroid estimators.

The results shown in Fig. 3.4 were obtained considering each and every one of the randomly located vectors found in the PTV analysis (almost one vector per particle), therefore different samplings were used to calculate δ for each different case. The number of vectors found (N) per case are shown in Fig. 3.5.

The differences in sampling can lead to wrong conclusions about δ when comparing different concentration sets; therefore, a uniform mesh was created using square windows. The random vectors inside these interrogation windows are used to obtain a single average vector for the given window. The total number of average vectors per image-pair is 256 (16×16 non-overlapping windows of size 32×32 pixel). Thus, for the whole data set a common sampling of approximately 25,600 vectors was used to

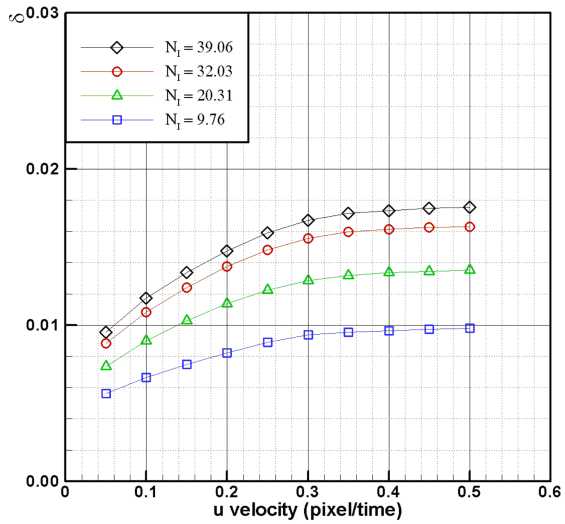

Figure 3.4: Total error as a function of the imposed displacement for different NI values.

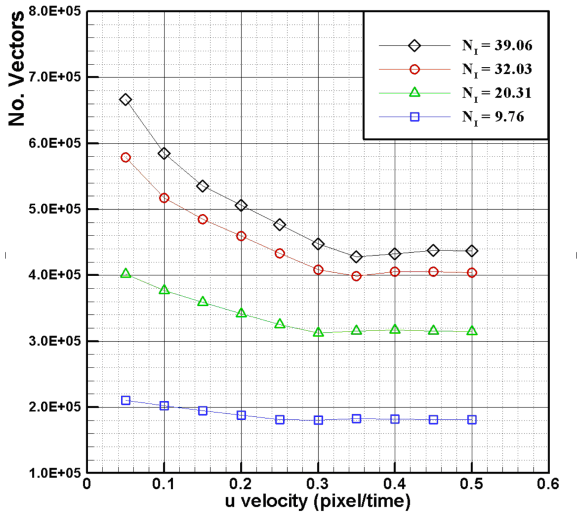

Figure 3.5: Number of vectors found in the PTV analysis as a function of imposed displacement, for different NI values.

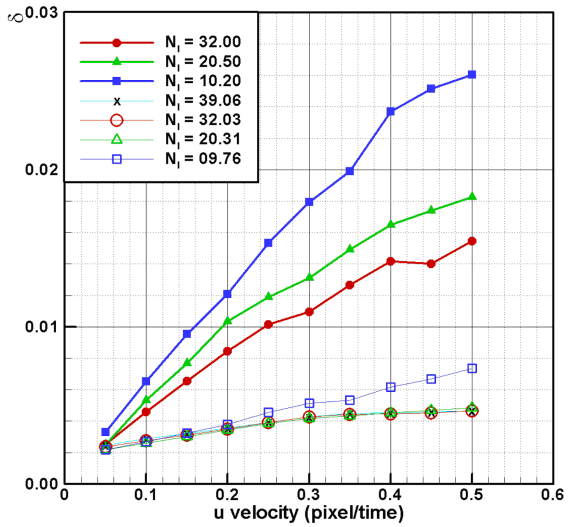

Figure 3.6: Comparison of the total error with results from Astarita and Cardone (2005) for different NI values. Closed symbols correspond to the simulations of Astarita and Cardone (2005). Open symbols correspond to this work results considering a sampling number of $N \approx$25,600.

calculate δ. The comparison with Astarita and Cardone (2005) data of classical PIV cross-correlation results and the ones obtained in this study are shown in Fig. 3.6.

In this case, PIV data is more affected by the particle density than the PTV results. PTV showed a constant total error response to variations of particle density, except for the lowest density case, where the lack of vectors within the interrogation windows produced erroneous estimations of the velocity. The accuracy in the PTV analysis even in the high particle density cases is noticeable. The improved particle detection and particle centroid estimation algorithms partly explain this finding. The capability of discerning particles close to each other highly increases the overall performance of the PTV analysis, which is reflected in a better spatial resolution without reducing the accuracy. However, the other part of the explanation is that the better performance of the improved PTV method is also related to the use of ideal particle images, that is, constant radius and brightness, in comparison with Astarita

Table 3.1: Turbulent channel flow conditions from other studies.

Authors	Johonson & Alfredson	Antonia et al	Gunther et al		Present work
Technique	Hot wire	Hot wire	LDV	DNS	PTV
w/2h	5:1	18:1	12:1	—	4:1
Reh	6900	5000	5730	5750	5128

and Cardone (2005) work.

3.1.5 Validation with Turbulent Boundary Layer Experiments

Since the synthetic image analysis indicated that the algorithm performed in a satisfactory way, the next step was to test the algorithm with experimentally obtained data. Measurements were carried in a fully developed closed channel flow, with a Reynolds number, based on half the height of the channel (Re_h), of 5128. Comparisons with LDV, hot wire measurements, as well as results from DNS at similar Reynolds numbers are presented later. Table 1 summarizes flow conditions for the present study and for measurements with hot wires at $Re_h = 6900$ (Alfredsson et al., 1988) and $Re_h = 5000$ (Antonia et al., 1992), measurements with LDV at $Re_h = 5750$ (Günther et al., 1998), and DNS computations at $Re_h = 5750$ (Günther et al., 1998).

Assuming the flow was homogeneous in the stream-wise direction, turbulence statistics were calculated. The data was divided in the vertical axis by 100 bins of 55 μm, with an average number of vectors per bin of 1100. The friction velocity, $u^* = (\tau_0/\rho)^{1/2}$, was estimated using two different methods. First, by plotting the dimensional total stress profile and taking a best fit of the near-wall total stress to determine τ_0. In this manner, u^* was estimated to be 1.29 cm/s. The other method used is proposed by Durst et al. (1996). This method consists of expanding the fluctuating components of the velocity vectors in a Taylor series and approximating the Reynolds stress in the near wall region. The estimation for u^* using this method

was 1.26 cm/s, thus confirming the efficiency of the procedure. The friction velocity calculated with the Durst method was used to obtain dimensionless variables.

Fig. 3.7 shows the non-dimensional stream-wise velocity, u^+, versus the non-dimensional y-location, y^+. The abscissa is in log coordinates to expand the inner region of the velocity profile. Two plots of the law of the wall are presented in each figure to avoid data point overcrowding. Good agreement is shown by the PTV measurements (current results) with DNS and LDV. Particularly important is the good agreement with the law of the wall for all measurement points, from $y^+ \approx 1$ to $y^+ \approx 60$. Although Fig. 3.7 is a good example of the accuracy reached with the PTV algorithm.

The present PTV analysis procedure showed the capability to achieve good spatial resolution for near-wall measurements. The use of the particle mask correlation method allowed an improved tracer particle identification accounting for optical aberration due to lenses effects and strong reflections from the wall. The particle centroid location algorithm also helps on the distinction of overlapped particle images. Thus, more tracer spots are obtained for particle tracking. The determination of centroid coordinates location by means of the two-dimensional Gaussian regression showed to be the best performing technique. Also, the particle tracking algorithm based on template matching, shows that the total error increases with increasing particle density. Also, when vector averaging is performed to obtain a velocity field on a regular grid, this operation amplifies strongly the influence of erroneous information, leading to errors increase as high as 5 times with respect to the error from using all randomly positioned vectors. For ideal synthetic data, a displacement of up to 5 pixels keeps the error below 0.02 pixels. The tracking algorithms were tested with real experimental data from a turbulent boundary layer channel flow. The present PTV method achieved spatial accuracy comparable to that of hot wire and

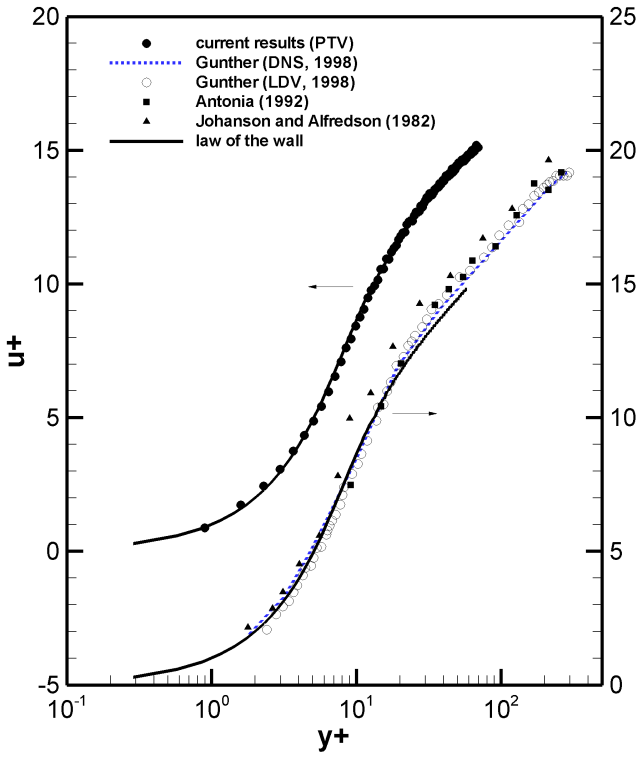

Figure 3.7: Measured mean streamwise velocity component and comparison with measurements from other techniques.

LDV measurements for mean flows and turbulence variables, even in regions close to the wall. The results also showed good agreement with DNS results. The present PTV method has shown to be suitable for near-wall experimental for two-phase flow conditions.

3.2 High Speed Shadowgraphy

Most of two-phase flow turbulence parameters have been measured using single point probes such as hot wire anemometry, laser Doppler anemometry and optical probes. These single point probes can achieve the high temporal resolution to resolve for the smallest time scales found in many engineering systems, however, their lack of spatial resolution has limited the understanding of the phenomena involved in two-phase flows. Therefore, many new measurement techniques have been explored to improve the quality of the acquired data. Flow visualization techniques have helped obtain, initially and with limitations, qualitative information of turbulence with high spatial resolution. In recent years, thanks to the development of high speed camera electronics, visualization techniques have evolved into powerful tools capable of delivering whole-field quantitative information with temporal resolutions comparable to that of single point probes. Examples of such techniques include particle image velocimetry, particle tracking velocimetry, and laser induced fluorescence. However, when dealing with two-phase flows with high void fractions, visualization techniques seems to be limited. These limitations are explored with sensitivity studies that will be presented in following sections.

The experimental sensitivity study presented in this section was performed as a validation of the in-house developed algorithm used to analyzed the shadowgraphy results. A bubble driven flow or bubble plume experiment was performed in a glass

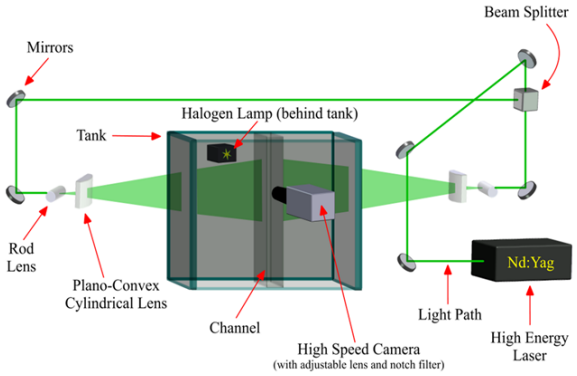

Figure 3.8: Schematic of the shadowgraphy-optical sensor sensitivity study.

tank using air at different superficial velocities. The bubbles velocity, size, and other statistics have been measured by means of shadowgraphy and a dual probe optical sensor.

3.3 Experimental Validation of Shadowgraphy by means of Optical Sensor Probe

The configuration of the experiment is shown in Fig. 3.8. The glass tank had inner dimensions of 91.44 cm in length, 30.48 cm in width, and 63.50 cm in height. The tank walls had a thickness of 1.27 cm. Two holes with a diameter of 2.54 cm were made on the bottom plate; one hole was made in the middle of the tank to drain the liquid inside, and the other hole was made close to one of the walls to allow air to pass through the bottom plate and enter the tank.

The tank was filled with 48.26 cm of water, supplied from a line at room temperature (from 20 to 22 °CC). All measurements were taken with stagnant water conditions. Air was introduced at room temperature to the tank through randomly positioned pores, which ranged from 40 to 60μm, located throughout the porous tube disk. The air inlet pressure was kept constant at 35 psig by a pressure regulator. A control valve regulated the amount of gas injected before the flow meter which

accounted for a range from 0-100 mL/min. Three superficial gas velocities (jg) were applied to produce the bubbly flow to study a range of different bubble sizes and velocities: 4.6 mm/s, 2.5 mm/s, and 1.4 mm/s. The superficial gas velocity was defined as:

$$J_g = \frac{Q_g}{A}$$

where $Q_g$is the gas volumetric flow rate and A is the flow area before entering the porous media. The square acrylic channel was placed over the porous tube in the tank. The channel had a wall thickness of 0.16 cm, each side a width of 2.2 cm, and a height of 61.0 cm. Two small slots were milled on one of the sides of the channel as to allow the placement of the optical probe. The camera used in the experiment provided a resolution of 1024 pixels x 1024 pixels and a frame rate of 1000 frames per second (fps) when observing both phases. The camera was synchronized with an Nd:YAG PIV laser to additionally obtain PIV images for the liquid phase measurements. To this end, 30μm fluorescent tracer particles were used. The laser system consisted of a diode pumped Nd:YAG laser head system operating at 80 mJ/pulse. The camera was installed on translational stages that were controlled via a computer, making it convenient to switch between measurment locations on which PTV, shadowgraphy, and the optical probe measurements were available. The experiment focused on two different regions located approximately at 36.8 cm and 40.6 cm from the inlet, Namely Region 1 and 2 respectively. In both regions, PTV and shadowgraphy studies were performed to study the liquid and bubble dynamics. Although the PTV experiments were performed separately, the optical probe and shadowgraphy measurements were performed simultaneously. This allowed the direct comparison of the bubble dynamics measured from both techniques To prevent the optical sensor to disturb the flow behavior within the shadowgraphy measuring volume, The region of interest was

placed slightly bellow the optical probe, so that the bubble-probe interactions would occur above the shadowgraphy region and cause no erroneous measurements in the shadowgraphy analysis. The area covered by the camera for both regions was 2.2 cm in width and 1.5 cm in height. An example of the simultaneous measurement of the optical sensor and the shadowgraphy technique is shown in Fig. 3.9, where typical air bubbles are shown on their path towards the optical sensor. It is important to note the that probe tips dimensions are too big to allow accurate measurement of the smaller bubbles.

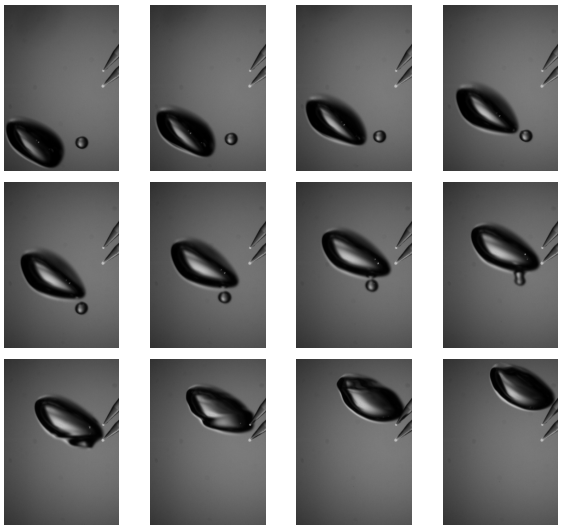

Figure 3.9: Example of simultaneous shadowgraphy and optical sensor measurements.

3.3.1 Optical Probe

The dual-tip optical probe was able to provide average gas phase parameters such as the void fraction, bubble interface velocity, and the Sauter mean diameter. The optical probe provided point measurements in 16 different horizontal positions for

each region. The measurement system, supplied by RBI Instruments, consisted of the optical probe, a signal processing optoelectronic unit, and an interface board needed to establish communication between the computer and optoelectronic unit. The probe takes advantage of the physics between two mediums, air and water. The optical fiber, manufactured from glass, relays the signal in the probe. Internal reflection allows the propagation of light when transmitting or receiving signals. The light source is located in the optoelectronic unit. When the probe tip senses a bubble (a different medium) some of the light reflects back through the fiber because glass has a higher index of refraction than air. There was no reflection of light in water since the calibration was performed in the gas (air) with a threshold level. The optoelectronic unit creates a signal produced by the reflected light from the probe-bubble interaction. Detection of a bubble occurs only if the signal is greater than or equal to the threshold level. The mentioned signal has a rising edge when the tip enters the bubble and a falling edge when it reenters the water. Based on the amount of time each tip remains inside the bubble and knowledge of other calculated parameters, the chord length and Sauter mean diameter can be obtained. The signal also assists in obtaining the void fraction Vejražka et al. (2010). An automatic measurement system assisted in performing probe measurements, and it consisted of a translational stage on which the probe was placed, allowing for horizontal movement in the channel. Once the probe was positioned in the center of the channel, the translational stage and the probe software were initiated. The probe acquired twenty minutes of data in each of the 16 horizontal locations considered to obtain horizontal profiles. These process was performed in both regions (Region 1 and Region 2) , and was repeated for each different gas flow rate.

3.3.2 PTV and Shadowgraphy

The tracking algorithm served as the primary method for measuring and obtaining 2-D parameters from the shadowgraphy and PTV images. The in-house developed algorithm, originally developed by Hassan et al. (1992b), has been improved since it was developed and is capable of detecting and estimating the centroid of the particles. Afterwards, it performs tracking between consecutive images by matching the particles through a cross-correlation method. For further detail on the algorithm, see Estrada-Perez (2004) and Estrada-Perez and Hassan (2010). The tracking algorithm analyzed data obtained from the liquid phase through PTV. It provided average liquid phase parameters: liquid velocity, fluctuating components in the liquid velocity (calculated from the root mean square), and the Reynolds shear stresses. In order to track the liquid, fluorescent particles were inserted from the top of the channel. Laser light sheets were incident from both sides of the channel, which was helpful for studying the flow in the channel. dual illumination provided quality images in which all areas in the region were illuminated. The laser sheets made tracking of the liquid possible on both sides of the bubble as well, for when a bubble is illuminated from one side, the particles on the other side receive little or no illumination and would not be tracked. After inserting the particles, time was given for them to spread uniformly throughout the channel before air was inserted. Measurements were taken some time after bubble injection to allow the flow to develop and to reach the desired flow rate. Next, the camera was signaled to record the flow. The signal supplied to the camera was synchronized to the initial pulse from the laser. Although the laser operated at 30 Hz, the time in between the two laser pulses (one from each lamp) was set to 0.001 seconds corresponding to 1000 fps. Two consecutive signals sent to the camera had an interval of five pulses in between each signal. Since the camera

was capable of recoding the images when triggered with the incoming signal, this ensured that there would be a new set of bubbles in consecutive image pairs; i.e. two images would be captured at 1000 fps, a five-pulse interval wait would occur, and the next two images would be captured at 1000 fps. This process continued until all images had been captured. The tracking algorithm also analyzed data obtained from observing the bubbles. It provided average gas phase parameters: bubble centroid velocity, fluctuating components in the velocity, void fraction, bubble size, and the Reynolds shear stresses. As the name suggests, shadowgraphy is implemented by imaging the casted bubble shadow. It is accomplished by illuminating the flow with a light source such as halogen lamps, as employed in this study, or LEDs. The illumination was strong, so a diffuser plate was required to lower the intensity of light to have a higher quality image. When light is incident on the bubble from behind, a shadow will be caused on the bubble due to refraction and reflection since water has a higher refractive index than air. In the images, the majority of each bubble results in a dark surface with a bright background. Using common image processing techniques, the image background can be removed leaving only the bubbles; thus allowing for the individual tracking of the bubbles. For shadowgraphy the camera was not synchronized to the illumination source. One signal was sufficient to trigger the camera and capture two consecutive images at 1000 fps. The camera was triggered every 0.2 seconds to ensure new bubble samples as in the case of PTV. The camera resolution was estimated to be 24 μmfrom a camera calibration procedure involving a calibration grid. It should be mentioned that the frame rate was not chosen randomly. Although 500 fps would not drastically affect the shadowgraphy analysis, results from previous test experiments showed large PTV particle displacements which is not desired because it may induce erroneous vectors detection due to the large tracking area. In contrast if the measurements are taken with a larger frame rate i.e. 2000

fps, the small particle displacement would not provide accurate statistics. Therefore, 1000 fps was chosen for all PTV and shadowgraphy measurements for this sensitivity study.

3.3.3 Uncertainty Quantification

Quantifying the uncertainty, or error, in measurements is an essential part of the results. It was desired to have an estimation of uncertainty in the results. The error was obtained in a similar manner for the methods implementing the tracking algorithm (PTV and shadowgraphy) and the optical probe. The previously mentioned uncertainties were calculated by taking the standard deviation from each set of 10 measurements for each parameter (void fraction, interface velocity, and Sauter mean diameter). The standard deviation provided the fluctuation from the average value. Since 20 minutes of measurements were taken for each data point in the channel, it was assumed that the standard deviation was a reliable approximation for the uncertainty in the measurements. The shadowgraphy data consisted of five sets and the standard deviation of each value for each parameter was calculated from the sets. Since each set of data contained 10,918 images (total 54,590 for each flow rate) it was assumed that five data sets were sufficient to approximate the uncertainty in each parameter for shadowgraphy. On the other hand, only one data set was taken for PTV measurements. The tracking performed from one PTV image-pair resulted in approximately 15,000 velocity vectors. Therefore, one data set was sectioned into five sub-data sets and a similar error analysis performed in shadowgraphy was applied to PTV.

3.3.4 Experimental Results

Although two regions were studied in this experiment we will focus on the results on the second region, for the first region was studied mainly to provide insights as to

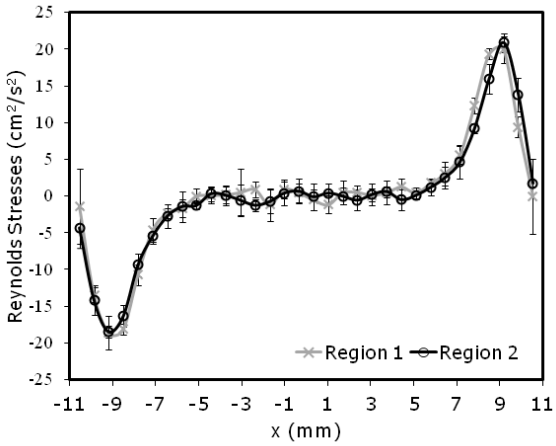

Figure 3.10: Bubble Reynolds shear stresses obtained from both regions.

whether or not the bubbly flow was fully developed. The second region was the main focus of this study.

Fig. 3.10 and Fig. 3.11 show the Reynolds shear stresses for the gas and liquid phases in both regions for the largest flow rate. The results from both regions are similar, indicating fully developed flow. Other flow rates had similar profiles for both regions.

3.3.4.1 Optimizing Time Interval Between Image Pairs

Prior to beginning the current experiment, time was invested on a similar experiment performed previously with the same apparatus. The purpose of the study was to find the optimal time between images that would result in less fluctuating profiles obtained from the tracking algorithm. The gas was inserted through the porous media into the channel. Even though shadowgraphy and the optical probe were implemented, the analysis focused on the shadowgraphy method. When the experiment was initiated the conventional procedure of obtaining the images was implemented to obtain results. The images were recorded continuously at 1000 fps

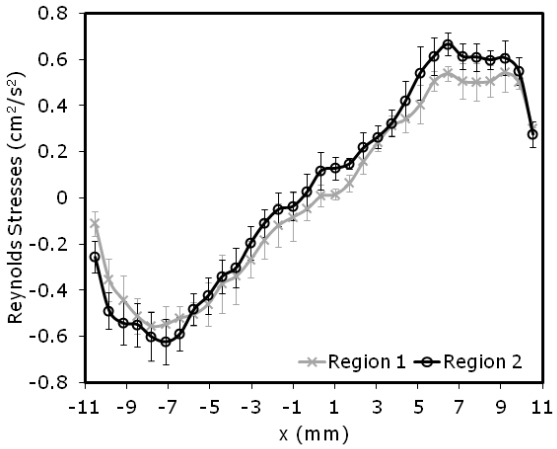

Figure 3.11: Liquid Reynolds shear stresses obtained from both regions.

resulting in 10,918 images (maximum internal camera memory). Figure 4 shows the bubble centroid velocity as a function of the distance from the center of the channel (x = 0mm). There are many fluctuations in the velocity profile and a clearly defined shape does not exist. In order to reduce the fluctuations, more frequent measurements were required. Usually, an increase in the sample number improves the statistics of the study. A bubble entering the region was tracked approximately 115 times before exiting; thus an effort was made to change the sample number of the bubbles – the bubbles that appeared in the image pairs. It was desired to track each bubble only once, rather than multiple times.

The images were then captured in sets. The camera memory was partitioned into 64 sets, each able to record 170 continuous images at 1000 fps. The camera was triggered every 15 seconds with a signal to record each set. This method ensured that a new sample of bubbles was observed after each set. As Fig. 3.12 shows, the results did not improve. Large fluctuations were still present in the profile.

Finally, it was decided to have a new sample of bubbles after each pair of images

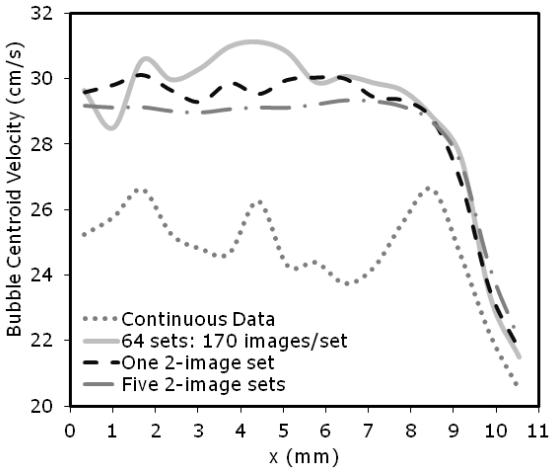

Figure 3.12: Sensitivity study showing different bubble centroid velocity profiles by varying duration in between image sets.

(it is required to have at least two consecutive images for tracking purposes). The camera was triggered to capture only two images every 0.2 seconds because it took approximately 0.115 seconds (115 images at 1000 fps) to allow a completely new set of bubbles to enter the visualization region. Again, a total of 10,918 images were captured (5,459 image pairs). Figure 4 shows how this method significantly improved the velocity profile. A more defined shape is seen, although some fluctuations are still present. As noticed, the continuous data profile is below the other profiles, indicating that using consecutive images may lead to an incorrect calculation.

Even though the profiles had improved, one set of 5,459 pairs was not sufficient. Five sets were captured in order to determine the uncertainty in the measurements. The tracking program analyzed five times the amount of data than before and performed the analysis on 54,590 images (27,295 image pairs). The fluctuations present in one two-image dataset have diminished and are no longer present.

The sensitivity study vastly assisted in improving the velocity profile.. To obtain optimal results when using captured images, this study has shown it is recommended

to have a different sample or inventory of bubbles present after each image pair. After performing this study, all the following measurements employing PTV and shadowgraphy had a sufficient time interval between image pairs to guarantee observation of a new set of bubbles.

3.3.4.2 Discrepancy Between Probe and Shadowgraphy

An important aspect was the discrepancy between the parameters provided by the optical probe and shadowgraphy. The optical probe measured higher velocity values and lower void fraction values than shadowgraphy. The two methods provide similar parameters through different techniques.

The optical probe calculates the bubble velocity based on the detection of the bubble surface, since it is the point of contact for the probe tip. The interface velocity is calculated by dividing the distance between the probe tips by the time it takes for the bubble surface to travel from one tip to the next, whereas shadowgraphy calculates the velocity by tracking the centroid of the bubble. Furthermore, the probe is a point measurement technique while shadowgraphy is a 2-D method. The probe velocity calculation presents an issue since the bubble surface is constantly deforming, especially when the bubble interacts with the probe. The probe may also not contact the bubble directly in the center. On average the bubble centroid has a smaller displacement than does the bubble surface. Since the surface is moving faster than the centroid, the velocity resulting from the probe will be greater than the one resulting from shadowgraphy.

Shadowgraphy presents an issue calculating the velocity and void fraction due to a dimensional disagreement. The problem encountered in shadowgraphy is the representation of a 3-D region as a 2-D plane. The method captures all the bubbles in the region of interest (which is a volume) but shows a planar view of that region.

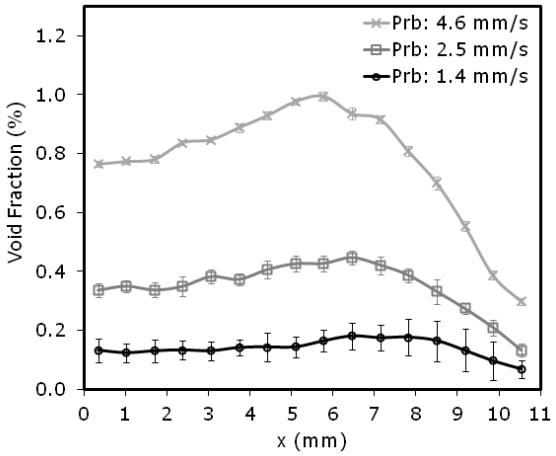

Figure 3.13: Void fraction obtained from optical probe.

Even though the velocity in the central plane of the channel is desired, the calculated velocity is an average of multiple planes throughout the channel where the bubbles exist. Due to this issue, the void fraction will be much greater when calculated by shadowgraphy as all the bubbles in the 3-D volume are collapsed into a 2-D image. For example, if there were only five bubbles in the plane of interest shadowgraphy images may show greater than ten bubbles. It is believed that the aforementioned phenomena caused the discrepancy between the two methods.

3.3.4.3 Optical Probe and Shadowgraphy Results

The optical probe and shadowgraphy provided gas phase parameters. Fig. 3.13 shows the average void fraction distribution across the channel for the different flow rates. There is an increase in the void fraction closer to the wall than the center due to the lift force that occurs close to the wall Mudde et al. (2008). Low values of the void fraction were observed due to the point measurements along a line from the optical probe. The void fraction profiles provided by shadowgraphy are shown in Fig. 3.14. The distributions have higher magnitude than the ones obtained from

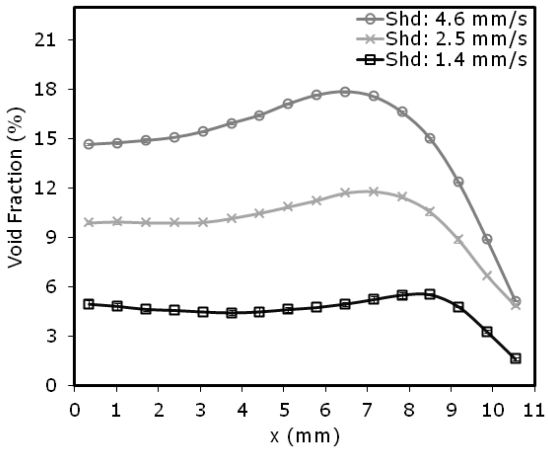

Figure 3.14: Void fraction obtained from shadowgraphy.

the optical probe. The discrepancy regarding the dimensional disagreement causes the large difference in the void fraction. The profiles exhibit a similar shape found in the optical probe results confirming that the majority of the bubbles are distributed closer to the wall. It can be seen from the figures that as the flow rate is decreased the void fraction also decreases, since the size and amount of bubbles become smaller in the channel.

The bubble interface velocity obtained from the optical probe is shown in Fig. 3.15. The decrease in the value can be observed as the distribution approaches the wall. The bubbles take a longer time to travel from one probe tip to the other when they are closer to the wall, which leads to a decrease in the velocity near the wall (v=d/t; d is constant at 1.4 mm) . A decrease in motion will occur from the bubble-wall interaction, and it was visually confirmed when bubbles collided with the wall. According to the void fraction plots, bubble to bubble interactions will also occur because of the void fraction peaking near the wall, and this may be another reason why the interfacial velocity decreases. Fig. 3.16 shows the average bubble

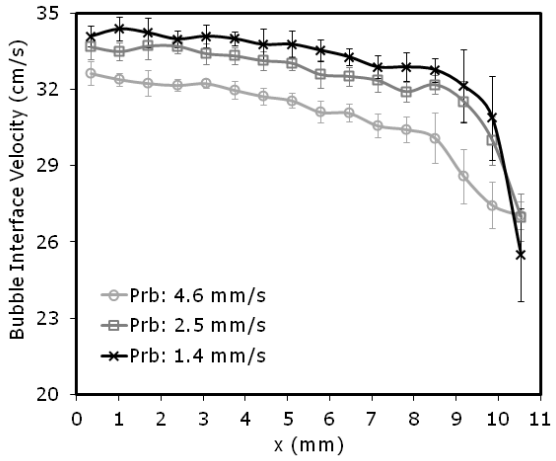

Figure 3.15: Bubble interfacial velocity obtained from the optical probe.

centroid velocity distribution for the three flow rates. Note that the velocity profiles are increasing as the flow rate decreases, similar to the bubble interface velocity from probe. The same explanation given for the optical probe can be applied here. There is a dip in the center of the distribution in Fig. 3.17 for jg = 1.4 mm/s which can be attributed to the low amount of bubbles that were present in the center of the channel. In the small flow rate case many small bubbles ranging from approximately 360 – 480 μm emerged from the porous media and predominantly remained in the center. Even if there are larger bubbles traveling faster in the center of the channel, the tiny bubbles coalesce with themselves or with larger bubbles and the cluster is tracked as one bubble. The slow velocity of the tiny bubbles reduced the average centroid velocity and leads to a dip near the center. Comparing the heights of the profiles from Figs. 3.15 and 3.17, we see that the bubble interfacial velocity is greater than the bubble centroid velocity due to the discrepancy mentioned earlier.

The velocity profiles shown in Figs. 3.15 and 3.17 increase with decreasing flow rate. The opposite may be expected as larger bubbles are thought to travel faster due

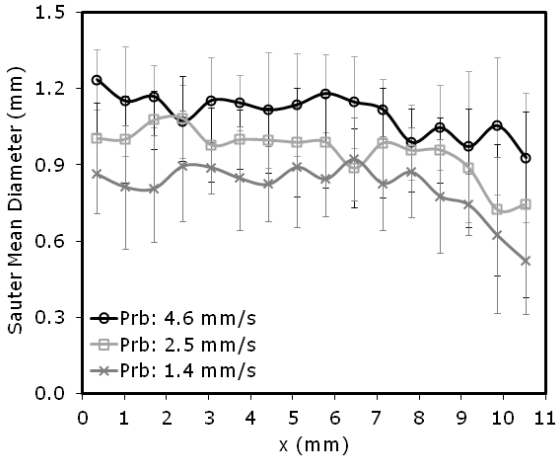

Figure 3.16: Sauter mean diameter obtained from the optical probe.

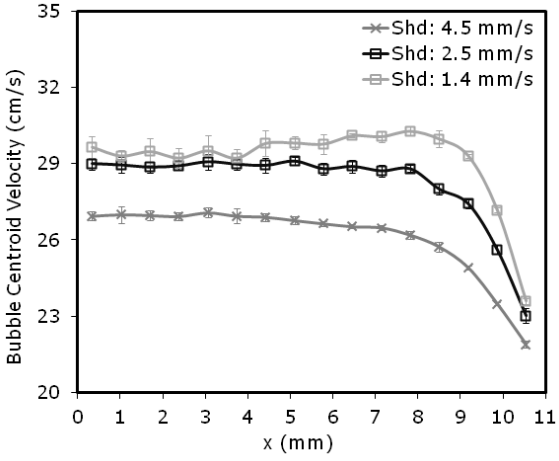

Figure 3.17: Bubble centroid velocity obtained from shadowgraphy.

to their size; however, the results show that larger bubbles have the lowest average velocity. This phenomenon may be caused by surface deformations of the larger bubbles. Another explanation may come from the forces acting on the bubble. Larger bubbles are more buoyant compared to smaller bubbles, but have less surface tension per volume; , therefore they oscillate more frequently than smaller bubbles, constantly deforming their surface. Small bubbles do not have surface deformations on the same scale as do large bubbles and, although they are less buoyant, less frequent oscillations may allow them to travel faster. Both types of oscillations for the two kinds of bubble sizes were visually confirmed. The trend of increasing velocity with decreasing flow rate may be due to a certain bubble size range present from the flow rates chosen for this experiment. From this study the results showed a greater velocity for smaller bubbles than for larger bubbles. This does not infer that if the flow rate is reduced further, bubbles smaller than the current size will travel faster. Similarly it does not infer that bubbles larger than their current size will travel slower if the flow rate is increased further. The Sauter mean diameter (Fig. 3.16) was not found to have any particular pattern as the flow rate decreased other than the decrease in the average size and increase in the average uncertainty. It was expected that the bubbles will become smaller as the flow rate was reduced, which is shown in the figures X AND Y. The increase in the uncertainty implies larger variation in the bubble size as the flow rate decreases. Bubble size was also estimated from shadowgraphy (Fig. 3.18). The size was based on the assumption that the bubbles were spherical (circular in 2-D view). The figure shows the decreases proportionally with the flow rate. A similar trend was found in the Sauter mean diameter measured by the optical probe, confirming that the bubbles become smaller as the flow rate is reduced. For each flow rate, the size remains fairly constant after which the profiles drop quickly. This indicates that the larger bubbles in a given flow rate tend to remain in the central

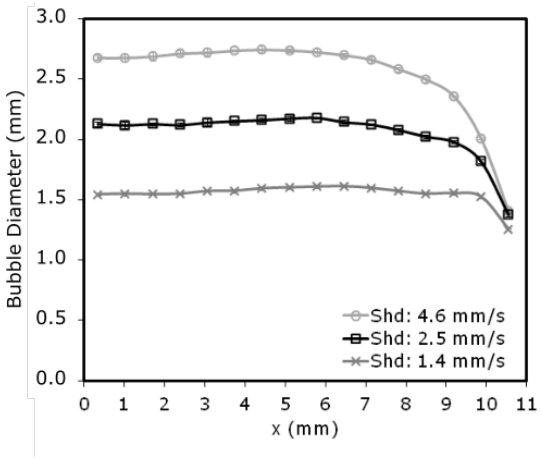

Figure 3.18: Bubble diameter obtained from shadowgraphy.

region of the channel, whereas the smaller bubbles remain close to the wall.

3.3.4.4 Turbulence Related Results from Visual Methods

The tracking algorithm applied to the visual methods (shadowgraphy and PTV) was able to provide turbulence related parameters such as the fluctuating velocity for each component (u', v') and the Reynolds shear stresses through the full channel region. The fluctuating velocity represents the degree of variation in the instantaneous velocity from the average velocity; for example, large values would occur from large fluctuations in the flow due to the constant change in the instantaneous velocity. Studying and measuring turbulence parameters is vital in understanding two-phase flow behavior. Experimental parameters are necessary for turbulence modeling and, in general, for improving and validating simulations. Although there was no liquid flow in the channel, the liquid movement was caused by the bubbles, which is negligible compared to the bubble motion as shown in Fig. 3.19. Since all average liquid velocities are less than 2.0 % of the average bubble velocities, the remaining liquid velocities are not shown. The bubbles' fluctuating velocity in the axial and radial

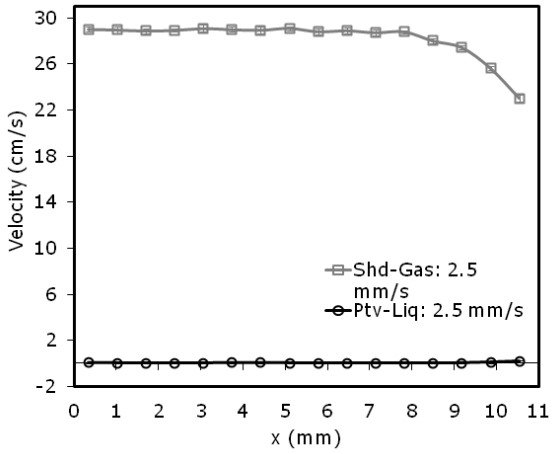

Figure 3.19: Liquid velocity shown to be negligible compared to gas velocity.

directions can be appreciated in Fig. 3.20 A and B. The high and medium flow rates seem to have a consistent profile in the center of the channel whereas the low flow rate shows irregularities in the profile, especially for the values of v'. The values of u and v change as the flow rate is decreased: u decreases and v increases; thus the fluctuations of the radial component of the velocity decrease and those of the axial component increase. These relationships suggest larger bubbles oscillate more frequently than smaller bubbles. The fluctuations in the axial and the radial components of liquid velocity were provided by the rms values, shown in Fig. 3.21 A and B. Notice the decrease in the values of the fluctuations as the flow rate decreases. Due to the large liquid disturbance caused by the large bubbles, the fluctuation value is highest for jg = 4.6 mm/s; on the other hand, smaller bubbles will cause smaller liquid disturbance, so the low flow rate has the lowest fluctuation values. The axial component of the fluctuating velocity has larger values than the radial component for all three flow rates; for this reason the variation in the liquid velocity is larger in the axial direction than the radial direction. This relationship can be confirmed intuitively since the bubble

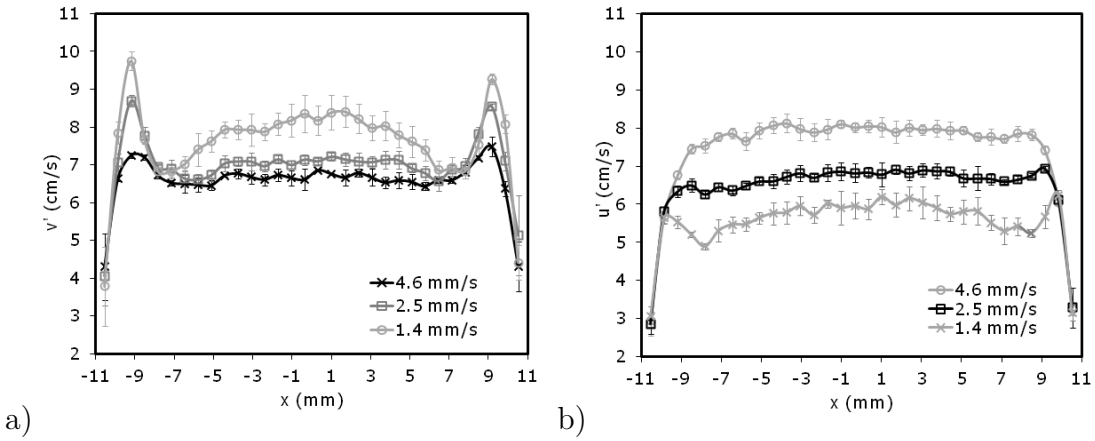

a) b)

Figure 3.20: Fluctuations in the bubble velocity: a) axial, b) radial.

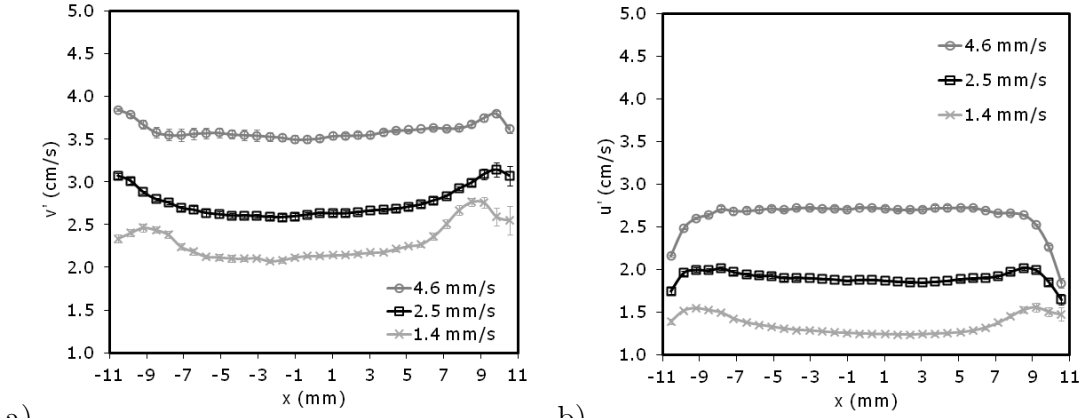

a) b)

Figure 3.21: Fluctuations in the liquid velocity: a) axial, b) radial.

motion is mainly in the axial direction, and as a result the major effect on the velocity fluctuations should be in the same direction. The Reynolds shear stresses obtained from shadowgraphy are shown in Fig. 3.22. The figure shows large changes near the walls probably due to the large velocity gradient occurring in that area (refer to the difference in the centroid velocity from x=7 to x =11 mm in Fig. 3.17). The increase in the peak values in the stresses as the flow rate decreases is worthy of mentioning. The Reynolds stresses show that as the flow rate decreases the bubble centroid velocity

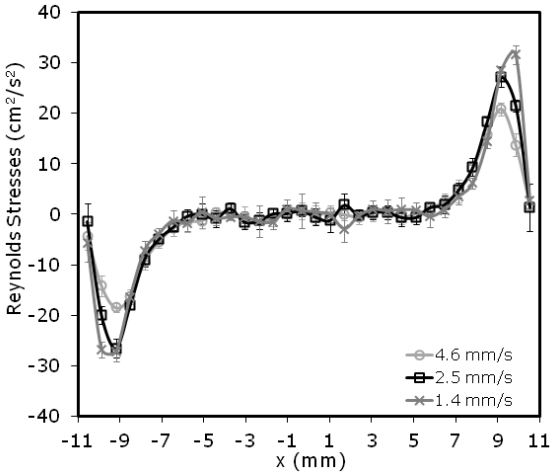

Figure 3.22: Bubble Reynolds shear stresses obtained from shadowgraphy.

increases and causes a larger velocity gradient as it approaches the wall. In Fig. 3.22 the profile at the center of the channel for jg = 1.4 mm/s remains relatively flat, and though the velocity distribution in Fig. 3.17 shows a slight increase in the center of the channel there seems to be no indication of an increment in the Reynolds shear stress. The lack of such an increase may be due to the low magnitude of the gradient near the center compared to the high gradient near the wall. The Reynolds shear stresses obtained from PTV are shown in Fig. 3.23. They show a changing profile throughout the channel. The largest values occur from the highest flow rate due to the largest liquid displacement. As the flow rate is reduced, the profile decreases indicating that there are fewer fluctuations in the liquid velocity. Two techniques, an optical probe and a tracking algorithm, were successfully applied in this experiment to obtain two-phase flow parameters in a square channel. The study was performed far from the bubble injection location. Air was inserted into the channel at three superficial gas velocities: 4.6 mm/s, 2.5 mm/s, and 1.4 mm/s. Using an in-house developed tracking algorithm, 2-D measurements were taken with shadowgraphy and

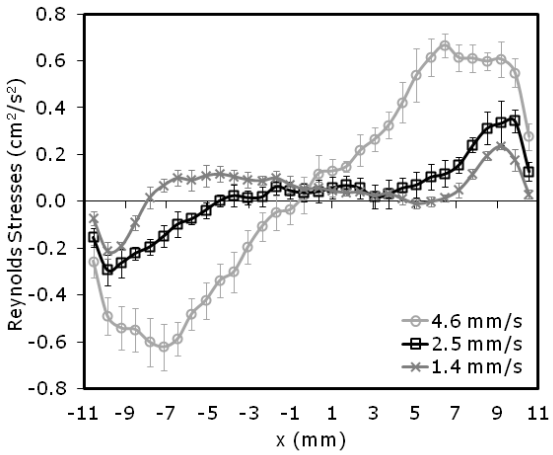

Figure 3.23: Liquid Reynolds stresses obtained from PTV.

PTV . Both methods provided turbulence related parameters such as the fluctuating velocity and the Reynolds shear stresses. Although liquid velocity was measured from PTV, it was considered to be negligible compared to bubble velocity. Since the optical probe and shadowgraphy measured the gas phase, parameters such as the void fraction, gas velocity, and bubble size were compared. From the previous study performed, it was shown that a new bubble sample after each image pair (every two images) had an enormous effect on the velocity profiles. The explanation was given as to why a difference exists between the same parameters obtained from the optical probe and shadowgraphy. Mainly, the measurement technique of each method caused the difference in the results. Due to the point measurement nature of the optical probe all calculations were based on the line of impact through the bubble, whether it was at the center or the edge of the bubble. Also, the probe-bubble interaction produced more surface deformations and affected the interface velocity. A dimensional disagreement was involved in shadowgraphy results. The 3-D volume was projected to a 2-D plane, which caused the void fraction results to be much greater than those

obtained from the optical probe. After concluding the experiment it was understood that the optical probe underestimates the gas phase parameters and shadowgraphy overestimates them due to their measurement method having only bubble velocity exception. PTV was the most precise in its measurement method since only particles present in the laser light plane were tracked, although in some parts of the images the liquid is covered by bubbles. The data obtained from this experiment will assist in improving and validating current simulation techniques.

3.4 LIF Principle

Laser Induced Fluorescence (LIF) is a non-intrusive technique used to measure whole-field scalar properties of fluids. Details on the principles of laser induced fluorescence can be found in various references (Pringsheim and Schulman, 1950). Briefly, a laser source is used to excite an electronic absorption transition of a species present in the flow of interest. A fraction of the laser light is absorbed, followed by a spontaneous emission of light at a different wavelength (Karasso and Mungal, 1997). The light emitted by the dye is called fluorescence, and it is dependent on many variables such as incident laser intensity, dye concentration, absorption coefficient, quantum efficiency, pH, and temperature. Therefore, with a careful conditioning of experiments, LIF can be used as an indirect measure of a fluid's pH, concentration, temperature, etc. Fluorescence is a radiative decay process that occurs by electronic transitions in molecules. After a fluorescent dye molecule is exposed to an electromagnetic field, photons entering the molecule cause displacements of electrons from one region of the molecule to another. The displacement of electrons results in increased potential energy of the molecule from a ground state to the first electronic excited state. When the energy state returns to the ground state,

fluorescent light emission takes place as a radiative process (Sakakibara and Adrian, 1999). The ratio of the total energy emitted per quantum of energy absorbed by the molecule is called the quantum efficiency, ϕ. The fluorescence energy I (Wm^{-3}) emitted per unit volume is defined as

$$I = I_0 C \phi \epsilon \tag{3.11}$$

where I_0 is the incident light flux (Wm^{-2}), C is the concentration of the dye solution (kgm^{-3}), and ϵ is an absorption coefficient ($\mathrm{m}^2\mathrm{kg}^{-1}$). Because, for some dyes, the quantum efficiency ϕ depends on temperature and considering that the absorption coefficient ϵ is constant and small, it is possible to measure the temperature of the solution if one can keep the incident light flux, I_0, and concentration, C, constant. To reduce the influence of I_0, a mixture of two dyes, called A and B whose quantum efficiencies differ, can be used. In addition, the two dyes should have different emission spectra so that the emitted light can be separated by optical means. If the two emission spectra can be separated, then the individual intensities can be measured by two different cameras. From the cameras output, the following ratio can be obtained

$$\frac{I_A}{I_B} = \frac{C_A \phi_A \epsilon_A}{C_B \phi_B \epsilon_B} \tag{3.12}$$

This ratio is independent of the incident light flux I_0, but it can depend on temperature through the ratio ϕ_A/ϕ_B.

Multiple fluorescent dyes may be selected as candidates; however, few of them have suitable characteristics. RhB is one widely used dye for LIF thermometry due to its temperature sensitivity (2.3% K^{-1}) and spectrum characteristics (Coppeta and Rogers, 1998). However, when using RhB with the two-color/single-dye LIF,

the temperature sensitivity will be even lower than that of RhB alone. For the two-color/two-dyes LIF, it is common practice to select one fluorescent dye with strong temperature dependence and the other with little or no temperature dependence. The temperature sensitivity is mainly dictated by the temperature dependent dye. Typically RhB is selected as the temperature dependent dye and either Rh110, sulforhodamine101 or Rh560 as the non temperature dependent dye (Sakakibara and Adrian, 1999). Although there are many benefits of using the two-color LIF technique, the temperature sensitivity is similar that obtained by the one-color LIF technique. To increase the temperature sensitivity, the quantum yield of the selected emission bands (ϕ_1 and ϕ_2) must be comparable, and their temperature dependence must differ significantly (Sakakibara and Adrian, 1999);

$$\frac{d\phi_1}{dT} \gg \frac{d\phi_2}{dT} \text{ or } \frac{d\phi_1}{dT} \ll \frac{d\phi_2}{dT} \tag{3.13}$$

Since $d\phi/dT$ is negative for most organic fluorescent dyes, the challenge is to find a suitable dye with a positive temperature dependence. Sutton (Sutton et al., 2008) proposed the use of a new dye combination composed of FL27 as a positive temperature dependent dye, with $d\phi_{FL27}/dT > 0$, and RHB as the negative temperature dependent dye, with $d\phi_{RhB}/dT < 0$. This dye combination presents a temperature sensitivity as high as 7%. Unlike RhB, FL27 is not used extensively, so its properties need to be studied in detail. FL27 fluorescent emission properties under different conditions are studied in this paper. In specific, effects due to changes in pH, temperature, concentration ratio, and excitation wavelength are presented.

3.4.1 LIF Dyes Sensitivity Study

An emission scan of each dye was made using a spectrofluorometer [product of Photon Technology International]. Among the advantages of this facility is its

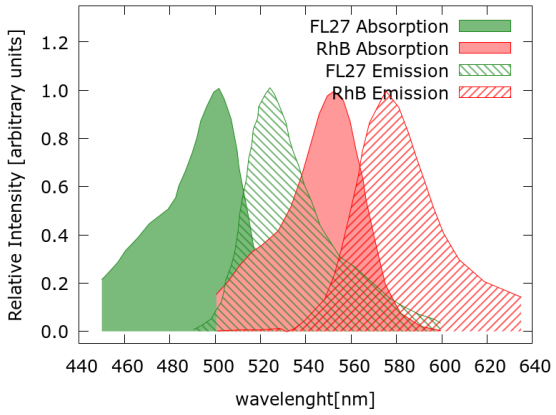

Figure 3.24: Absorption and emission spectra of RhB and FL27.

ability to excite the dye at varying wavelengths and temperatures. For accurate measurements of the fluorescent light from the dyes, an optical filter was used to block the excitation light wavelength. The optical filter blocked $\lambda_{ext} \pm 5$nm. The temperature capabilities of the spectrofluorometer allowed a temperature range from 20 to 95°C; however, to prevent damage to the dye container, a maximum temperature of 80°C was used.

3.4.2 Influence of Excitation Wavelength

An aqueous solution of FL27 and RhB dye mixture was prepared with a concentration ratio of $R = C_{FL27}/C_{RhB} = 1$, each dye having a concentration of 0.2 mg/L. Considering the absorption and emission spectra of FL27 and RhB, (see Fig. 3.24) a range of suitable excitation wavelengths were selected: 488nm, 514nm (Argon-ion lasers), 510nm (Copper-vapor lasers), and 532nm (Nd:YAG lasers).

For each selected excitation wavelength, the dyes' temperature was changed. The measured fluorescent spectrum under different temperatures is shown in Fig. 3.25. The emission spectra peaks of FL27 and RhB are about 525nm and 580nm respectively, which differ significantly enough for our purposes. From Fig. 3.25, we can

see that FL27 fluorescent emission is dependent on temperature; however, the nature of this dependence changes for different excitation wavelengths. When the excitation wavelength was short, such as 488nm (see Fig. 3.25(a)), the emission intensity decreased as temperature increased. The opposite behavior is found in the case of longer excitation wavelengths such as 526nm and 532nm (see Figs. 3.25(d)&(e)), on which the emission intensity increased with temperature. A transition region was found for excitation wavelengths in the range from 510nm to 514nm (see Figs. 3.25(b)&(c)). On these wavelengths, when the temperature is increased, the left side of the FL27 emission peak decreased, while the opposite behavior was observed for the right side of the FL27 emission peak. A common behavior of the FL27 spectrum for all excitation wavelengths is a significant right-shifting of its emission spectrum peak as the temperature increases. This indicates that although the emission spectra shows a strong temperature dependence, the right-shifting behavior must be considered to obtain high temperature sensitivities. It is desired to select emission spectral bands that are stable and that change monotonically with temperature. For the excitation wavelength range λ_{ext} = [526nm to 532nm], a positive temperature dependence ($dI/dT > 0$) is found for most of the FL27 spectrum. Similarly, a negative temperature dependence ($dI/dT < 0$) of FL27 spectrum is observed for the excitation wavelength of $\lambda_{ext} = 488$. The emission spectrum range λ_{ext} = [510nm to 515nm] is considered a transitional range, because within this range, FL27 temperature dependence changes from a negative to a positive value. The FL27 emission spectra property of presenting both positive and negative temperature dependence at different excitation wavelengths makes FL27 an excellent dye to implement LIF thermometry, providing more flexibility depending on the application. The FL27 positive temperature dependence response is particularly important, because with a proper fluorescent dye match (Rhodamine-B), it can improve the temperature sensitivity of the two-color/two-dye LIF thermometry.

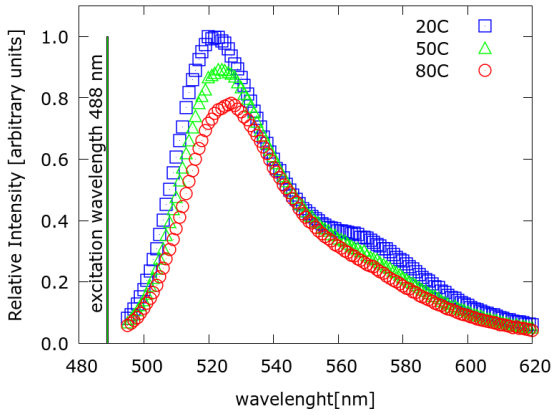

Figure 3.25: Emission spectra under different temperatures and an excitation wavelengths of λ_{ext}= 488 nm.

The different absorption spectra of RhB and FL27 (Fig. 3.24) give rise to different emission intensities of FL27 and RhB, depending on the excitation wavelengths. For the same dye concentration, the emission intensity of one dye may play a dominant role so as to make the emission intensity of the other negligible. Therefore, depending on the excitation wavelength used, the concentration ratio between the dyes must be adjusted; for example, when using a short excitation wavelength, more RhB (compared to FL27) is needed.

3.4.3 Temperature Sensitivity

As mentioned before, the largest temperature sensitivity of the two-color/two-dye LIF technique is obtained when $d\phi_1/dT > 0$ and $d\phi_2/dT < 0$. To obtain such behavior with a FL27 and RhB solution, an excitation wavelength of 527 or 532 (green light) can be selected, on which FL27 has a positive dependence on temperature ($d\phi_{FL27}/dT > 0$), and RhB has a negative dependence on temperature ($d\phi_{RhB}/dT < 0$). With these excitation wavelengths, the main emission spectra (>10% of the peak intensity) of FL27 is within 500-580nm with a peak located at

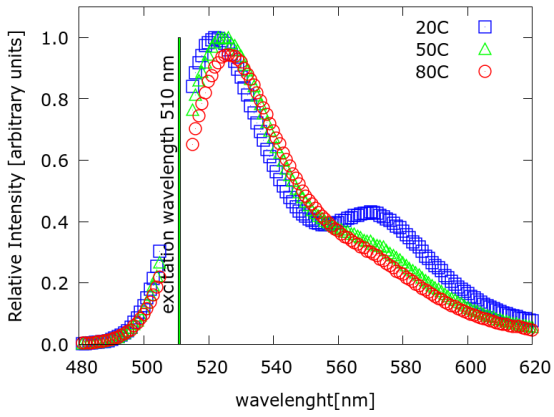

Figure 3.25: Emission spectra under different temperatures and an excitation wavelengths of λ_{ext}= 510 nm.

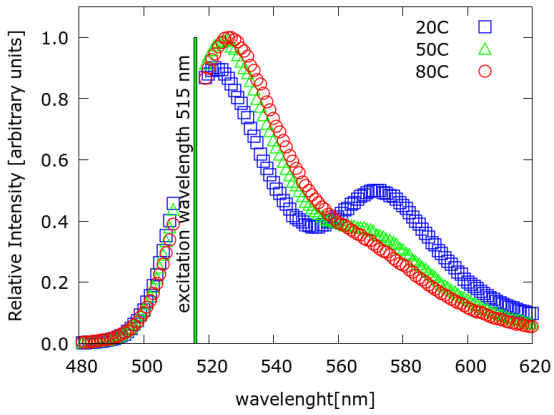

Figure 3.25: Emission spectra under different temperatures and an excitation wavelengths of λ_{ext}=514 nm.

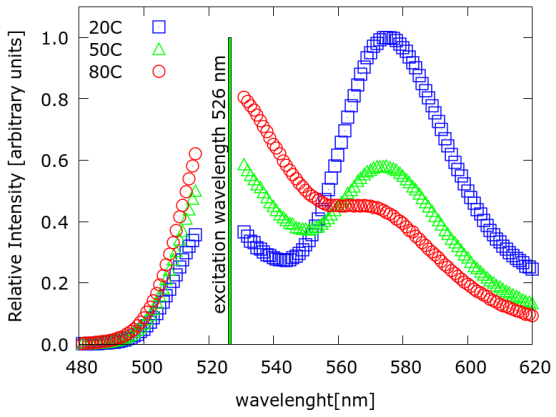

Figure 3.25: Emission spectra under different temperatures and an excitation wavelengths of λ_{ext}=526 nm.

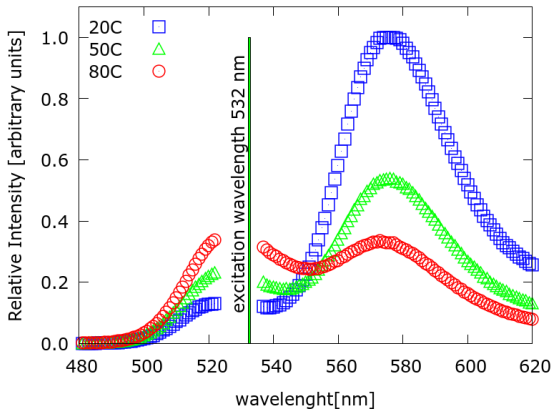

Figure 3.25: Emission spectra under different temperatures and an excitation wavelengths of λ_{ext}=532 nm.

530nm. For RhB, the main emission spectra is within 540-660 and its peak is located at 580nm. There is an "overlapping" region (from 540 to 580nm), in which the fluorescence emission intensity is influenced by the contribution from both dyes. The individual contribution from each dye is dependent on the concentration ratio, and the excitation and emission wavelengths. Emission at wavelengths close to 580nm will be more influenced by RhB, while wavelengths closer to 530 will be more influenced by FL27. The two-color LIF thermometry works better when each of the emission spectral bands selected to perform the ratio are influenced by a single dye only; therefore, it is common practice to avoid selecting emission bands that are close to the "overlapping" region center. The selected bands must have a large and stable response to temperature (always increasing or always decreasing with temperature). For RhB the selection of a suitable band is straightforward, because its emission peak is close to the edge of the "overlapping" region, where there is little influence from the FL27 emission. However for FL27, the spectrum band selection presents more challenges. The peak of FL27 is close to the excitation wavelengths (527 or 532nm), which will induce errors in the temperature measurements. Therefore, there are two options: select wavelengths on the left or right side of the FL27 peak, in such a way as to avoid the influence of the excitation light. When an excitation wavelength of 527nm is used, the two recommended bands for FL27 are: left side, from 500 to 516nm, and right side, from 531 to 550nm. When using an excitation wavelength of 532nm, the left and right bands are from 500 to 522nm and from 537 to 550nm, respectively.

The effect of temperature on the whole-spectrum intensity ratio ($R = I_{RhB}/I_{FL27}$) with λ_{ext}= 532 is shown in Fig. 3.26(a), while that of λ_{ext}= 527 is shown in Fig. 3.26(b).

It is important to note the gap left by the optical filter for wavelengths close to

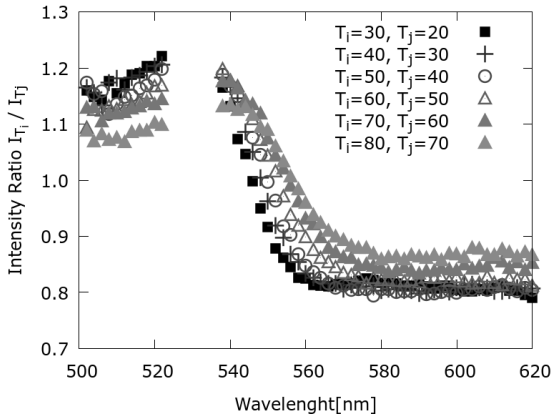

Figure 3.26: Intensity ratio for different temperature cases and λ_{ext}=527 nm.

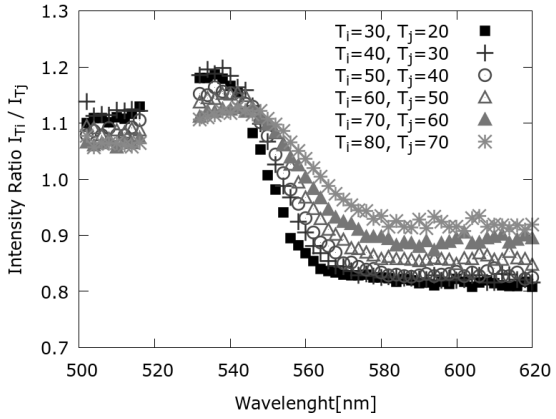

Figure 3.26: Intensity ratio for different temperature cases and λ_{ext}=532 nm.

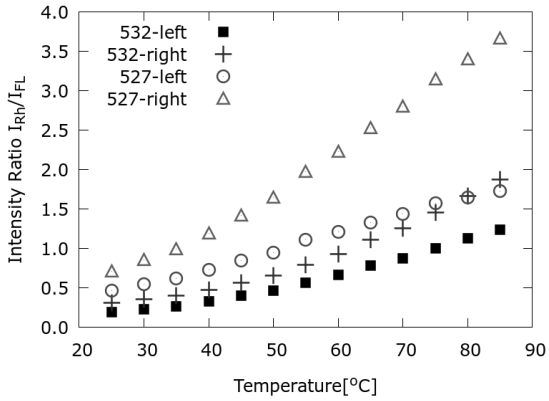

Figure 3.27: Intensity ratios of FL27 and RhB.

the excitation wavelengths. Although this data shows that all wavelengths can be used for LIF thermometry, a higher temperature sensitivity is obtained when avoiding wavelengths in the "overlapping" regions. Considering this, the intensity ratio is calculated using only the light within the bands mentioned previously. The effects of temperature and excitation wavelength on the intensity ratio of the selected bands are shown in Fig. 3.27. The temperature sensitivities are calculated based on Fig. 3.28.

The results show that the temperature sensitivity is about 4%, and better than that of RhB alone. This further confirms the choice of the RhB and Fl27 solution. The characteristics of the FL27 selected emission bands are different for the excitation wavelengths considered. For $\lambda_{ext} = 526$nm, the right band is preferred because it presents a higher temperature sensitivity with a high emission intensity, which is good if a CCD sensor is used to detect the emitted light. For $\lambda_{ext} = 532$nm, a more careful selection of the FL27 emission band is required, one which is based on the temperature measurement scope. For low temperatures ($< 50^o$C) the left band presents a higher temperature sensitivity than the right band, while the opposite

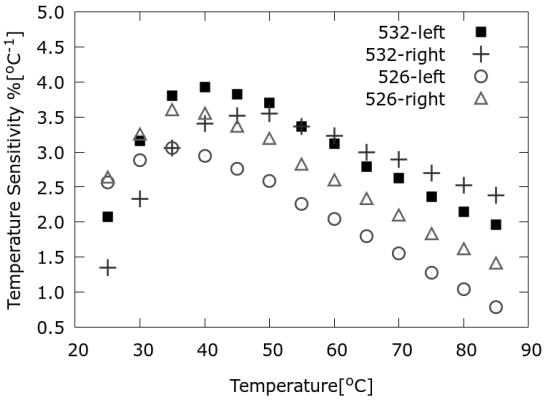

Figure 3.28: Temperature sensitivity for different cases.

behavior is observed for higher temperatures ($> 50^oC$), Comparing both excitation wavelengths, a higher performance is obtained when using λ_{ext}=532, especially in the high temperature cases.

3.4.4 Influence of pH

The emission intensity of the RHB and FL27 solution is strongly influenced by pH. Fig. 3.29 shows that FL27 emission spectra are more influenced than those of RhB. Although it appears that the emission intensity of both dyes increases with pH, the RhB emission increase may be due to the FL27 contribution; therefore, it can be concluded that FL27 is the only pH dependent dye.

The pH value of a freshly made solution is usually as high as 10 or 11, and decreases to 5 after about ten days. To increase the pH, sodium hydroxide can be added to the solution. Although increasing the pH increases the emission intensity of FL27, it does not modify much the emission intensity of RhB. Therefore, a careful monitoring of pH is needed to avoid increasing the FL27 emission intensity to the point that the RHB emission peak is no longer visible or is difficult to identify. Having

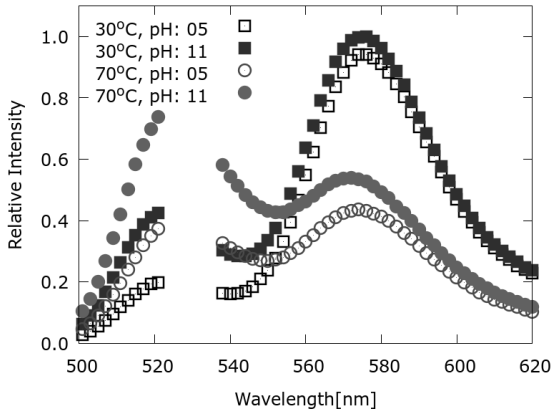

Figure 3.29: Emission spectra under different pH.

a higher emission intensity can simplify the detection of the emitted light; however, an emission intensity increase does not mean a higher temperature sensitivity. In fact, the opposite occurs, and the temperature dependence is reduced slightly (see Fig. 3.31). In addition, the pH time dependence may induce additional errors in the results as the pH value decreases with time, so low pH values are preferred.

3.4.5 Influence of Concentration Ratio

A concentration ratio value was set to unity ($R = C_{FL27}/C_{RHB}$=1). However, in most experiments, this value must be changed to obtain optimal results. Several issues should be considered to select an adequate concentration ratio. First, a high emission intensity from both dyes is required to ensure a correct detection from the CCD sensor or other optical instrumentation. Second, the emission intensities from both dyes must be of comparable value within the experimental temperature scope, which implies that both peaks should be easily detected with low or little influence between them. For example, in Fig. 3.25, the concentration ratio provides acceptable emission intensities from both dyes within the temperature range of 30-50^{o}C. If the

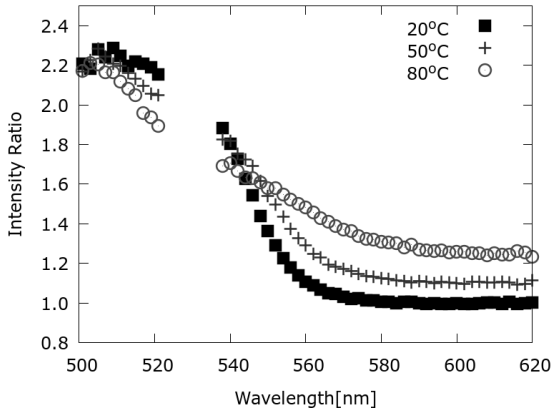

Figure 3.30: Intensity ratio under different pH.

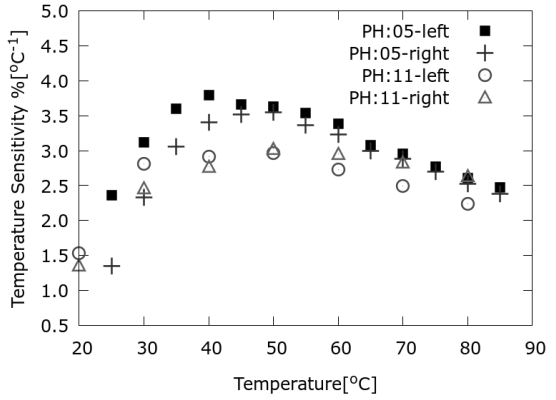

Figure 3.31: Temperature sensitivity under different pH.

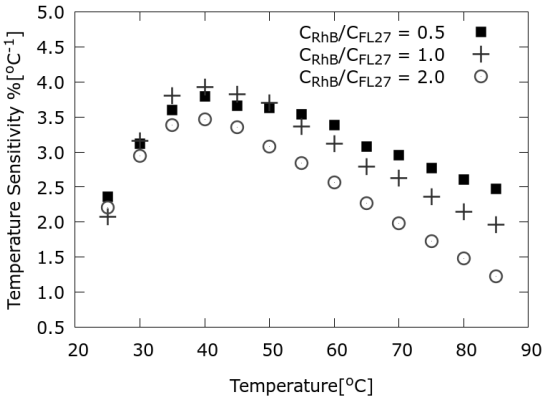

Figure 3.32: Temperature sensitivity with different concentration ratios considering the left emission band.

desired temperature scope is from 50-80^{o}C, more RhB is needed, i.e., the concentration ratio should be decreased. The selected concentration ratio value will always depend on the excitation wavelength and experimental temperature scope. An analysis of the concentration ratio influence on temperature sensitivity was developed with a constant RhB concentration of C_{RhB}=0.2mg/L, and an excitation wavelength of λ_{ext}=526nm. The FL27 concentration was changed from 0.1mg/L to 0.4mg/L to obtain concentration ratio values of CR = 0.5, 1.0 and 2.0. The results show a dependence of temperature sensitivity on the concentration ratio. Fig. 3.32(a) shows that when the FL27 left band is selected, the temperature sensitivity decreases when increasing the concentration ratio, while for the FL27 right band case, the opposite behavior is found (see Fig. 3.32(b)).

3.4.6 Advanced Two Colors or Multicolor Methods

Unlike solutions with RhB/Rh110, which have only one temperature sensitive dye and thus only require 2 bands for detection, the RhB-FL27 solution contains two temperature dependent dyes, which allows for a more flexible band selection process.

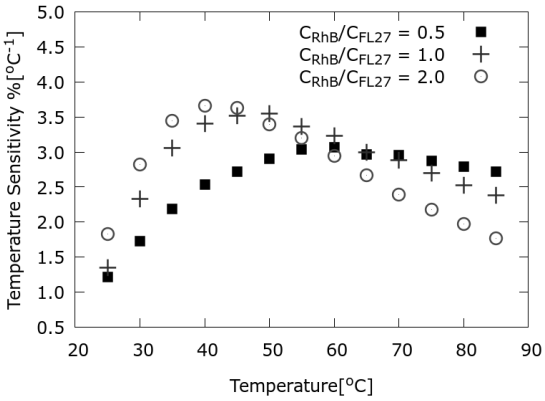

Figure 3.32: Temperature sensitivity with different concentration ratios considering the rigth emission band.

The RhB-FL27 solution can be employed as a multicolor ratiometric technique on which two or more spectral bands can be detected. To improve sensitivity, it is necessary to capture light at wavelengths that are highly affected by temperature. In the case of RhB-FL27 solutions, the left and right bands from the FL27 spectrum peak can be selected, and if possible, two more bands from the RhB spectrum peak. The selected bands are shown in Fig. 3.33, from which a temperature sensitivity up to 8% can be achieved (see Fig. 3.34). The availability of multiple bands allows researchers to perform a smart band selection. For example,Lavieille et al. (2004) presented the three-color/one-dye technique, whereby three spectrum bands (or colors) were selected to minimize specific error sources such as the influence of optical path and concentration. The bands presented by Lavielle contained the following characteristics: Band 1, with Low sensitivity to temperature and high sensitivity to absorption; Band 2, highly sensitive to temperature and absorption, and Band 3, with high sensitivity to temperature and low sensitivity to absorption. The same idea can be applied in the RhB-FL27 solution, with the selected bands shown in Fig. 3.35.

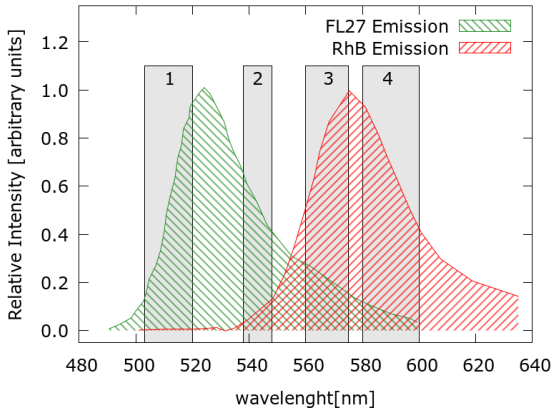

Figure 3.33: Detected bands used in multi-color method.

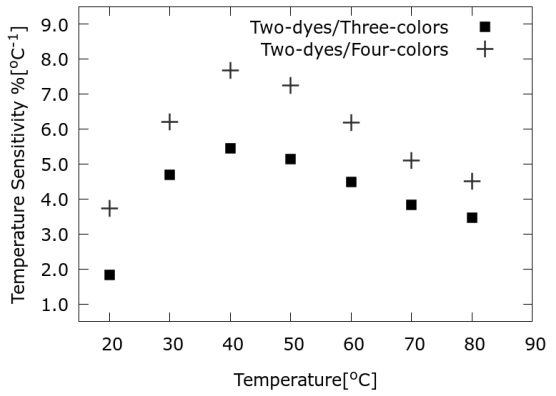

Figure 3.34: Temperature sensitivity of multicolor methods.

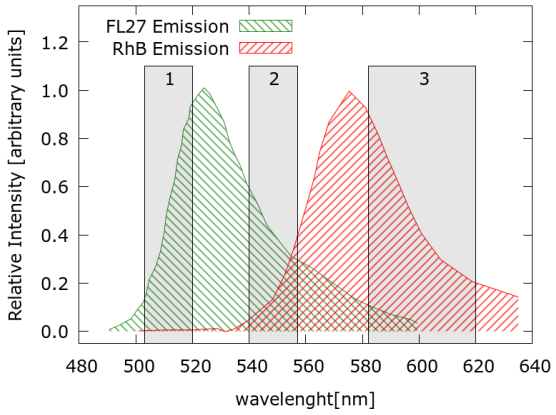

Figure 3.35: Detected bands of Lavielle's three color method.

The highlighted bands in Fig. 3.35 present the following characteristics: Band 1 from 503 to 521 nm, Band 2 from 541 to 558 nm, and Band 3 from 582 to 619 nm. Band 1 is sensitive to temperature and absorption of both dyes, especially for the FL27 absorption. Band 2 is located in the mixed emission band of both dyes, so the temperature sensitivity is quite low due to the mixed mixed effect of a negative and positive temperature dependence. The absorption peak of RhB is about 555nm, so Band 2 is sensitive to RhB absorption. Band 3 is sensitive to temperature, and the absorption cross sections of both dyes are very low at this region, so this band shows low sensitivity to absorption. These three bands can be easily measured by means of optical filters.

A sensitivity analysis on FL27-RhB solution properties tested the applicability of this solution in planar induced fluorescence (PLIF) thermometry. Emission spectra measurements were performed to test the dye solution behavior under different excitation wavelengths, temperatures, pH values, and concentrations. The temperature sensitivities under different conditions were analyzed.

Significant changes of the FL27 temperature response at different excitation

wavelengths was found. By increasing the excitation wavelength, the temperature dependence switched from a negative dependence ($\frac{d\phi}{dT} < 0$) at $\lambda_{ext} = 488$ nm to a positive dependence ($\frac{d\phi}{dT} > 0$) at a $\lambda_{ext} > 526$ nm and 532 nm (range of Nd:Yag lasers). A temperature dependence tendency was not found at intermediate excitation wavelengths ($488 < \lambda_{ext} < 526$); therefore, to obtain a high temperature sensitivity, 526nm and 532nm excitation wavelengths are preferred.

The maximum estimated temperature sensitivity was as high as 4.0% per ^oC, which is better than the widely used mixture of RhB and Rh110 (2.0% per ^oC). The emission intensities of the dyes showed them to be sensitive to pH, especially FL27. Although high pH values increased the emission intensity, the temperature sensitivity did not substantially increase; therefore, low pH values were selected. Low concentration ratios are preferred for a low temperature measurement scope (below 50^oC), while high concentration ratios are required for measurements at higher temperatures within the calibration range ($>50^oC$ and <90 ^oC).

Higher temperature sensitivities can be obtained with the advanced multicolor methods, where more than two bands are used for the LIF thermometry. The temperature sensitivity can increase to 6.0% with three bands or to 10.0% with four bands. The RhB-FL27 dye mixture is a good candidate for the implementation of the three color method promoted by Lavieille et al. (2002). With a two-dye/three-color technique, not only could the influence of Beer's absorption, laser intensity, probe volume dependencies, concentration and optical path be eliminated, but a high temperature sensitivity could also be obtained.

3.4.7 Validation of the Simultaneous LIF and PTV Measurements

In this section, an improved 2-D PTV-LIF technique is presented for the simultaneous measurement of temperature and velocity fields of cavity flows. 2-D Whole-Field

temperature measurements are achieved by the two-color/two-dyes laser-induced fluorescence (LIF) technique, while the 2-D velocity is measured with particle tracking velocimetry (PTV) method. The improvements presented in this work is the modification of the commonly selected dyes to achieve the two-color LIF technique. Traditionally the organic dyes used to perform two-color LIF measurements are Rhodamine-B and Rhodamine-110, Rhodamine-B provides a fluorescence emission dependent on temperature while Rhodamine-110 provides an emission independent of temperature. In this work, Rhodamine-110 is replaced by Fluorescein-27, which provides a second temperature dependent dye. By using two temperature dependent dyes, the temperature sensitivity of the technique is increased. Also, in this work, a sensitivity analysis of the RHB-FL27 solution properties is presented, and its application to a natural convection two-phase flow within a cavity is explored.

3.4.7.1 Experimental Arrangement

The experimental facility was designed for simultaneous PTV and LIF measurements. Detailed description of the test facility and visualization system are given next.

The test section is shown in Fig. 3.36. The fluid container is a solid octagon made of transparent acrylic with a cylinder of 16 mm drilled in its center. This design was selected to accomplish multiple optical access and to provide enough insulation through the cylinder walls. The top and bottom of the hollow cylinder can be closed with stainless steel rods. This rods are heated or cooled to induce heat transfer only through the top and bottom of the cylinder. Each rod contains six thermocouple holes to achieve transverse and lateral temperature measurements within the rods. The thermocouple measurements also helps to estimate the heat induced to the fluid. The heating element is a cartridge heater with a PID temperature controller. The

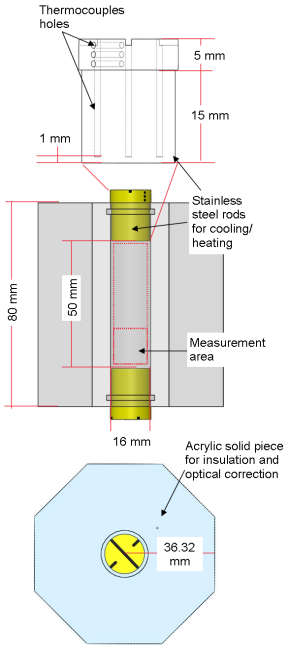

Figure 3.36: Test facility arrangement.

cooling element is an aluminum heat exchanger receiving cold water from a water bath. The heater can reach temperatures in excess of 300 ^{o}C, while the water bath temperature range is within 5 to 90 ^{o}C. The limiting aspect of this facility is the test section itself. The recommended working temperatures for acrylic does not exceed 80 ^{o}C. The test section was designed to achieve an L/d $\approx$ 3

The visualization system consisted of a high-speed high-resolution camera, a high-energy laser, mirrors, lenses, optical filters, and a beam splitter. The high-speed camera has a maximum frame rate of 4,700 fps at a resolution of 800$\times$600 pixels, with a maximum bit depth of 12 bits. The illumination was provided by a Spectra-Physics dual lamp Nd:Yag laser which can operate at a maximum power of 400 mJ/pulse. The maximum pulse rate from each lamp is 30 pulse/s. The pulse interval between the two lamps (Δ_{PIV}) can be adjusted to achieve faster frame rates. Two optical

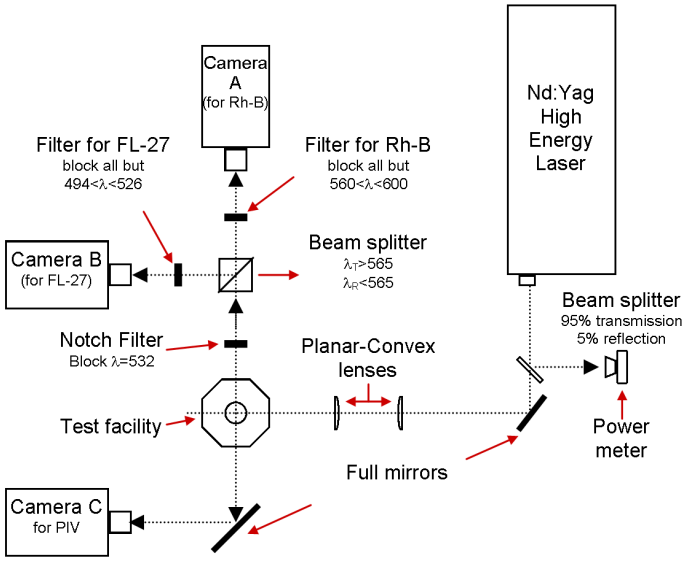

Figure 3.37: Arrangement of the optical system.

mirrors and two plane-convex lenses are used to convert the small circular beam from the laser, into a 1 mm thick sheet of light. The laser light sheet is positioned on the measurement region, parallel to the cameras focal area. The test facility is mounted on a translational stage to have the capability of changing the measuring region while keeping the visualization system unaffected. For the PTV velocity measurements, the fluid is seeded with highly reflective particle tracers with a density similar to that of the water. The average PIV particle diameter is 10 μm. Fig. 3.37 shows the schematics of the visualization system. For the LIF-Thermometry, RhB and FL27 are disolved in distiled water with a concentration of 0.8 and 1.6 g/L respectively. The optical arrangement shown in Fig. 3.37 allowed for the LIF Camera A to capture the light emitted nearby the center of the maximum emission of RhB, from about 565 to 600 nm, while the LIF Camera B captured the fluorescent light emitted on the left part of the emission peak of FL27, from about 500 to 525 nm. A third high speed color camera (Camera C) is used to capture all the light coming from the PIV particles

reflections and the fluorescent light from the dyes. Several experimental conditions were used, firstly to achieve an estimate of the temperature measurements errors, secondly to test the LIF technique on different experimental situations. Namely these experiments are: Temperature calibration experiments; Stratified experiments; Natural circulation experiments and Boiling Experiments.

3.4.7.2 Calibration Experiments

From the calibration experiments, a relationship between fluorescent emission intensity and temperature is to be determined ($I = f(T)$). Experimental variations, even subtle ones, can induced large differences on the LIF temperature calibration. Differences on materials, viewing angles, distance and magnification, are factors that influence the amount of light from the measurement region to the optical sensor. Therefore careful experimental calibrations are to be performed. For this particular setup, the common practice to perform calibration experiments was to set the bottom and top rods to isothermal condition. This conditions were kept for two hours to ensure steady state, i.e., until the same temperature in the whole measurement domain was achieved. After the steady state waiting time, 500 images were acquired from which an average image was obtained for each temperature. This procedure was repeated for as many calibration points were desired. The calibration temperature ranged from 30 to 90^{o}C. Fig. 3.38 shows the experimental calibration results from both cameras: RhB (left) and FL27 (right). From these average images a clear temperature tendency is found. By obtaining an average gray-scale value from each calibration image, a calibration function is obtained. Fig. 3.39 shows the temperature dependence of the RhB and FL27 average fluorescent intensity. From this figure, it is clear that $d\phi_{RhB}/dT < 0$ and $d\phi_{RhFL27}/dT > 0$. This is a good indication that Eq. (3.12) is well satisfied, this means that the ratio dI_{RhB}/dI_{Fl27} has a higher temperature sensitivity

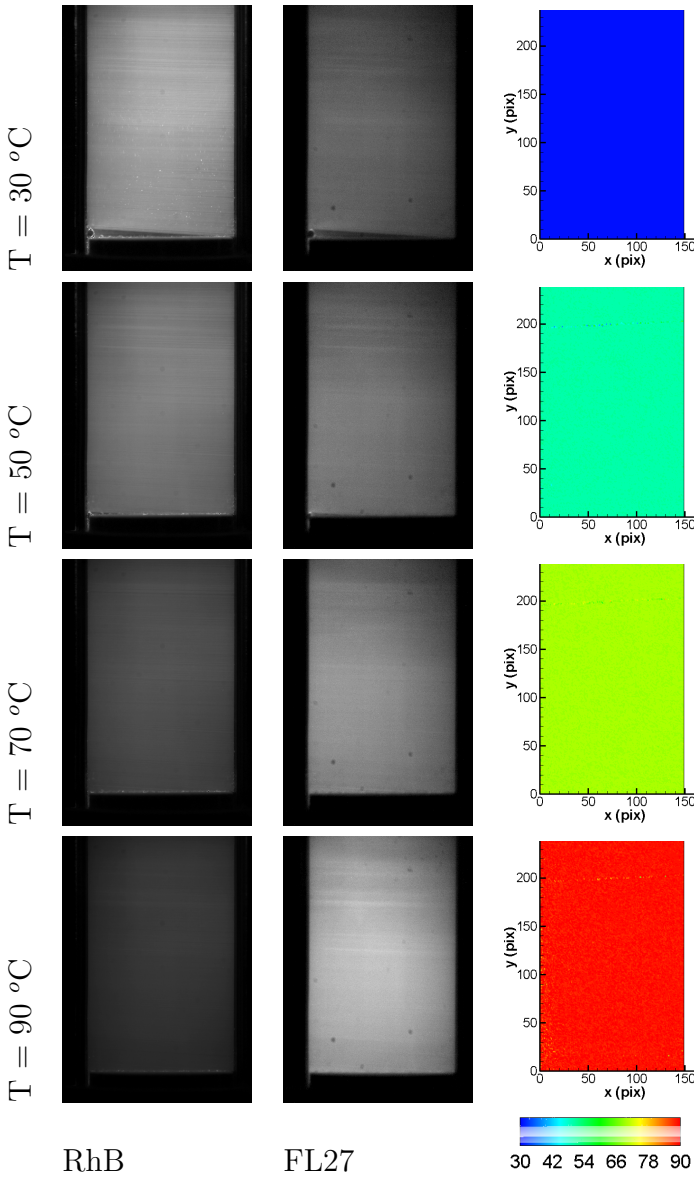

Figure 3.38: LIF experimental results.

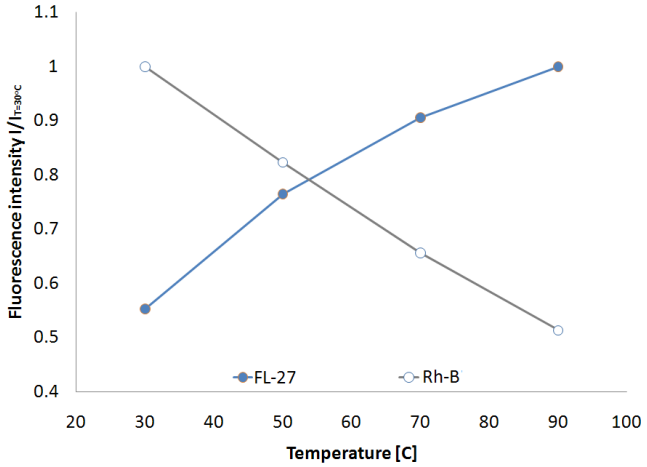

Figure 3.39: Variation of the fluorescence intensity dependent on temperature.

than that of RhB or FL27 alone. Fig. 3.40 shows the functional dependence of the intensity ratio I_{RhB}/I_{FL27}, also it is shown a power function that fits the data with a R^2=0.99. Although the process of performing the ratio I_{RhB}/I_{FL27} helps to reduce the effects of laser light fluctuations, Camera A and Camera B (For RhB and FL27 respectively) individual defects are not corrected. This defects may be due to burned pixels on the CCD sensors, or from uneven illumination captured by one camera only. To fix this problem it is common practice to normalize the output of each camera using the images obtained from the lowest or the highest temperature case. Another technique to reduce discrepancies on spatial illumination due to individual camera defects, is to utilize multiple calibration curves. The amount of calibration curves is limited by the number of pixels on the images. To have a single calibration curve per pixel is an ideal situation, although it requires a large amount of computer memory and time. Therefore it was decided to divide the image in a grid on which each cell contains a single calibration curve obtained from the pixels clustered within the grid cell. An automatic routine to obtain the calibration curves was developed,

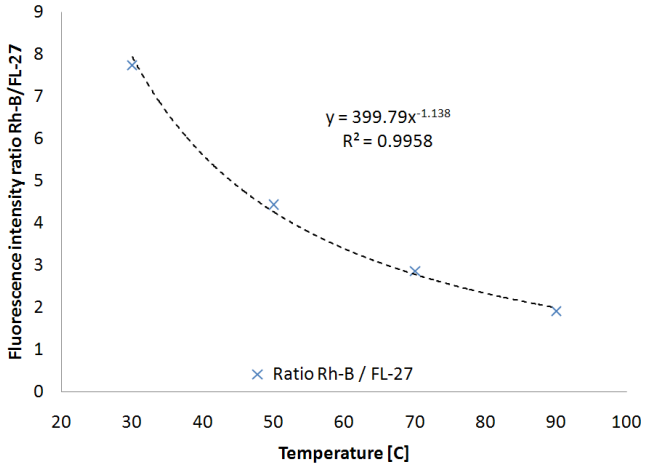

Figure 3.40: Ratio between two CCD camera's output against temperature.

with the option to fit a polynomial or a power function for each cell (or pixel). The calibration experiments were performed five different times to test for repeatability. The temperature measurements and the calibration curves discrepancies accounted for less than 5%. This is a good indication that the dye solutions can be heated and cooled in multiple occasions without hindering the fluorescent emission intensity and behavior. Although the previous statement is true, attention is needed when the liquid volume is small. Photo-bleaching effects becomes significant when a small amount of dyes are present. For this cases an anti-Photo-bleaching agent is needed to reduce the influence of photo-bleaching.

3.4.7.3 Stratified Experiments

On this set of experiments it is intended to obtain density stratification by heating the top stainless steel rod and cooling the bottom rod. The temperatures were respectively 90 and 20 ^{o}C. This experiment was conceived as a simple way to test the applicability of the technique on a fluid subject to a large temperature gradient. Fig. 3.41, shows the results of applying the correction to remove the effects of uneven

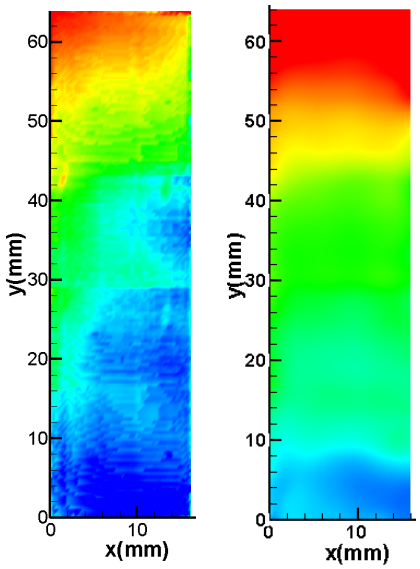

Figure 3.41: LIF analysis on density stratification (a) without correction, (b) with normalization correction.

illumination (normalization with the lowest temperature image). In Fig. 3.41(a) the non uniform distribution of light produces a lack of radial temperature symmetry; the liquid on the cylinder's left side appears warmer than that on the right side. Fig. 3.41(b) shows the corrected results where the lack of radial symmetry was reduced.

3.4.7.4 Natural Circulation Experiments

Natural Circulation Experiments were performed by heating the bottom stainless steel rod and cooling the top rod. The temperatures ranged from 10 to 90 ^{o}C. This particular setup produced flow instabilities that allowed natural circulation to happen. The measurement area selected is a region of 16×27 mm^2, this region was positioned close to the bottom of the test section, just above the bottom heating rod (see Fig. 3.36).

Fig. 3.42 shows the average velocity and average temperature within the flow

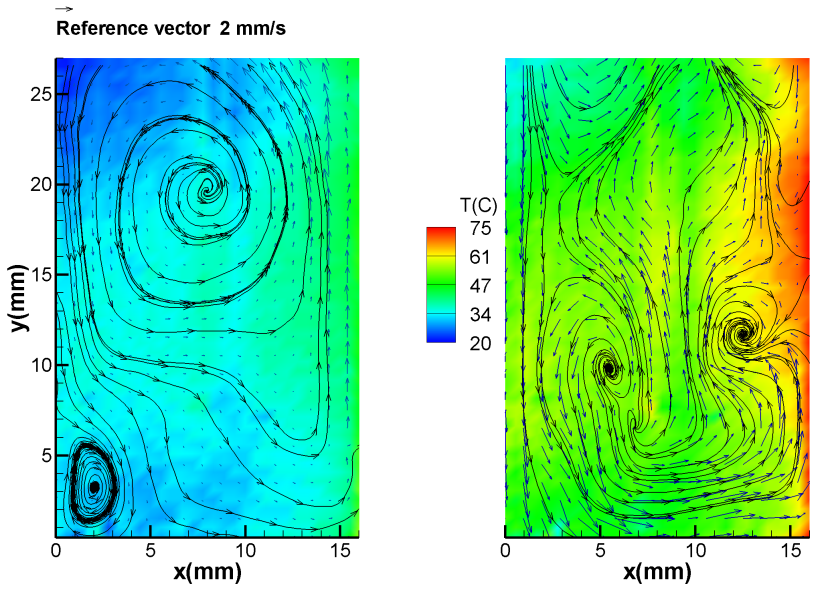

Figure 3.42: Contour plot of the temperature and velocity fields for the conditions: a) $T_{top} = 10^{o}$C with $T_{bot} = 80^{o}$C, and b) $T_{top} = 10^{o}$C with $T_{top} = 50^{o}$C.

domain. for the lower temperature case (Fig. 3.42 (b) the level of turbulence is lower, and larger coherent structures regions can be observed. the higher temperature case (Fig. 3.42 (a)) shows a more chaotic behavior on which the structures tend to be of smaller dimensions. Although the magnification used does not allowed for the near-wall thermal boundary layer to be resolved, there is a global tendency on both cases for the hotter lighter fluid to move upward on the right side of the cylinder; and the colder heavier fluid to move downward through the left side of the cylinder.

3.4.7.5 Boiling Experiments

The applicability of the PTV-LIF technique was tested in boiling conditions, the process of heating the bottom rod and cooling the top rod was repeated, the bottom rod maximum temperature was 130 C, on which some degree of boiling was present.

The reason why LIF is not commonly used on two-phase flows is due to the different refractive index of the phases involved. When light pass through the contact surface between two materials of different refractive index, the light suffers drastic changes on its direction due to refraction, reflections and dispersion of the light. This phenomena is observed on the bubbles-liquid boundaries. The irregular and changing shapes of the bubbles during the boiling process, deforms the incident laser light sheet, and produces shadows or a dimmed illumination on regions behind the bubbles; frequently, the bubble surface geometry can refract the light as to produce a volume illumination behind the bubbles. These effects are observed in Fig. 3.43, where bubble shadows and volume illumination are present. The influence of the optical distortions on the LIF temperature measurements are reduced inherently on the two-color/two-dyes LIF technique. The two LIF cameras can capture simultaneously these optical distortions. Optical distortions can be treated as laser intensity fluctuations, or as an uneven illumination on the images. Therefore, by applying the ratiometric technique on the two-phase flow images (I_{RhB}/I_{FL27}), the spatial non-uniform illumination is reduced, and temperature measurements can be estimated even in regions close to the bubbles. The correction process for the boiling images is therefore the ratio (I_{RhB}/I_{FL27}), and is shown in Fig. 3.43. These images are animations showing the ratiometric process. The ratio I_{RhB}/I_{FL27} is performed with the FL27 information shifted as to show bubble's shadows and reflections at the beginning of the animation. The resulting image at the end of the animation, is the final result of the ratiometric technique, where the effects of shadows and reflections are significantly reduced. Fig. 3.43(a) shows the image processing to perform the ratio I_{RhB}/I_{FL27}, while Fig. 3.43(b) shows the temperature results of this procedure.

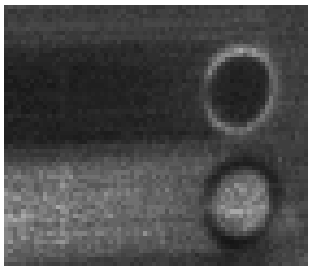

(a)

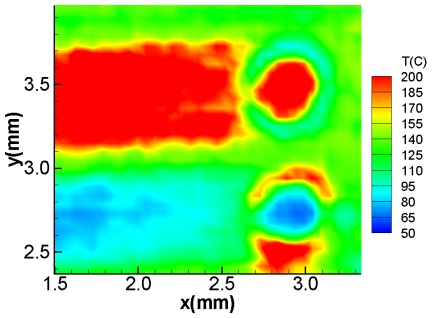

(b)

Figure 3.43: LIF applied on two-phase flow conditions.

3.4.7.6 PTV-LIF Implementation Remarks

This work presents a feasibility study to implement an improved PTV-LIF technique for simultaneous temperature and velocity measurements. The novel approach on this work is the use of a RHB-FL27 solution. To the knowledge of the authors, this solution was not previously used for simultaneous velocity and temperature measurements. Furthermore, in this work is presented a sensitivity study to understand the RHB-FL27 fluorescent emission response to different excitation wavelengths and temperatures, from which a concentration ratio of C_{RHB}/C_{FL27}= 0.5 was selected for the temperature range of interest and for an excitation wavelength typical of a PIV laser system (Nd:Yag Laser). PTV-LIF was successfully used for the simultaneous measurements of single-phase natural convection flows, and its application to boiling

flows was also explored. Remaining work is the comparison of experimental results and numerical simulations that are now undergoing at Texas A&M University. The aim of this work is the future use PTV-LIF on a subcooled boiling flow experiment.

4. SUBCOOLED BOILING FLOW EXPERIMENTS

The experimental facility was designed for the visualization of subcooled boiling flow of refrigerant HFE-301 (3M Novec-7000) at low system pressures. The facility consists of a hydraulic loop and a visualization system. Experimental setup details are given in the following sections.

4.1 Hydraulic Loop

The hydraulic loop consists of an external loop and a test section, both designed to withstand temperatures in excess of 100 °C, and pressures up to 100 psi. The external loop provides thermal and hydraulic steady state conditions. The system excess energy is removed with a small plate heat exchanger connected to a chilling system. This allowed us to have control of the inlet temperature to the test section. Liquid conditions such as volumetric flow rate, temperature, and density were measured by a Coriolis flow meter and controlled by adjusting the test section valves. The test section is a rectangular channel made of transparent polycarbonate, with 30.5 mm length and a cross-sectional area of 10×10 mm. Energy for boiling is provided through a transparent ITO heater with a length and width of 25.5 cm and 9 mm, respectively, and a maximum working temperature of about 150 °C. The heater is attached to the lateral interior face of the channel (see Fig. 4.1).

The electric current to the heater is provided and adjusted by a DC power supply. To reduce heat losses to the ambient, the test section was covered with an insulation box. Three walls of the insulation box were made of transparent acrylic and the fourth wall was a sapphire window.

The insulation box material was selected as to provide visual access for both the

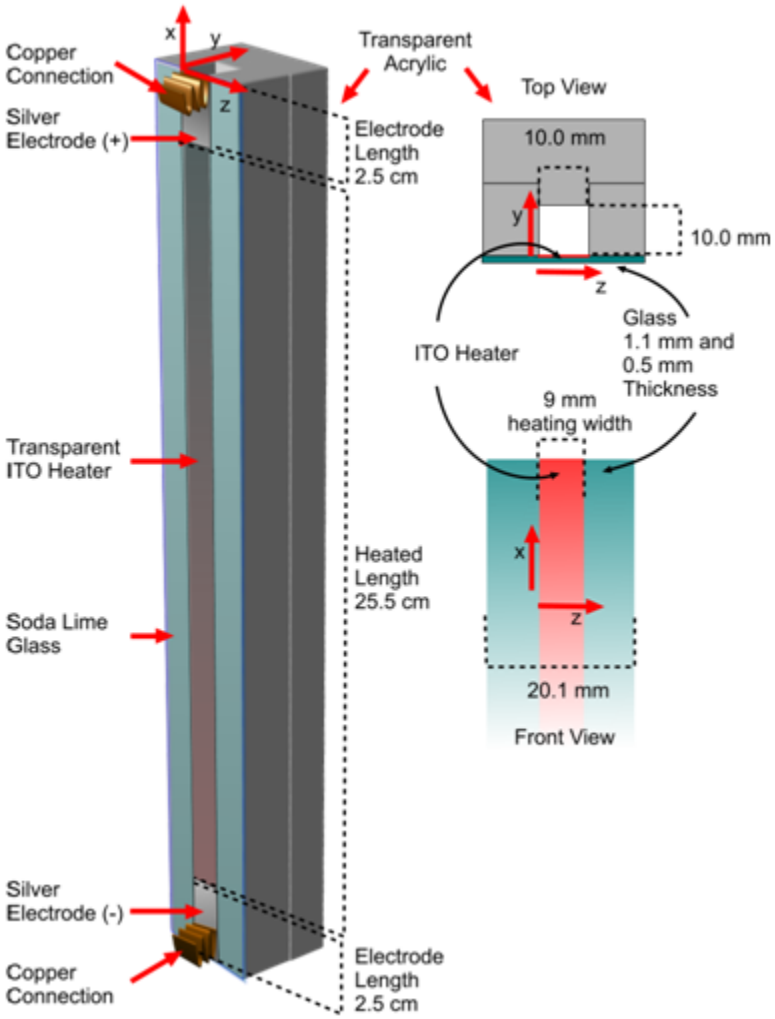

Figure 4.1: Test section schematics and dimensions.

Table 4.1: Measurement equipment ranges and uncertainties.

Equipment	Parameter	Range and uncertainties
Coriolis flow meter	flow rate $[m^3/s]$	$\dot{Q}_l$ ±0.05% of value
Thermocouples	temperature $[°C]$	T_{in}, T_{out}, T_{amb} ±0.5°C
Differential pressure 1	pressure drop [Pa]	dP_1±0.25% (full scale)
Differential pressure 2	pressure drop [Pa]	dP_2±0.5% (full scale)
Gage pressure 1	gage pressure [Pa]	P_{in}±0.25% (full scale)
Gage pressure 2	gage pressure [Pa]	P_{out}±0.25% (full scale)
Power supply	heating power [W]	$\dot{q}$ ±1.1% (full scale)

IR-camera [1] and the High speed cameras. An unheated length of about 61 cm was considered before the test section (i.e., $L_u/D_h \approx 61$) to ensure fully developed flow. To measure the heater wall temperature, a mid-wave infrared high-speed camera (3-5 μm) was used. To provide validation for the infrared camera measurements, K-type thermocouples were attached to the external face of the heater. The test section fluid inlet (T_{in}) and outlet (T_{out}) temperatures were measured with two fast response T-Type thermocouples. Ambient temperature (T_{amb}) fluctuations were measured with J-Type thermocouples. Fig. 4.1 shows the schematics and dimensions of the test section. To account for the pressure drop through the test section, two differential pressure transducers were used. Also, the gage pressure was measured at the entrance (P_{in}) and at the outlet (P_{out}) of the test section. The parameters uncertainties are provided in Table 4.1.

4.1.1 Visualization System

The visualization system consisted of three high-speed high-resolution cameras, two for front view shadowgraphy experiments, and one for side view PTV/Shadowgraphy measurements, a high-speed high-power laser, a high-speed infrared camera, a fast

[1]The optical saphire window used in this work provided almost 95% transparency to the infrared wavelengths of interest.

response LED illumination system, mirrors,translational stages, lenses, optical filters, particle flow tracers, and a laser power meter. The flow tracers were fluorescent particles with a density range between 1.39 to 1.41 g/cm, with an average particle diameter of 5 μm. Illumination was provided by a Pegasus dual lamp laser which can operate at a maximum power of 27 mJ/pulse and can achieve a maximum pulse rate of 20,000 pulses/s. Two optical mirrors and two concave-convex lenses are used to convert the small circular beam from the laser into a thin sheet of light. The laser light sheet was positioned on the measurement region, parallel to the camera focal area. The LED system is externally synchronized to be used as the shadowgraphy illumination. The cameras, mirrors and lenses are mounted on translational stages in order to have the capability of changing the measuring location within the test section. Fig. 4.2 shows the schematics of the visualization system. The High speed cameras, the laser and the LED illumination system are synchronized in such a way as to be able to obtain quasi-simultaneous PIV and Shadowgraphy measurements.

4.1.2 Temporal Multi-Scale Approach

The configuration shown in Fig. 4.2 was designed as to allow multi-orientation and multi-scale measurements. The high speed PTV/Shadowgraphy camera is arranged to provide "semi-simultaneous" measurements of PTV and shadowgraphy. This is achieved by synchronizing the camera shutter with alternating pulses of laser and led illumination. From the temporal multi-scale point of view, the PTV/Shadowgraphy camera can be configured to run in Continuous or in Straddling timing modes. Continuous mode provides a fixed time interval between consecutive frames. In order to properly capture the fast moving features within the flow, this time interval (Δt_{PTV}) needs to be small and consequently the camera need to be run at high speeds. Due to the camera memory limitations the Continuous timing mode provides short

measuring times on the order of seconds. This limited measuring time also limits the capability of measuring accurately time-average flow quantities. The Straddling timing mode combines a small time interval (small Δt_{PTV}) between image pairs plus a waiting period which will be called straddling time ($\Delta t_{Straddling}$) . This waiting period is required to achieve a higher number of independent samples for better statistics. Similarly, the two high speed shadowgraphy cameras can also be configured to work in either Continuous or in Straddling timing modes. Fig. 4.3 shows schematics of the timing used to achieve " semi-simultaneous " PTV and Shadowgraphy images. The green squares represent camera frames illuminated with the PIV laser, while the gray squares represent the camera frames illuminated only with the LED lamp. The white squares represent the "waiting" period or straddling time ($\Delta t_{Straddling}$). As shown in Fig. 4.3, the "semi-simultaneous" PTV/Shadowgraphy experiment consists of sets of four frames each. Two frames for PIV and two frames for shadowgraphy. The time interval between a PIV and a Shadowgraphy frame is given by $\Delta t_{PTV}/2$.

4.1.3 Spatial Multi-Scale Approach

To achieve spatial multi-scale measurements, the PTV/Shadowgraphy camera, or camera 1, was equipped with a telecentric lens which allowed two different magnification modes: High and medium, which corresponded to a resolution of 4.8 and 17.5 μm respectively. This camera was oriented to provide side-view measurements. The two shadowgraphy cameras (camera 2 and 3) were configured to provide front-view measurements. Camera 2 delivered front-view high magnification while camera 3 allowed for front-view low magnification, with a resolution of 186.8 μm/pixel and 32.8 μm/pixel respectively. Focus will be given to the results from the medium-magnification PTV/Shadowgraphy camera which provides simultaneous information from both phases (liquid and vapor). The cameras arrangement is summarized in

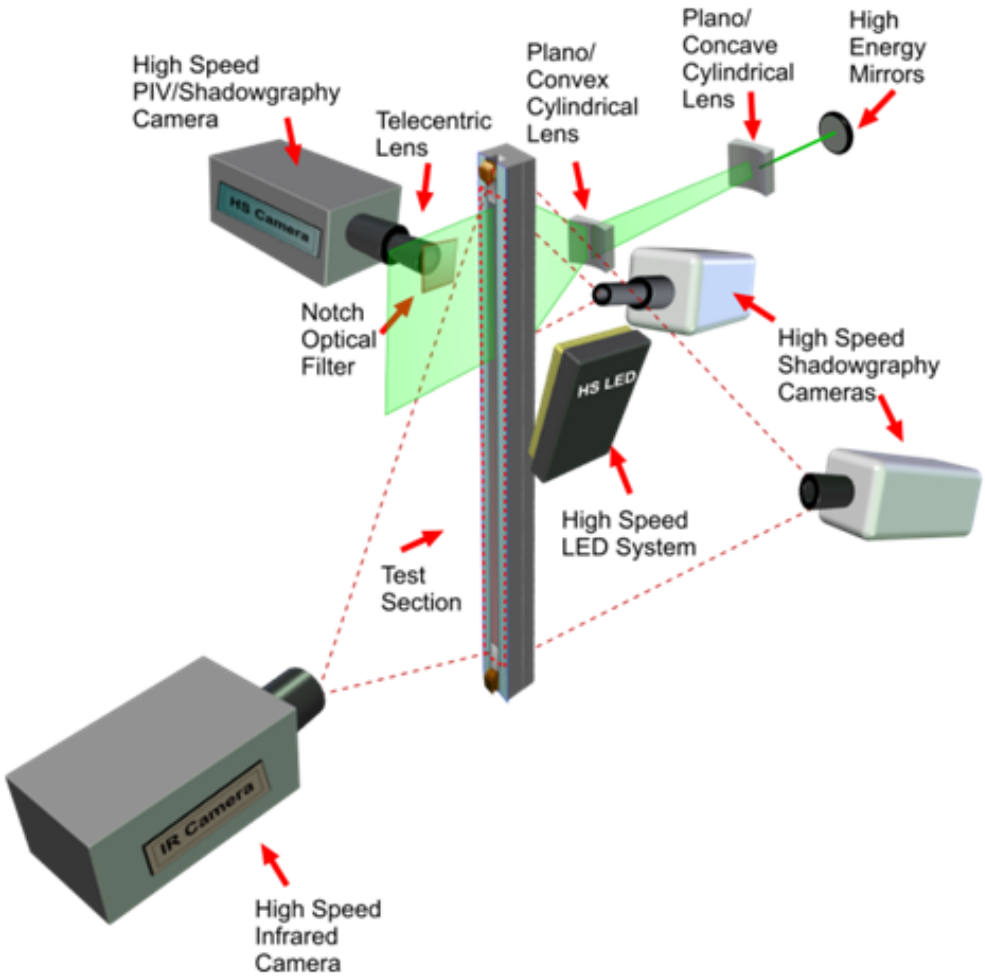

Figure 4.2: Visualization system schematics.

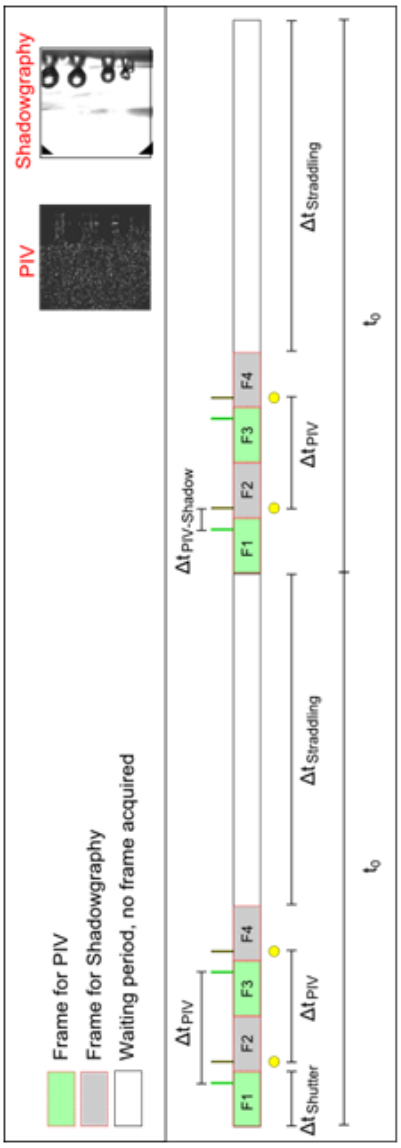

Figure 4.3: Timing configuration for semi-simultaneous PIV/shadowgraphy measurements.

Table 4.2: Camera Arrangement.

	Orientation	Magnification	μm/pix
Camera 1	Side View	High	4.8
		Low	17.5
Camera 2	Front View	High	32.8
Camera 3	Front View	Low	186.8
IR Camera	Back View	Low	190.0

Table 4.2.

The experimental setup described above allows for a set of unique experimental features relevant for two-phase flow measurements. These are summarized next:

Simultaneous whole-field measurements of liquid and bubbles parameters.

- The simultaneous application of PTV and Shadowgraphy techniques provides measurements of the liquid and bubbles velocities, along with measurements of parameters that describe the bubbles dynamics. This methodology simplify the quantification of the local void influence on the liquid turbulence.

- Improved liquid velocity measurements can be achievedwith the use of the shadowgraphy information to remove spurious vectors found within the domain occupied by the boiling bubbles. i.e., liquid velocity vectors should not exist within the bubbles volume.

- Fluorescent seedings and optical filters helped to reduce the bubbles induced laser light reflections. It is known that bubbles induced reflections accounts for large percentage of undesired noise in the PTV images.

The use of a relatively long and transparent heater for boiling.

- Thermal and hydraulic fully developed boiling flows were achieved.

- Improved optical access. The transparent heater allowed for an additional window for either: flow visualization or illumination.

Spatial and temporal multi-scales measurements.

- The availability of three cameras arranged to cover different perspectives allows the quantification of bubbly flow parameters with respect to the $x-y$ and $x-z$ planes, while at the same time providing wall-normal ($x-y$ plane) close to the wall liquid velocity measurements.

- The spatial multi-scale visualization configuration allows for liquid turbulence measurements to be resolved for both, the largest and smallest scales within the test section.

- The spatial multi-scale visualization allowed to resolve detailed near-wall liquid velocity measurements, and three different scales to study the bubbles dynamics during the life time of the bubbles.

- The "Continuous" and "Straddling" timing modes allowed for the temporal multi-scale measurements on which are resolved thefast-happening instantaneous parameters while providing also a venue for resolving the long-term average measurements. This capability proved to be specially important for the average and instantaneous bubbles dynamics measurements.

Infrared thermometry.

- Infrared thermometry allowed for measurements of two-dimensional temperature fields of the heater wall. Only average temperature fields were considered. The infrared measurements were specially useful to ensure experimental repeatability. Slight deviations from the "normal" boiling behavior were easily capture as outliers in the measured temperature fields.

Analysis of a Single Nucleation Site.

- By placing the measurement area on the vicinity of a single nucleation site, it was possible to measure the flow development from a single-phase heated condition on its transition to a two-phase bubbly flow condition, i.e., measurements were available for both upstream and downstream of the nucleation site covering the full bubbles life-cycle.

Improved experimental practices.

- An experimental protocol was developed to reduce the influence of non-condensable gases, laser induced heat, optical distortions due to temperature gradients, and heater aging. This protocol helped to achieve a reasonable repeatability and reduced uncertainty.

5. EXPERIMENTS

5.1 PTV-IR-Shadowgraphy Experiments

The PTV/Shadowgraphy camera measurement area was located at about 12.3 cm from the test section inlet. Simultaneous PTV and shadowgraphy measurements were performed at this position. The high-speed camera was set to 4000 frames/s, with an exposure time of 250 μs. The relatively large exposure rate was selected as to allow enough light to reach the camera sensor and achieve satisfactory shadowgraphs of the bubbles. The time between the PTV and the shadowgraphy pairs was Δt_{PTV}=1/2000 s. This timing allows to acquire one frame of PTV immediately followed by one frame of shadowgraphy. For the medium magnification experiments, each acquired image consisted of 640×952 pixels and a resolution of 17.5 μm. Only one experimental condition was considered, with a Reynolds number of Re = 4400. For this Reynolds number, a heat flux of $q'' = 13.5$ kW/m^2 was selected and a constant inlet temperature of about 15°C was maintained. This experimental condition allowed for a stable nucleation site behavior, however, as can be seen later, nucleation intermittency was found to be a natural behavior at this conditions. The heater wall temperature was measured with the infrared camera. The infrared camera magnification allowed temperature measurements of the whole length of the test section with a resolution of 265 μm. Inlet and outlet fluid temperatures were also measured by means of T-type hypodermic thermocouples.

6. UNCERTAINTY ANALYSIS

As discussed previously, there exist a vast collection of works which focus on subcooled boiling. However, there are not many subcooled boiling experimental studies utilizing visualization techniques to study simultaneously the behavior of both phases and their influence on the heater wall temperature. The reason of the scarcity of visualization studies dealing with subcooled boiling studies may be due to the experimental inherent complexity and the relative incompatibility between these visualization measurement techniques and the boiling phenomena of interest. For example, if not properly addressed, the visualization instrumentation may induce perturbations into an otherwise statistically stable boiling system. In this section are summarized the sensitivity analysis of experimental issues not previously addressed in other studies. These issues are classified in three categories a) visualization experimental issues, b) error sources due to the boiling phenomena, and c) data analysis issues. The methodology to quantify and minimize the experimental uncertainties are presented in the next sections.

6.1 Visualization Experimental Issues

Most of the visualization experimental techniquesshare the characteristics of utilizing specialized illumination sources. These illumination sources will depend on the targeted parameters of interest. The 2D PTV technique utilizes a high energy 2D laser light sheet for liquid velocity measurements, while the shadowgraphy technique utilizes volumetric illumination, such as an halogen or LED lamp, to generate shadows of the objects under investigation. These illumination sources produce large amounts of heat, and since in this study, the PTV and the shadowgraphy techniques were

utilized simultaneously, the impact of the illumination instrumentation induced heat on the boiling system was addressed and quantified. It is important to mention that similar studies were performed before (Estrada-Perez and Hassan, 2010), however, previous studies limited their analysis to understand the impact of illumination heat sources on the wall temperature by means of wall-thermocouples. In the present study the multi-view, multi-scale visualization and the added advantage of a high-speed infrared camera allowed to capture the effect of the illumination heat sources in both, the bubbles dynamics and the heater wall temperature. The present sensitivity studies are summarized in the next sections.

6.2 Selected Timing Modes (Straddling vs Continuous)

The illumination system was configured to run in continuous and straddling modes (see chapter 4) with two illumination sources; a high energy laser and an LED lamp. A sensitivity analysis was performed to quantify the influence of these illumination sources and to explore ways to minimize non-desirable effects. Four tests were considered: a) LED illumination and continuous timing mode, b) LED illumination and straddling timing mode, c) LED+laser illumination and Continuous timing mode, and d) LED+laser illumination and Straddling timing mode. The effect of the illumination timing modes was studied from the measurement results of bubbles dynamics and from the Infrared heater wall temperature measurements.

6.3 Effect on Bubbles Dynamics

For this analysis, we focused on the bubbles dynamics behavior. Figure 6.1 shows the comparison of the near-nucleation site bubble dynamics between the different illumination and timing modes. Fig. 6.1 shows a two dimensional plot of the bubbles

centroid location for each case (X is the axial direction, while Y is the wall-normal direction). For these conditions the bubbles rarely detached from the wall, therefore the bubbles centroid location gives a very good indication of the bubble radius. It is noticeable that for almost all cases the bubbles paths followed a similar trajectory. However, the Laser+LED Continuous case showed to be different from the other test cases. The added amount of heat by the laser running in Continuous timing mode, produced bubbles even upstream the nucleation site under investigation. These laser-induce bubbles, while sliding through the wall, travel on top of the nucleation site causing it to deactivate or making it intermittent. Of special interest are the comparisons between LED Straddling and Laser+LED Straddling cases, in both cases the bubbles paths seem virtually the same. This gives a clear indication that the laser induced effects are minimal when the Straddling timing mode is used. It is important to note that although the LED Continuous case presents very similar bubble behaviors, the bubbles most probable paths are not captured. This may be due because in the Continuous timing mode, fewer independent samples are acquired hindering the overall statistics of the measurements, i.e., a single bubble is captured in multiple frames, therefore reducing the sampling number. With the Continuous timing mode, outliers bubbles may impact more the statistics. Fig. 6.2 compares the estimated bubbles diameters measured in each of the experimental modes. From the box plots is noticeable that even when the average bubble diameter is about the same (0.52 mm) much more outliers are found in the Laser+LED Continuous mode. From these plots can be concluded that if the straddling timing mode is selected it can be ensured similar behavior in repeated experiments. The shadow illumination continuous mode provides similar characteristics but with a higher number of outliers.

From this analysis it was concluded that as long as the straddling timing mode is used, non-desirable influences from the illumination sources are considered to be

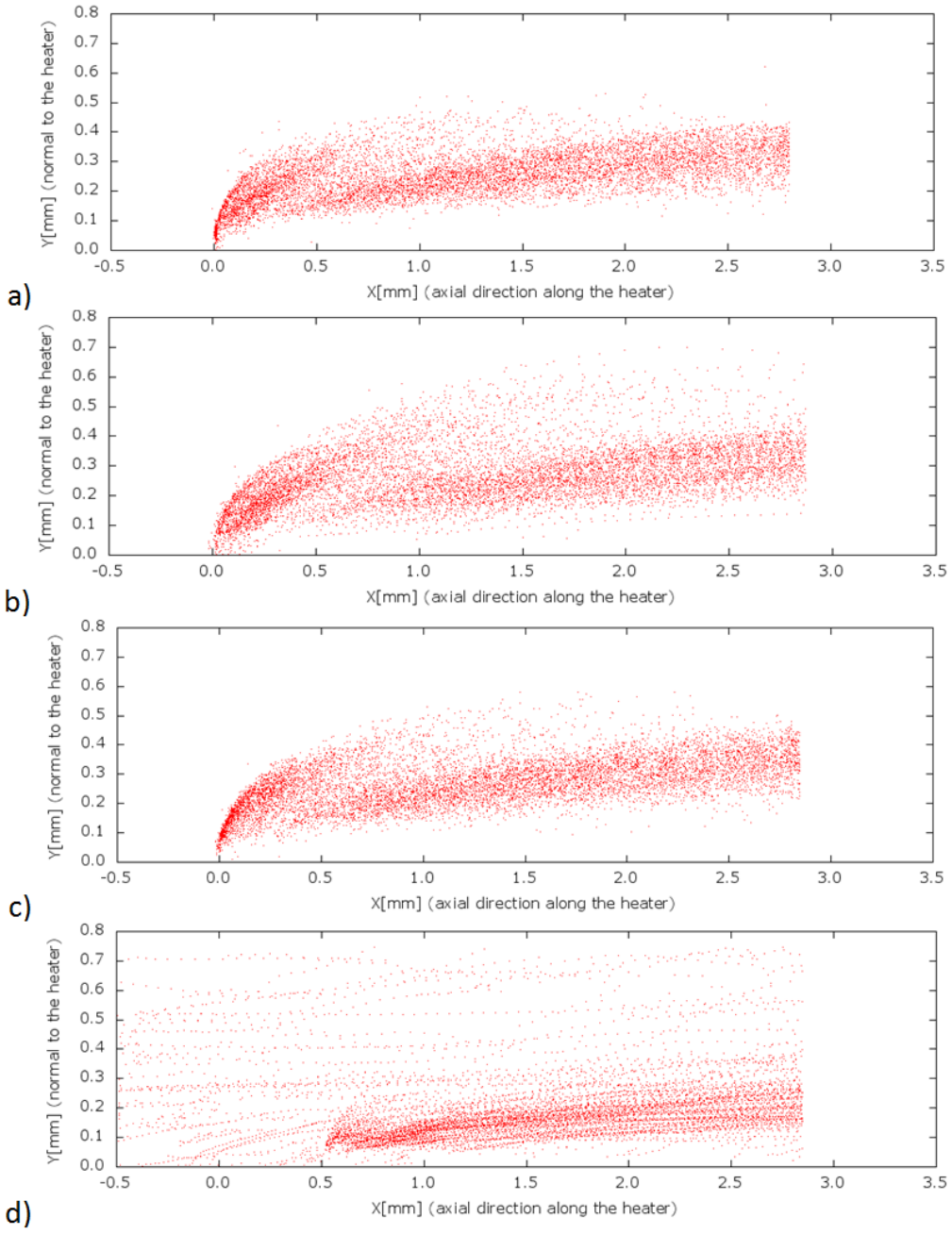

Figure 6.1: Bubble dynamics behavior at different illumination and timing conditions: a) LED straddling, b) LED Continuous, c) Laser+LED straddling, and d) Laser+LED continuous.

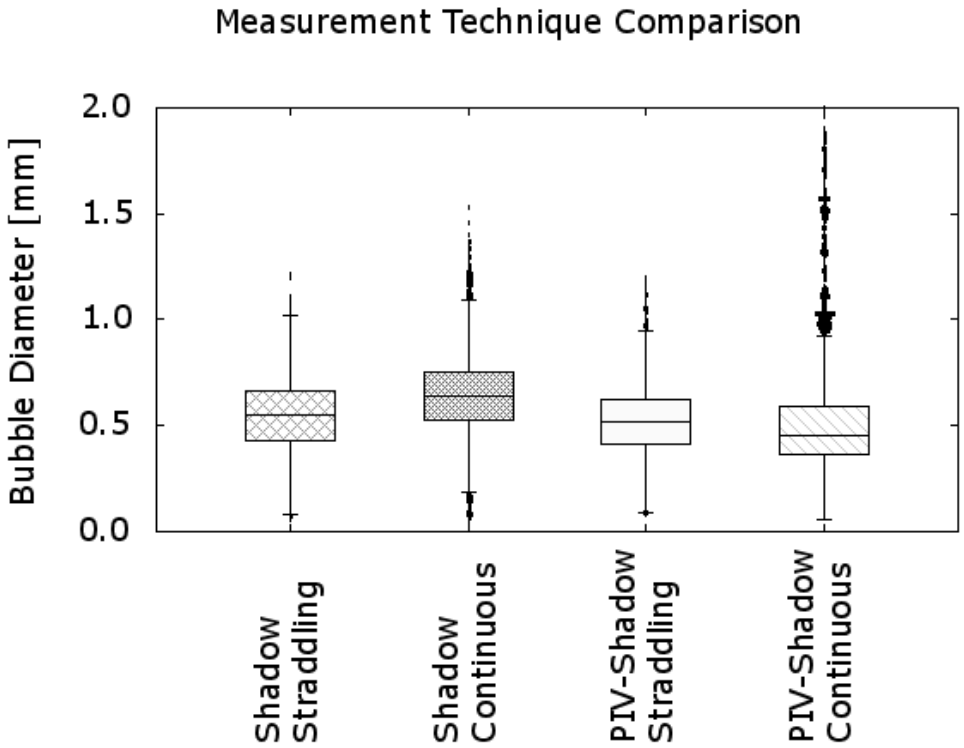

Figure 6.2: Bubbles diameters comparison between different illumination and timing modes.

negligible small.

6.4 Effect on the Heater Wall Temperature

As mentioned previously, the effects of the illumination sources and timing modes have a significant effect on the bubbles dynamics. In a similar way, illumination sources also affect the heater wall temperature, and when considering that boiling bubbles dynamics are intimately linked to heater wall heat transfer, these effects become more evident. Two mechanisms were found on which illumination sources may change the heater wall temperatures, the first mechanism is the direct energy deposition from the illumination sources to the heater wall. The direct energy deposition may be absorbed uniformly by the whole heater, as in the case of halogen and LED lamps for shadowgraphy measurements, or it may be absorbed only in particular locations, such as in the case of PTV, on which the laser light sheet was restricted to a line of 0.8 mm thickness impinging on the heater wall. From infrared measurements, the direct deposition of energy from illumination sources appeared to be negligibly small, and was barely detected when single phase experiments were performed. The second mechanism were noticeable only in the boiling experiments, and significantly changed the heater wall temperature. The wall temperature distorting mechanism is indirect in nature and initiate due to small perturbations of the heater wall temperature. The small temperature perturbations lead to modification of the bubbles dynamics in the form of illumination induced boiling. The illumination induced boiling brought about significant changes in the heater wall temperature, as can be seen in Fig. 6.3. Fig. 6.3 shows the results of a sensitivity study on which four cases were considered: a) No illumination, b) LED illumination and Straddling timing mode, c) LED+laser illumination and Straddling timing mode and

d) LED+laser illumination and Continuous timing mode. From these results is clear that the LED+laser illumination with continuous timing mode produced significant changes when comparing to the no illumination case. The temperature changes were not so significant in the single-phase region, there seems to be a constant temperature increase up until the vicinity of the nucleation site (about 130 mm from the inlet electrode). The laser induce bubbles acted as a heat sink in the nucleation site region, making it intermittent. The nucleation site intermittency reduced the heat removal due to a reduced bubble frequency, which is translated in a temperature increase downstream of the nucleation site as seen in Fig. 6.3. All other illumination cases on which the laser light illumination in a continuous timing mode were not used, provided reasonable and repeatable results.

6.5 Thermally Induced Optical Distortions

Thermally induced optical distortions (TOD) in subcooled boiling systems are typically found nearby interfaces on which large temperature gradients occur. Of special interest on subcooled boiling are the heater wall-liquid interface and the boiling bubbles-liquid interfaces. The TOD phenomenon is specially relevant on organic fluids on which the refractive index is strongly dependent on the local fluid temperature (Elsinga et al., 2005), as is the case for the present study. The working fluid selected for the current experiments is relatively new, and the temperature dependance of the refractive index is unknown. Therefore an experimental characterization was performed to test the influence of refractive index changes on the optical "performance" of the visualization techniques. From the analysis, it was found that the thermally induced optical distortions have three main effects, one bias effect, and two random effects: one due to density changes and the other due to optical distortions produced

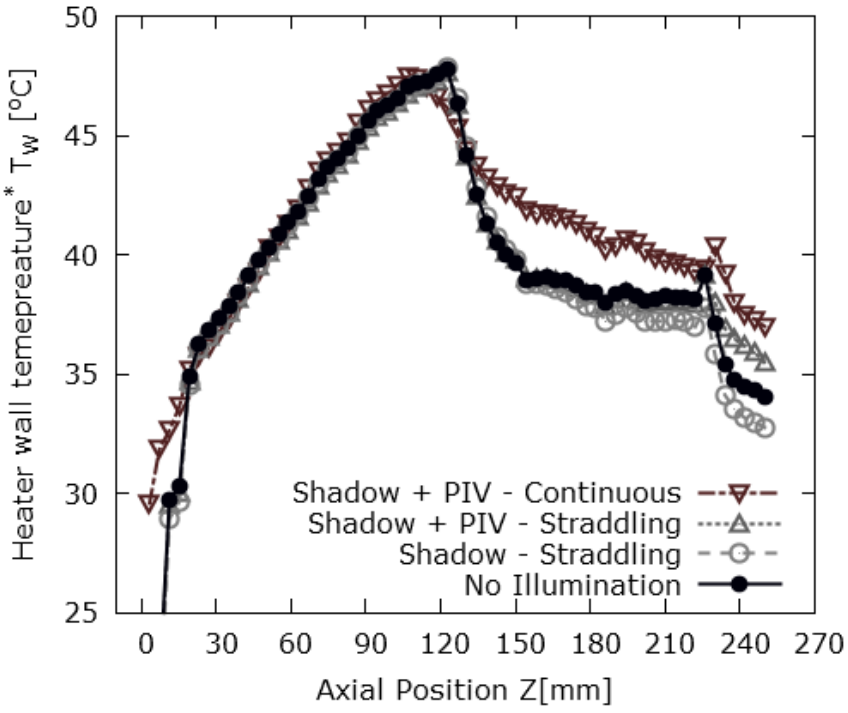

Figure 6.3: Wall temperature influence due to different illumination and timing conditions.

by the boiling bubbles. These effects can be accounted to be included as part of the bias (β_{TOD}) and random uncertainty (σ_{TOD}) of the PTV centroid location algorithm. The quantification of these effects were performed in situ, with the following process: A calibration grid with circular patterns was located as to coincide with the focal plane of the PTV/Shadowgraphy camera. The flow loop was ran normally at the conditions of interest, namely at a Reynolds number of $Re = 4400$, a heat flux range from 0 to 13.5 kW/m^2 and a subcooling level of ΔT_{sub} =15.0°C. The PIV/Shadowgraphy camera frame rate was set to 2000 fps, the same frame rate as the one used for the "continuous" timing condition (see section 4.1.2). The experimental conditions of the uncertainty analysis emulate exactly the boiling experimental conditions, with the exception of the camera focal plane location. In this analysis, the camera was focused on the calibration grid, rather than on the nucleation site. The calibration grid was located on the outer face of the channel, at about 6.5 mm from the nucleation site (the nucleation site was located at about 3.5 mm from the inner wall). This location was selected as to maximize the illumination light path length through the medium with variable refractive index (the heated refrigerant) on its travel from the target (the calibration grid) to the camera sensor.

Shadowgraphy pictures of the calibration grid were acquired at five different heat fluxes. 1000 images were stored per condition. The acquired calibration grid images were pre-processed to match the requirements of the PTV centroid location algorithm, which receives as input an image with white objects embedded in a black background. The PTV centroid location algorithm was applied for all images within each set. Fig. 6.4 shows the centroid location process applied to the calibration grid. Fig. 6.4 (a) shows an example of the original shadowgraphy image of the calibration grid. Fig. 6.4 (b) shows the inverted version of the original calibration grid image which is the input of the PTV centroid algorithm, and Fig. 6.4 (c) shows the output of the PTV

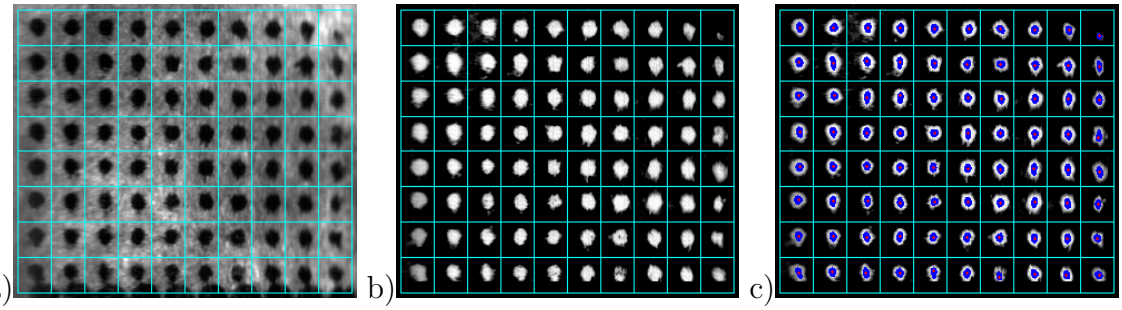

Figure 6.4: Centroid location process.

centroid location algorithm. The PTV centroid location algorithm is based on a particle mask correlation method (Takehara and Etoh, 1999), on which every pixel is correlated to an "ideal" object image, in this case, a white circle embedded in a black background. The blue pixels in the output image indicate pixels near the vicinity of the centroid, while the red pixels indicate the centroid position itself.

6.5.1 Random Uncertainty due to Thermally Induced Optical Distortions (σ_{TOD})

As mentioned previously, the random component of the thermally induced optical distortion can be divided in two, those due to density fluctuations without phase change (σ_{TOD_ρ}) and those due to the bubbles passing through the measurement region (σ_{TOD_b}), therefore, the total TOD random uncertainty can be expressed as $\sigma_{TOD} = \sigma_{TOD_\rho} + \sigma_{TOD_b}$. These random components of the thermally induced optical distortions were estimated from the calibration grid images. The random distortions without phase change (σ_{TOD_ρ}) showed a concomitant behavior with the heat flux. As expected, these distortions showed to be larger for the higher heat flux cases, and for the regions within the vicinity of the heated wall. The effect of the random distortions on the calibration grid images appeared as image deforming patches which moved in the flow direction. These patches varied in length and width affecting differently the appearance of the grid images. Ultimately, the grid points location estimation

was randomly changed by these patches. To clarify this effect Fig. 6.5 shows the centroid location estimation of the calibration grid points. These results are shown for the non-heated and boiling conditions ($q'' = 0$ and q'' =13.5 kW/m^2 respectively). It is important to mention that the boiling bubbles are outside of the camera focal plane, reducing in this way their optical distortion influence, therefore it is safe to say that the present analysis quantifies only the uncertainty due to the effect of the liquid density changes. Fig. 6.5 shows the calibration grid points centroid location estimation for all 1000 images for both, the unheated and boiling conditions. It is clear that the centroid location fluctuations are larger for the boiling condition, which is represented by the black crosses, while the red crosses represent the centroid location estimation on the unheated condition. It is important to mention that although no variations on the grid points centroid locations were expected for the unheated case, small variations were found of about 0.1 pixels. These variations are mostly attributed to the LED illumination fluctuations and due the fact that the PTV algorithm will produce larger uncertainties for centroid estimation of big objects (Estrada-Perez and Hassan, 2010). Therefore we define here a random error inherent to the PTV algorithm for big objects as $\sigma_{PTV} = 0.1$ pixels.

Further conclusions may be drawn from the wall-normal RMS profiles of the centroid location estimation. These profiles are shown in Fig. 6.6. The centroid location RMS of the boiling case is a function of the wall-normal position, while the single non-heated case shows to be position independent. The boiling case showed to have a maximum RMS of about 0.6 pixels on the near-wall region, decreasing asymptotically for regions far from the heated wall towards a value of about 0.15 pixels. Noting that the boiling asymptotic RMS value is slightly different to 0.1 (which is representative of the single phase case), lead us to conclude that the influence of the thermally induced optical distortions affect the whole measurement view and

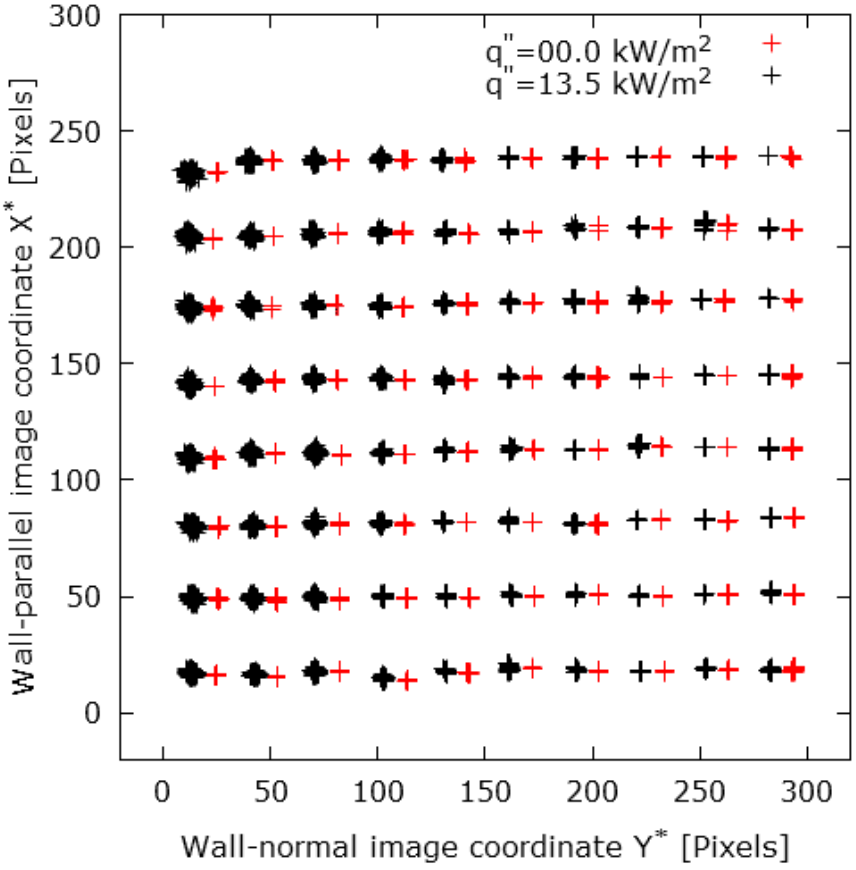

Figure 6.5: Estimated location of grid points.

need to be accounted for. Another conclusion from this analysis was the fact that the centroid location random uncertainties due to thermally induced optical distortions has an equal effect on both, the wall-normal and the wall-parallel directions.

From Fig. 6.6 we can obtain a maximum value for $\sigma_{TOD_\rho} \approx 0.5$ pixels (considering that about 0.1 pixels is attributed to the algorithm uncertainty at this conditions). However, considering that this value is only valid at the location of the calibration grid, a correction is required for positions nearby the nucleation site. Assuming a linear dependency with the distance, and considering that the nucleation site region is one third from the calibration grid region, the uncertainty in the region of interest is considered to be also one third. Therefore, $\sigma_{TOD_\rho} = 0.16$ pixels. This assumption will be validated in a later section.

6.5.2 Bias Uncertainty due to Thermally Induced Optical Distortions (β_{TOD})

An apparent displacement of the calibration grid points was observed as a consequence of heat flux increments. This displacement was uniformly distributed through the whole image with a wall-normal preferential direction. The overall trend was that for every increment on heat flux, the whole image seemed to shift towards the direction where the heated wall was located. This effect was so unexpected and large, that it was wrongly thought that the camera or the channel were displaced in some way. The apparent displacement can be observed, when comparing the grid points centroid estimation of the boiling and unheated conditions from Fig. 6.5. To clarify this effect, Fig. 6.7 shows a single row of grid points for the five different heat fluxes considered for this analysis. This apparent displacement is stable once a steady state condition is reached, after which an estimation of β_{TOD} can be easily obtained and a correction for each heat flux is readily available.

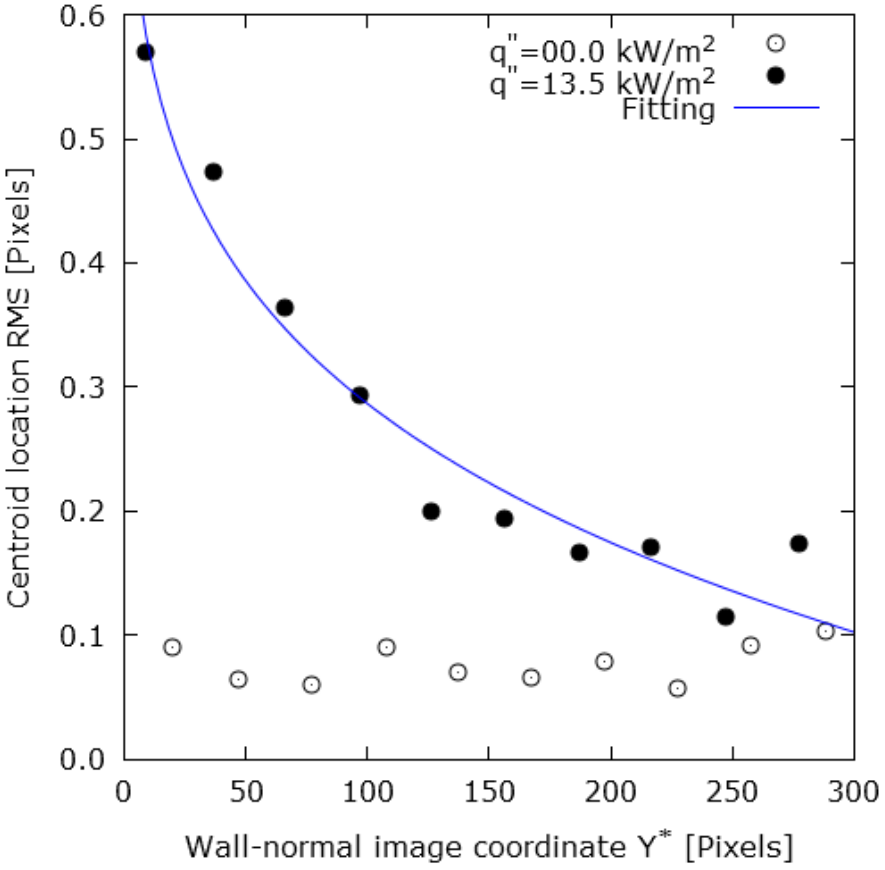

Figure 6.6: Location uncertainty due to refractive index fluctuations.

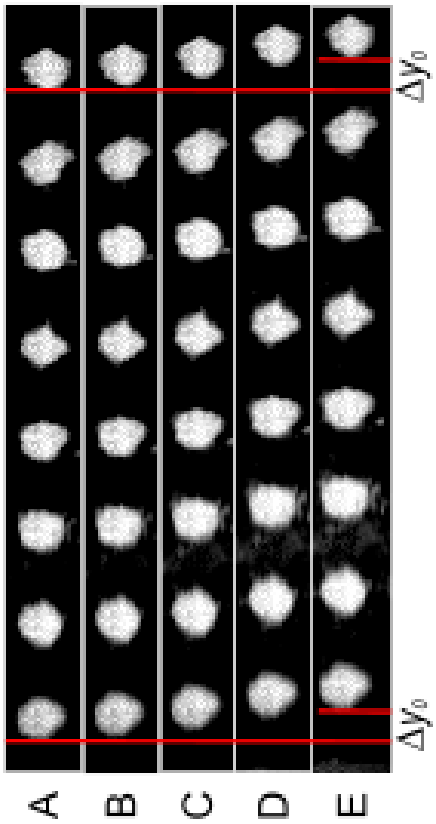

Figure 6.7: Apparent position displacement due to temperature driven refractive index changes.

6.5.3 Random Uncertainty due to the Bubbles Passing Through the Measurement Region (σ_{TOD_b})

From all the thermally induced optical distorting effects, the one that brought about the largest uncertainties was the boiling bubbles effects. To quantify the effect of the boiling bubbles, a calibration grid was located exactly on top of the nucleation site. The camera focal plane was located in the calibration grid position so as to have the calibration grid on focus. From the camera perspective, the boiling bubbles passed in front and behind of the calibration grid. Only the bubbles passing in front of the calibration grid produced optical distortions. To clarify this procedure, Fig. 6.8(a) shows the optical distortions that a seemingly transparent boiling bubble produce on its path in front of four calibration grid points. The boiling bubble is sliding along the heater moving up in the direction of the flow. The frames at times $t = 0.0$ and $t = 4.0$ ms shows examples when the influence of the bubble was minimal. It is clear that at those particular times the centroid estimation of the four points were accurately captured. However at different times, the bubbles domain was nearby of the measured area, and the bubbles influence was clear. The curvature of the bubbles interface produce a lens-like effect which produced the optical aberrations of the calibration grid points.

A more quantitative approach may be observed on Fig. 6.9, where the black dots represent the centroid location estimation from a row of the calibration grid. The bubbles influence is confined to near-wall regions, on which the boiling bubbles are located. The bubbles induced uncertainties showed a similar behavior as the liquid density fluctuation uncertainties in the sense that it was not observed any preferential direction either. The centroid location of grid points varied within a range of 15 pixels which in the context of PIV/PTV is unacceptable. Therefore an

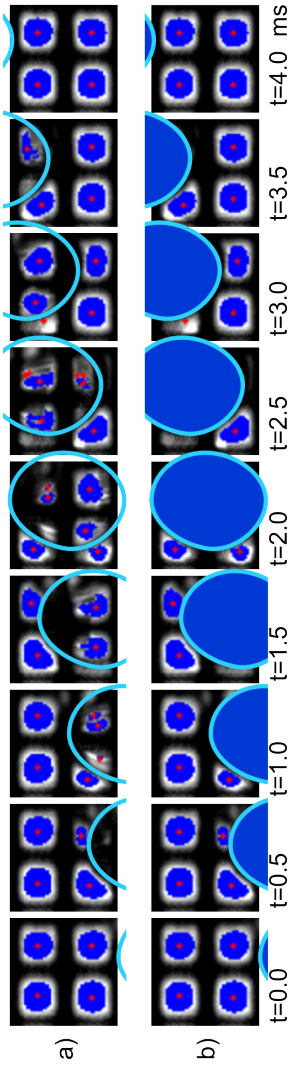

Figure 6.8: Example of centroid location variation due to a bubble optical distortion.

approach to reduce this influence is strongly suggested. In this work we removed all the bubbles induced optical distortions by using the bubbles images as masks to remove this undesired effect. The process of bubbles masking was facilitated due to the fact that we performed simultaneous PIV and Shadowgraphy visualizations, this meant that we can use the bubbles information from the shadowgraphs to remove the unreliable particles found within the domain of the bubbles. Fig. 6.8(b) shows the bubbles masking procedure to reduce the effect of the bubbles passing. In this case the bubbles body is considered to be no longer transparent, therefore the lensing-effect is totally removed. However, bubbles influence still prevails in the vicinity of the bubbles. In these regions, large density changes are still producing considerably large effect. However it has to be recalled that in the PIV/PTV experiment, the objects to be tracked are tinny particles that are following the liquid flow. Both of these characteristics (small size and moving with the flow) will reduce greatly the bubbles influence. The present analysis is quite conservative, and it is expected that both, the density fluctuations and bubbles influences will affect the PIV/PTV particle tracers centroid location in a reduced fashion. The process of removing the information within the domain of the bubbles is shown in Fig. 6.9. The red dots represent the resulting centroid location estimation after removing the undesired bubbles induced information. By simple comparison, it is clear that the bubbles removal process drastically reduced the centroid location range from about 15 pixels to about only 2 pixels.

Fig. 6.10 shows the centroid location RMS comparisons between three cases, the unheated case, the boiling case with raw data, and the boiling case without the bubbles unreliable information. The bubbles brought about a huge RMS on the order of 2.5 pixels which was reduced to about 0.4 pixels just after removing the bubbles information. From the comparison of these two cases, it is clear that the bubbles

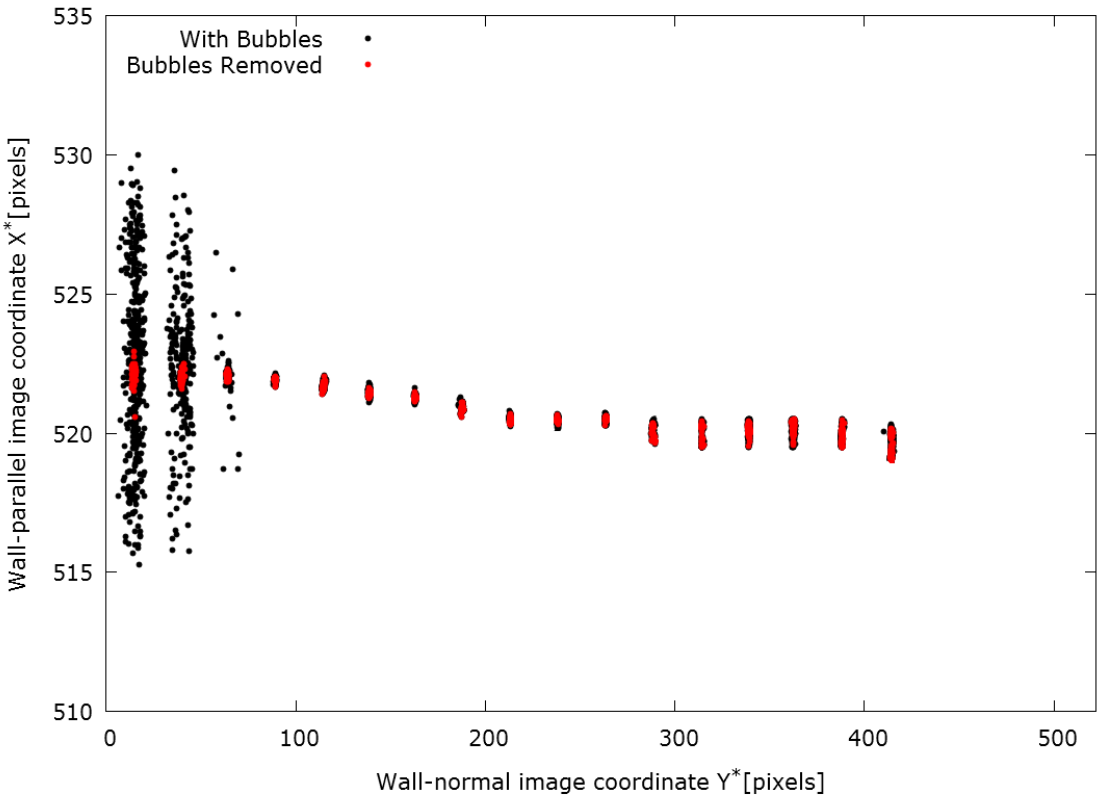

Figure 6.9: Centroid location variation due to bubbles induced distortions.

removal correction extends to the first four points (from left to right) of the profile. These points are closer to the heated wall. The fifth and sixth points show a significant discrepancy compared to the unheated case. This discrepancy may be explained by the density fluctuations effects or by the distorting effect located on the vicinity of the bubbles interface. From this information the maximum bubbles induced optical distortion for the near-wall measurements accounts for about σ_{TOD_b} =0.2 pixels. This value does not take into account the density fluctuation influence which accounts for about 0.2 pixels, a similar value was obtained for the density fluctuations induced uncertainty estimated in previous sections, which accounted for $\sigma_{TOD_\rho} = 0.16$ pixels, therefore the assumption of a linear dependency of the density induced uncertainty with respect to location seems to be reasonable.

6.6 Data Analysis Issues

6.6.1 PTV Related

The previous sections showed critical issues that have to be addressed when using PTV for the analysis of subcooled boiling experimental images. These issues were mainly related to optical distortions due to density gradients and due to the existence of boiling bubbles in the measurement region. Based on this information, it was decided that careful removal of bubbles induced vectors was a necessity to ensure reliable liquid velocity measurements. The bubbles induced vectors removal can be performed in two distinct ways: The first one, which will be called Bubble Image Masking (BIM), is an image processing algorithm that removes or masks the pixels that are within the domain of the bubbles. The second one, which will be called Bubbles Velocity Masking (BVM), is a post-processing algorithm that removes or masks the velocity vectors that are within the domain of the bubbles. In both

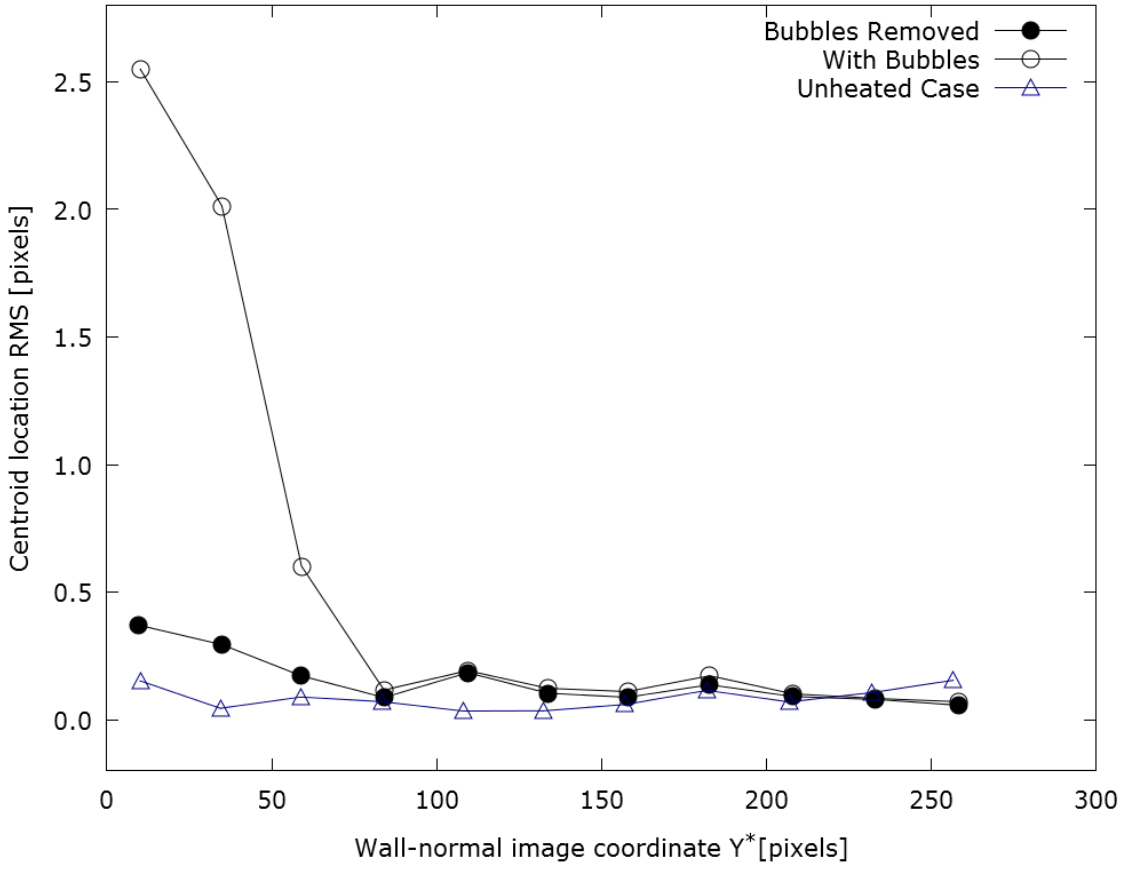

Figure 6.10: Centroid location estimation RMS variation due to bubbles induced distortions.

cases, the bubble domain is determined from the shadowgraphy images acquired simultaneously with the PTV images. Fig. 6.11 shows the comparison of the average liquid velocity profiles using three different PTV analysis procedures, including the Raw data analysis, on which no bubble information was removed, the PTV analysis on which BIM was used to remove undesired noise from bubbles images, and the PTV analysis with BVM, to remove undesired velocity vectors within the bubbles domain. These results are compared at different axial positions (x = 0.0 mm, 1.2 mm, and 6.2 mm) from the nucleation site. From these results, it is clear that the PTV analysis with BIM produces an overestimation of the liquid velocity at the axial location x = 6.2 mm. Investigation of these results showed that the bubbles image removal of the BIM process hindered the particle centroid location of the PTV algorithm, resulting on spurious particles on the vicinity of masked regions. The spurious particles location corresponded to the bubbles interfaces, which lead to erroneously measure the bubbles velocities. This explains the overestimation of the liquid velocity at the location x = 6.2 mm, at this location the bubbles are fully developed and have larger velocities. Based on these results, it was determined that the BVM performed better, not only the spurious particles detection was reduced with the BVM process, but also provided higher quality vectors due to the aid of the bubbles information on the particle matching process.

6.6.2 Bubble Intermittency

Although it appeared that at this experimental condition a stable bubble nucleation behavior was achieved, the influence of the additional power supplied by the laser showed to be large. When performing PIV experiments in a continuous mode (see timing configuration explanation), the nucleation site behavior changed drastically (these effect were explained in previous sections). Therefore it was decided to perform

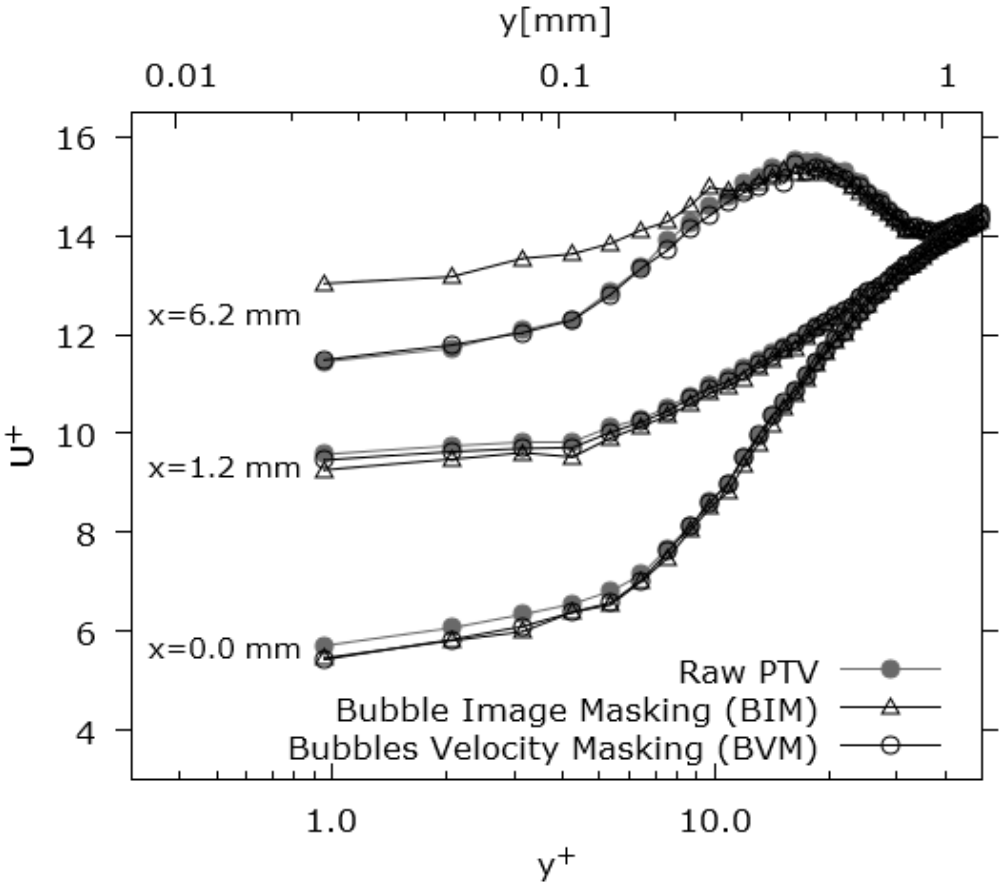

Figure 6.11: Bubbles images effect on the average liquid velocity measurements.

the PIV experiments only in straddling mode configuration. In straddling mode, the laser induced power was largely reduced, and the effect of the laser in the nucleation behavior was not longer noticeable. However, some intermittency was observed in the activity of the nucleation site. As shown in Fig. 6.12, this intermittency was detected directly from the experimental images. Ten percent of the 10,000 PIV images were considered as "intermittent" instances on which a lower void fraction was found. Examples of what was considered an "intermittent" image are shown in Fig. 6.12 (A), (B), and (C). Intermittent images were removed from the analysis of flow statistics because they were not representative of the "stable" behavior of the nucleation site. Fig. 6.12 (D) and (E) are examples of the experimental data that was considered in the statistical analysis. As of today, is not known with certainty the reasons of this intermittency.

Further insights are obtained when comparing the liquid velocity measurements between the stable case and the intermittent instances. Fig. 6.13 shows the average velocity profiles at three axial positions (x=6.2, x=1.19, x=0.0) from the nucleation site. The black filled symbols represent the stable case or in the context of this condition, it represents instances of high void fraction on which the bubble number was larger than six, the red hollow circles represent the intermittent cases on which low void fraction was found. Low void fraction cases were those on which less than 6 bubbles were present. Comparing the results obtained between the intermittent and the stable cases, the influence of the bubbles parameters is clear. For the intermittent cases, the small void presence barely influence the liquid velocity, in fact the deviation from a single phase behavior was small. However for the stable case on which the bubble layer was fully developed, the influence of the high void fraction brought about a large acceleration of the liquid velocity.

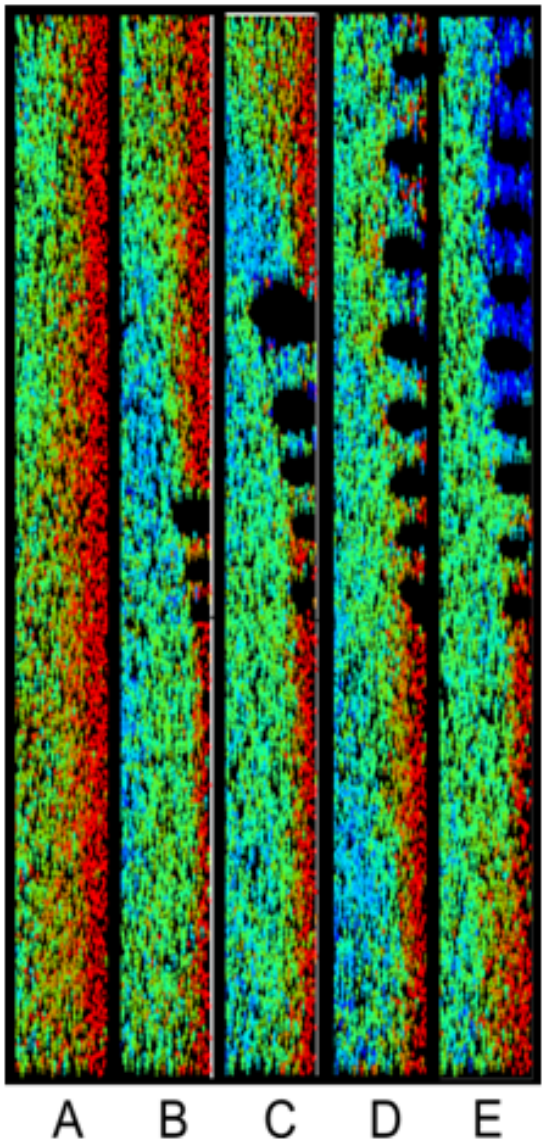

Figure 6.12: Intermittency of nucleation site activity.

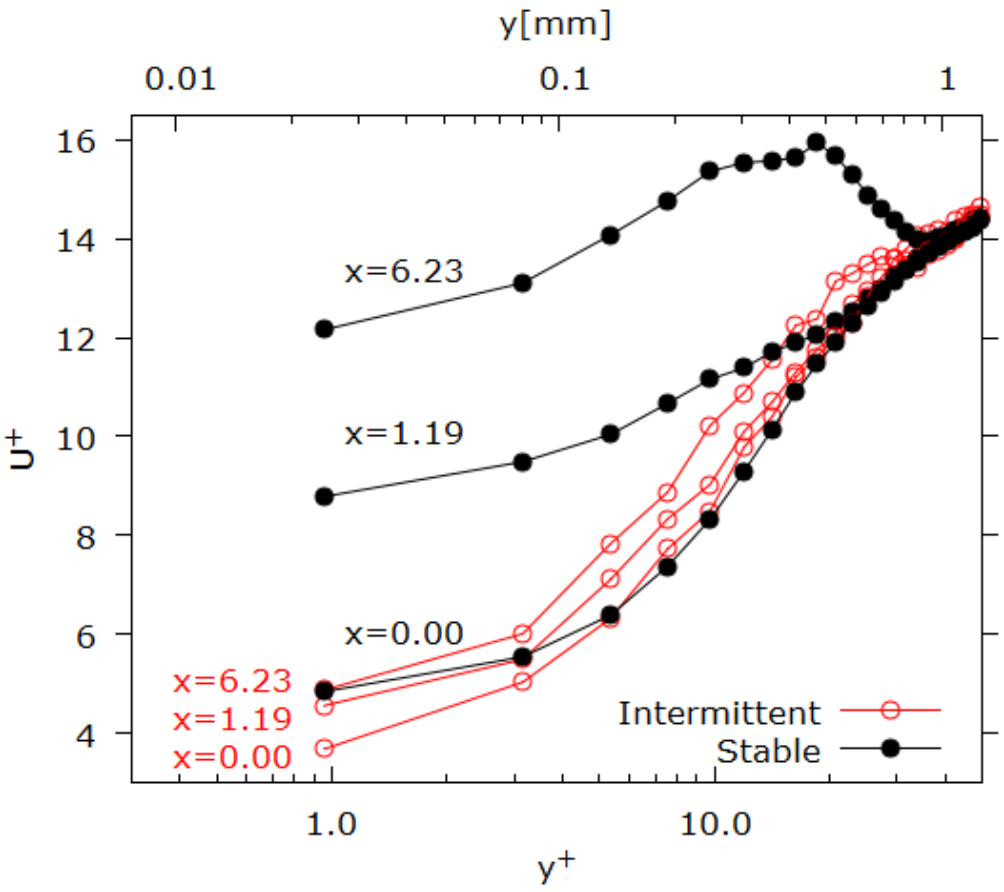

Figure 6.13: Velocity profiles showing the effect of the nucleation site intermittency.

6.6.3 Sampling Number Influence on Velocity Measurements

To ensure that the measured flow statistics have been computed with a high statistical significance, an analysis was performed to test the influence of sampling number on the statistical parameters of interest. In this case we were interested on the wall-normal velocity profiles along the heater, to this end, the velocity fields from the PIV images were divided in bins, 200 vertical bins in the wall-parallel direction, and 50 horizontal bins in the wall-normal direction. This allowed us to provide velocity profiles representing the flow development along the heater.

For the uncertainty analysis, we focused on a single horizontal bin and performed the average wall-normal velocity profile estimation depending on different sampling numbers. The selected sampling numbers ranged from 10 to 4000. This analysis was repeated five times, ensuring that each time different samples were selected out of the total sample pool which was about 4800 velocity fields. Fig. 6.14 shows the results of this procedure. For small sample numbers, or in this case for small number of vector fields, the discrepancies of the five estimated velocity profiles are significant. These discrepancies gradually die down by increasing the number of vector fields, until reaching a point on which increasing the number of vector fields no longer affects the estimated average profile. This point is said to have sufficient samples, enough to provide the velocity profile with high statistical significance. The point of high statistical significance for the wall-normal velocity profile corresponded to a value of about 3000 vector fields.

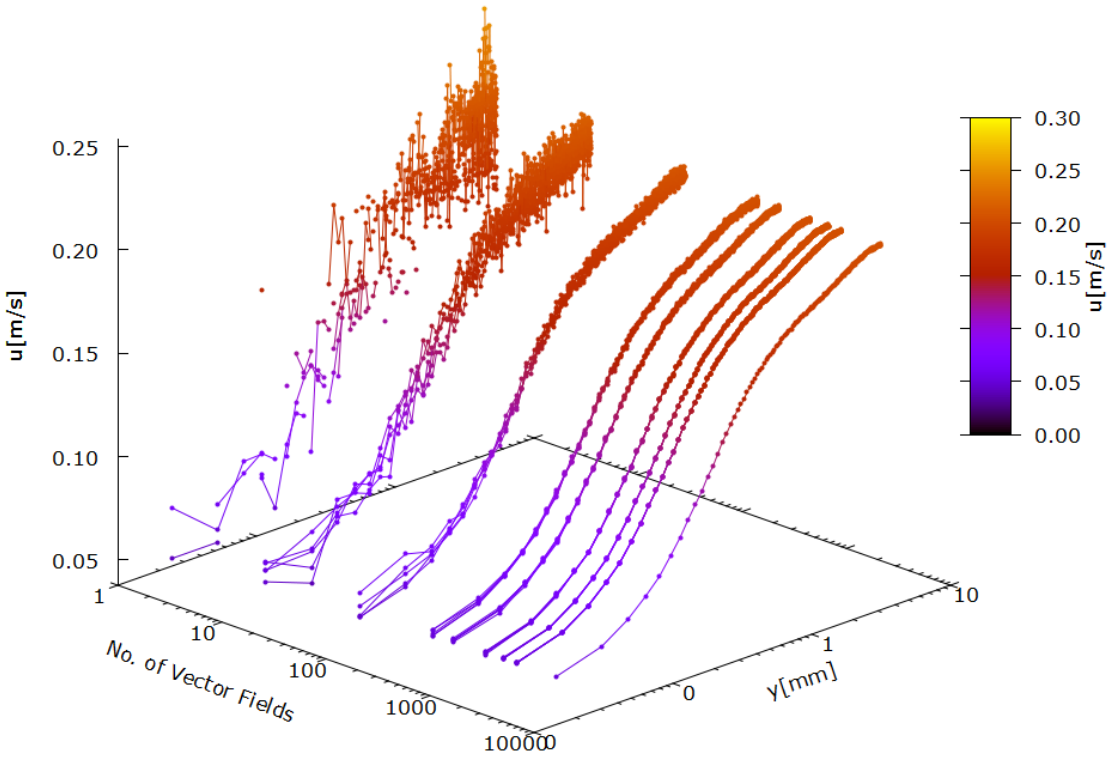

Figure 6.14: Sampling number effect on the velocity profile.

7. SUBCOOLED FLOW BOILING EXPERIMENTAL RESULTS

7.1 Velocity Measurements

After addressing the issues found in section 6 to reduce uncertainty and to enhance the statistics reliability, we focused on the liquid and bubbles velocity measuremetns. The velocity of both phases was obtained by means of particle tracking velocimetry (PTV). The PTV algorithm is able to track small objects such as the PIV particle tracers or large objects such as the boiling bubbles. The results of the tracking algorithm are shown in Fig. 7.1. The picture in the left of Fig. 7.1 shows an instantaneous velocity field on top of the shadowgraphy image, the right picture in Fig. 7.1 shows the PTV results of the boiling bubbles.

Fig. 7.1 shows the advantages of using the single nucleation site approach. This approach provides the capability of measuring at the same experimental condition, the flow development from a heated single phase to the transition to two-phase boiling flow. Furthermore, the bubbles dynamics can be accurately characterized at every point along the heater, this allows to explore the influence of multiple bubble dynamics conditions on the average liquid velocity behavior. From a set of instantaneous information, like the ones shown in Fig. 7.1, average flow statistical quantities can be estimated, for example, in Fig. 7.2 are shown the average void residence time fraction (left) and average liquid velocity profiles (right). The void residence time fraction was obtained from the average of a set of binary shadowgraphy images on which black pixels represented the liquid phase and white pixels represents the gas phase. This procedure enabled us to consider each pixel as a single void probe for the estimation of the local void fraction. Similarly from a set of instantaneous velocity fields, average velocity profiles can be obtained. Fig. 7.2 shows the liquid

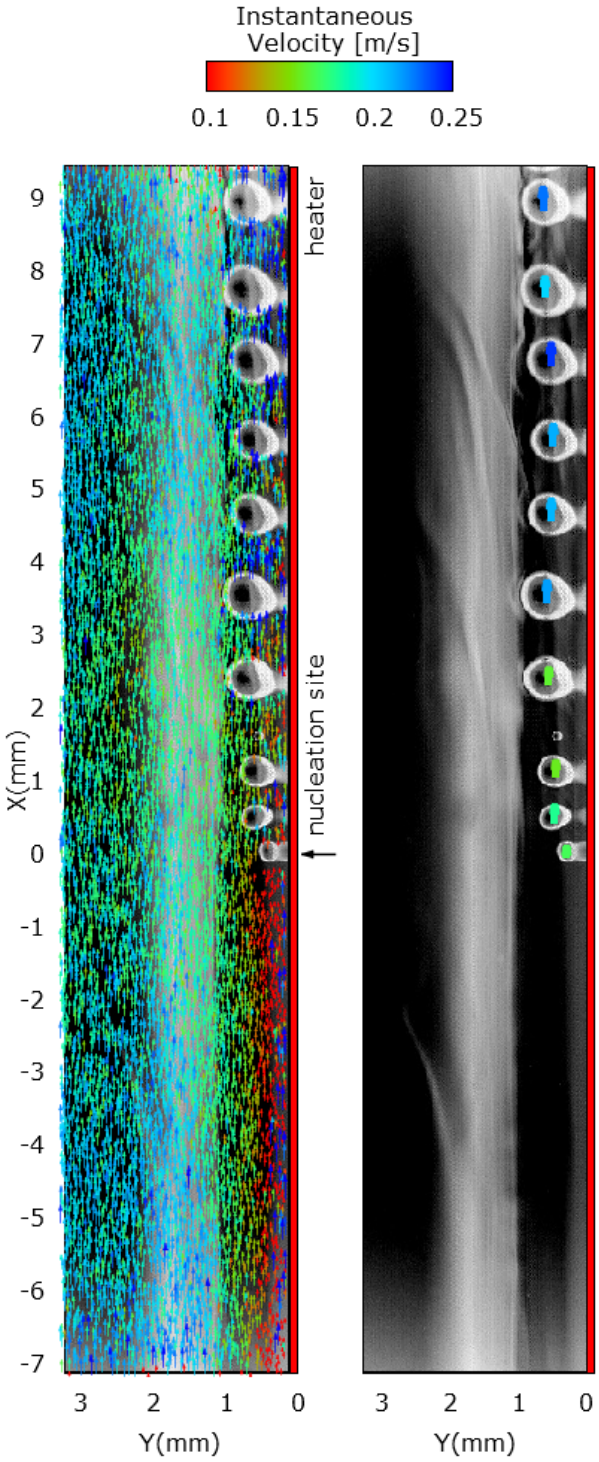

Figure 7.1: Liquid and bubbles velocity fields and profiles.

and bubbles average velocity profiles along the axial direction (right picture). it is clear that the effect of the nucleated bubbles brought significant changes on the liquid behavior: Upstream of the nucleation site, in the single-phase region, the liquid velocity is virtually not affected, the liquid statistics remain the same at different axial positions. Such behavior remain constant up until the region on which the nucleation site is located. Downstream the nucleation site, there is a liquid axial velocity increase which seems to be concomitant to the bubbles sizes and velocities. From the present observations it appears that the liquid velocity increase with the distance is maintained up until about a distance of 7 to 8 mm, after which, the local peak of liquid velocity tend to a terminal value of 0.2 m/s. A similar behavior was observed for the boiling sliding bubbles, bubbles diameters and velocities increased concomitantly with the distance. This increase on bubble diameter is attributed to the bubble sliding through the heated wall. It was also observed that the rate of bubble growth is much larger near the vicinity of the nucleation site, and that after few millimeters (~4 mm), the bubbles dimensions reached a value that was kept relatively constant. Bubbles velocity depended entirely on the bubbles sizes along the heater. The bubbles dynamics behavior is studied in more detailed in following sections.

7.2 Bubble Dynamics

Bubble dynamics were measured mainly from the high speed shadowgraphy experimental results. The measurements include, average bubbles paths or location, bubble diameters, instantaneous and average bubbles velocities, bubbles growth rate, and, fraction of bubbles residence time (or void fraction). The next sections presents these results together with a brief explanation of the procedure to obtain them.

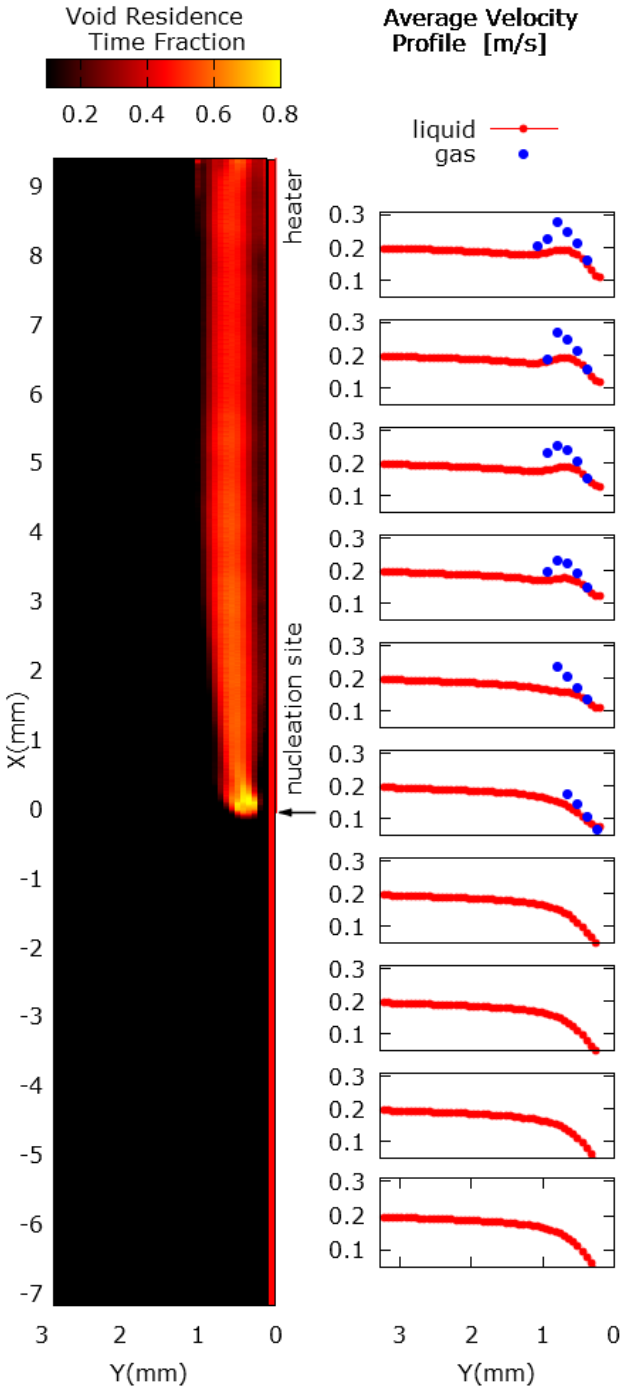

Figure 7.2: Void residence time and velocity profiles.

7.2.1 Experimental Images

The shadowgraphy images can be classified depending on the cameras configuration which was summarized in Section 4.1.2. The front view measurements were achieved with the shadowgraphy camera 2 and camera 3, which provided the largest measuring regions. Examples of the results from camera 2 and camera 3 are available from Fig. 7.3 and Fig. 7.4 respectively. Camera 2 provided the visualization of the whole length of the channel, with a viewing area of about 2.0×23.0 cm^2. Camera 2 was originally meant to provide nucleations site density measurements together with quantitative and qualitative information of the bubbles behavior downstream of the nucleation sites. However, due to the low camera resolution, results should be consider with caution. This camera arrangement will prove more useful when multiple nucleation sites are generated. It is noteworthy to mention that the horizontal line at the mid-section of the channel is the intersection between the two saphire windows positioned behind the heater as insulation. As can be seen in Fig. 7.4, camera 3 magnification provided a measurement area of about 13.0×27.0 mm^2. The higher resolution of this camera may allow for more accurate measurements of bubbles dynamics. However, due to the illumination configuration (see section 4.1.2), the bubbles images were far from ideal. Ideal bubble shadowgraphs should appear as black objects in a light background, or at least, bubbles edges should be easily discernible. The bubbles images from camera 3 did not showed good contrast and showed regions of transparency. This made difficult any type of analysis for quantitative information extraction. Camera 3 also captured the intersection of the two insulation saphire windows which is shown as an horizontal line in the upper part of the image. Bubbles passing through that line can not be properly characterized due to the low contrast between the bubbles body and the background.

Higher quality of shadowgraphy images were obtained from the side view camera (camera 1). This is due to the fact that the illumination arrangement allowed to have only one source of light for the shadowgraphy measurements. The source of light was the LED lamp. The LED lamp was arranged to directly illuminate the side view camera (camera 1) and only indirectly illuminate the front view cameras (cameras 2 and 3). An example of the side view low magnification experimental images is given in Fig. 7.5 which covers an area of about 10.0×16.0 mm^2. The bubble images from this view showed a larger contrast with the background, and bubbles edges were easily determined. This simplified the image processing to extract quantitative information from this images. Although the side view images showed to be of higher quality, there were many challenges from the image processing point of view. First, due to the use of telecentric lenses, dark regions were found on the images edges. These darker regions were neglected from the analysis. Second, due to the large temperature gradients in the boiling process, large density fluctuations hindered the quality of the bubbles shadowgraphs. Density changes were observed as randomly moving streams of dark and light pathces moving with the flow. Also, bubbles shown to have transparent bodies, specially in their central regions. This transparency affected little the extraction of quantitative information because the bubbles edges were still easily identified. The side-view low-magnification images shows detailed information of the bubble behavior downstream the nucleation site location. It is clear from Fig. 7.5 that bubbles start fairly spherical in shape and slide through the heated wall gaining size. Further away from the nucleation site the bubbles shape is no longer spherical but rather become pear shaped with a bubble necking in regions close to wall. There were not many bubbles detachment observed from the wall, rather, a continuous growing and sliding was found along the heater wall.

The highest magnification was provided by the side-view camera. it allows a measuring area of about 5.0 $\times$ 4.0 mm^2. An example of the side-view high magnification images is shown in Fig. 7.6. This configuration was designed to provide detailed information in the near-nucleation site region. The bubble life-time in the vicinity of the nucleation site is clearly captured with this camera configuration.

From these experimental images, relevant quantitative information was extracted. However, the front-view high-magnification results were not analyzed due to the difficulties encountered in the image pre-processing. Furthermore, the side view results provided the information relevant to the liquid-bubble interaction. Some of the bubbles dynamics obtained with the shadowgraphy images are shown next.

7.2.2 Bubble Probable Paths

Fig. 7.7 shows the high magnification shadowgraphy results (resolution of 4.82 μm). The high magnification results allowed a detailed examination of the average bubble behavior along the bubble path. Four profiles are shown in Fig. 7.7: bubbles width, height, axial velocity, and normal velocity. It is important to note that more than 20,000 bubbles were considered so as to show the most probables behavioral bubble paths along the heater wall. Furthermore, these results were obtained with the straddling timing mode, which provides an independent measuring sample for each image pair. As observed in Fig. 7.7, large changes in the bubbles dimensions came about the first half millimeter after nucleation. Bubbles at the nucleation site increased rapidly both in width and height. The nucleated bubbles showed to follow two preferable growing paths, namely: Path A and Path B. Path A is characterized by a sharp increase on bubble size, following two typical behavior. The first behavior of bubbles following path A is the rapid size increase of a single bubble, which in turn provided enough inertia normal to the wall so as to promote bubble detachment. Most

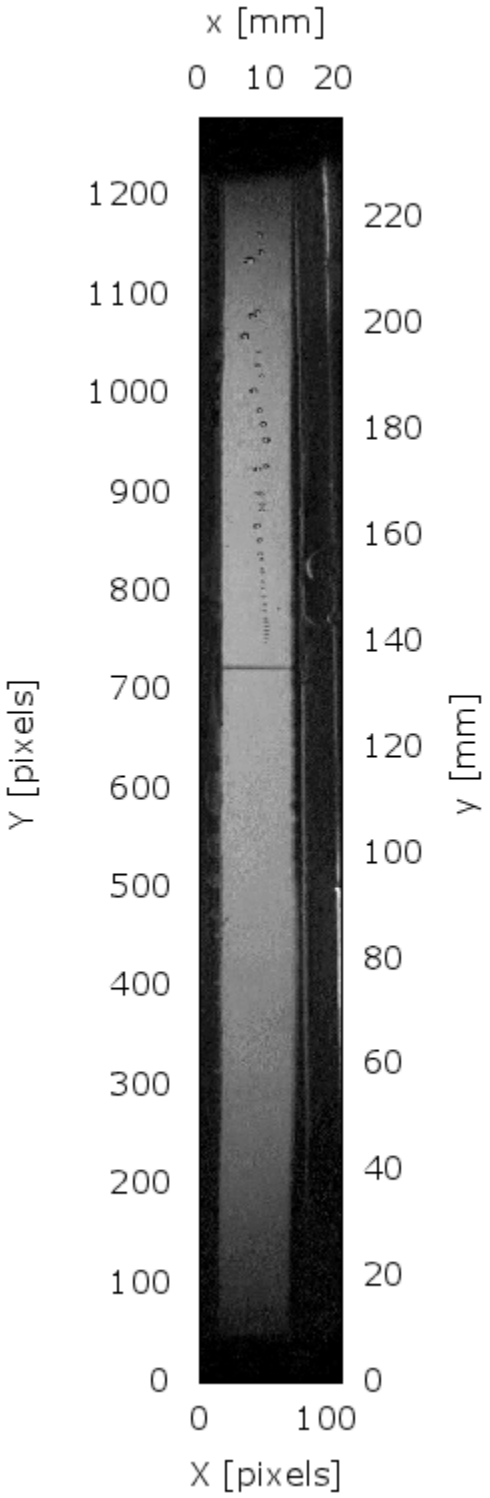

Figure 7.3: Front view shadowgraphy experimental image from camera 2 at a resolution of 186.8 μm/pixel.

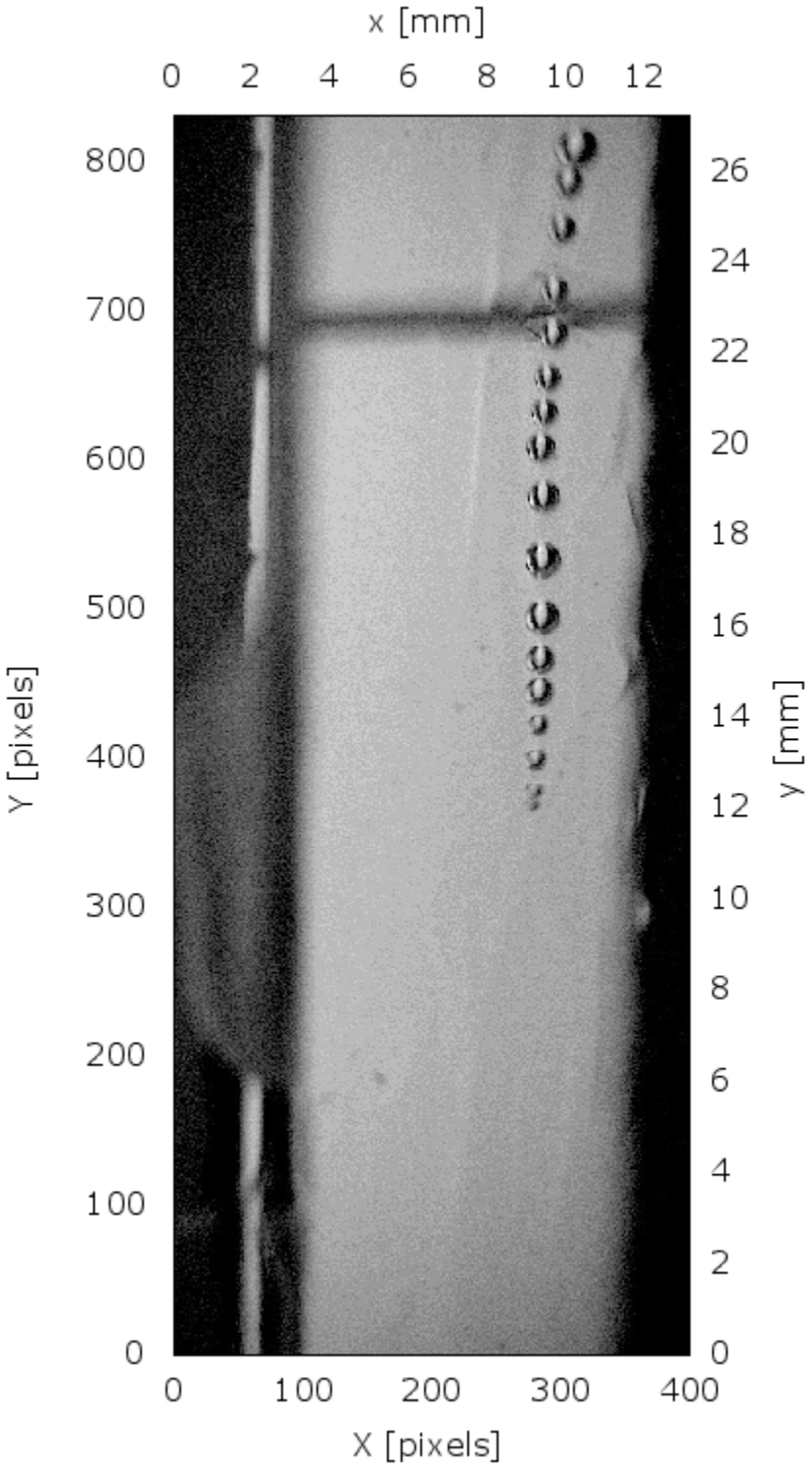

Figure 7.4: Front view shadowgraphy experimental image from camera 3 at a resolution of 32.8 μm/pixel.

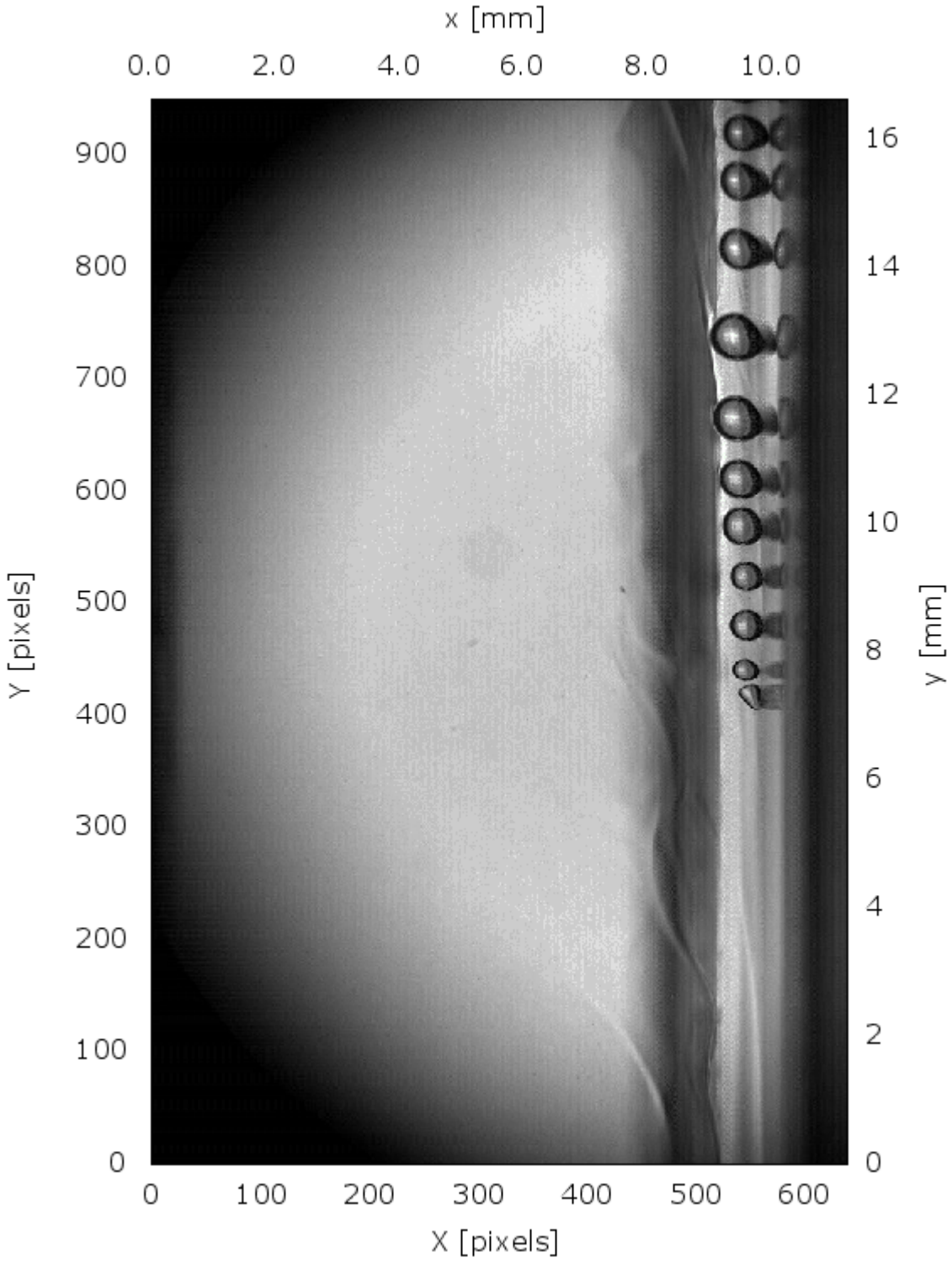

Figure 7.5: Side view shadowgraphy experimental image from camera 1 at a resolution of 17.5 μm/pixel.

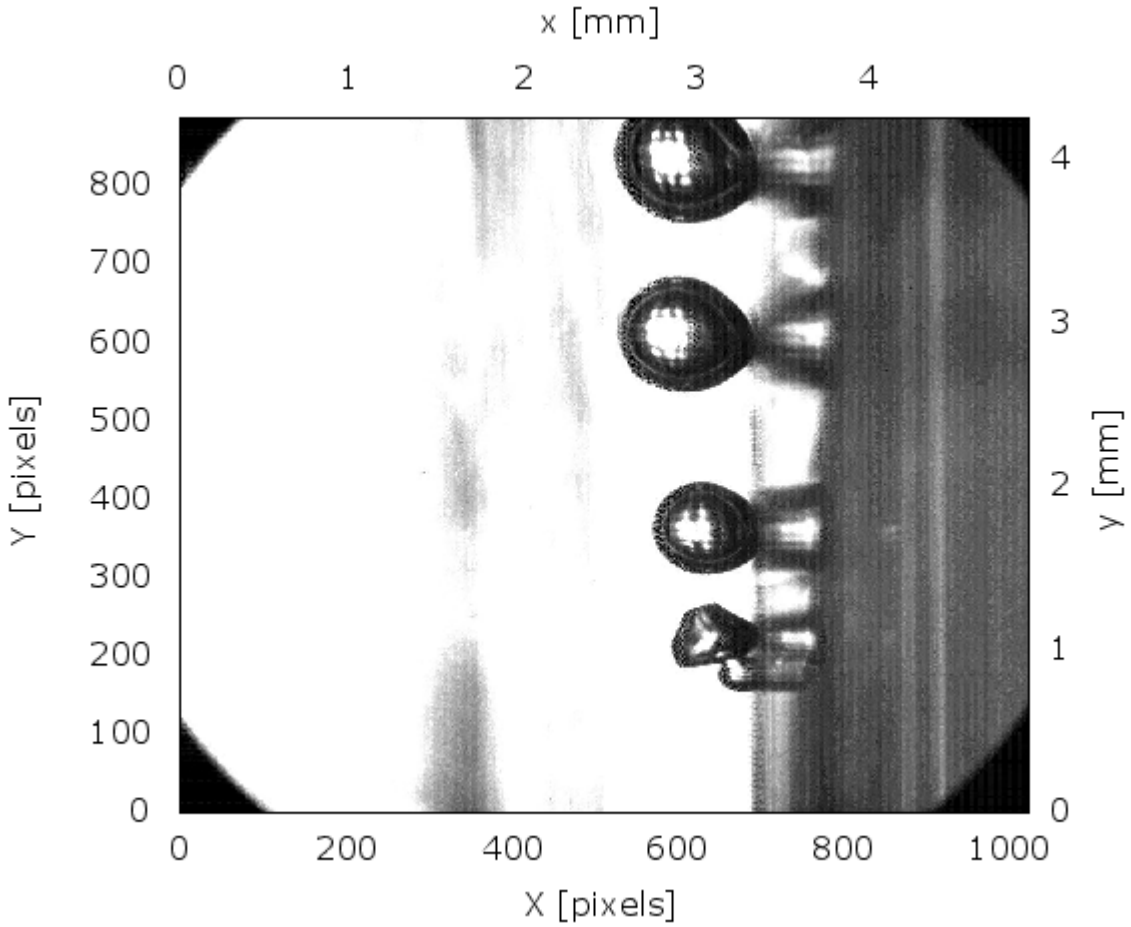

Figure 7.6: Side view shadowgraphy experimental image from camera 1 at a resolution of 4.8 μm/pixel.

of the detached bubbles reduced in size and were pushed back to reattach to the wall. The second common behavior of bubbles that follow Path A, were those bubbles that coalesced with the leading bubble. The motion fluctuations induced by the coalescing process promoted as well bubble detachment. Bubbles that followed path B, consisted on nucleated bubbles that did not detach from the wall, and presented a smooth growing rate as they slid through the wall. The bubbles velocity was intimately related to the bubbles growing behavior. Several points are worth noting: First, the bubbles seems to have an almost constant acceleration at least in the first 3.5 mm after nucleation. However, the axial velocity within 0.25 to 0.75 mm showed to be largely fluctuating. This behavior is explained if considering that at this location, most of the coalescence, detachment and reattachment happens. Another interesting behavior is the normal bubbles velocity at the nucleation site. The bubbles inertia induced by the rapid growing at the nucleation site produced bubbles velocities as large as 0.4 m/s. This velocity is large compared to the maximum axial velocity that was not larger than 0.25 m/s. After this very large velocity increase, the normal velocity tends rapidly to zero.

Insight into the benefits of performing multi-scale measurements can be gained when comparing the results from Fig. 7.7 and Fig. 7.8. Fig. 7.8 shows the synchronized measurements at the same conditions as the ones shown in Fig. 7.8. but from different view point and magnification. Fig. 7.7 shows the high-magnification side-view results, while in Fig. 7.8 are shown the low-magnification front-view results. Fig. 7.7 provides detailed bubble dynamics information, however this measurement is limited to only 3.5 mm from the nucleation site. Fig. 7.8 shows less detailed information but in a larger scale. To make the differences of scales between these measurements clearer, a small rectangle close to the nucleation site in Fig. 7.8 depicts the measurement region from the side-view high-magnification camera. The first

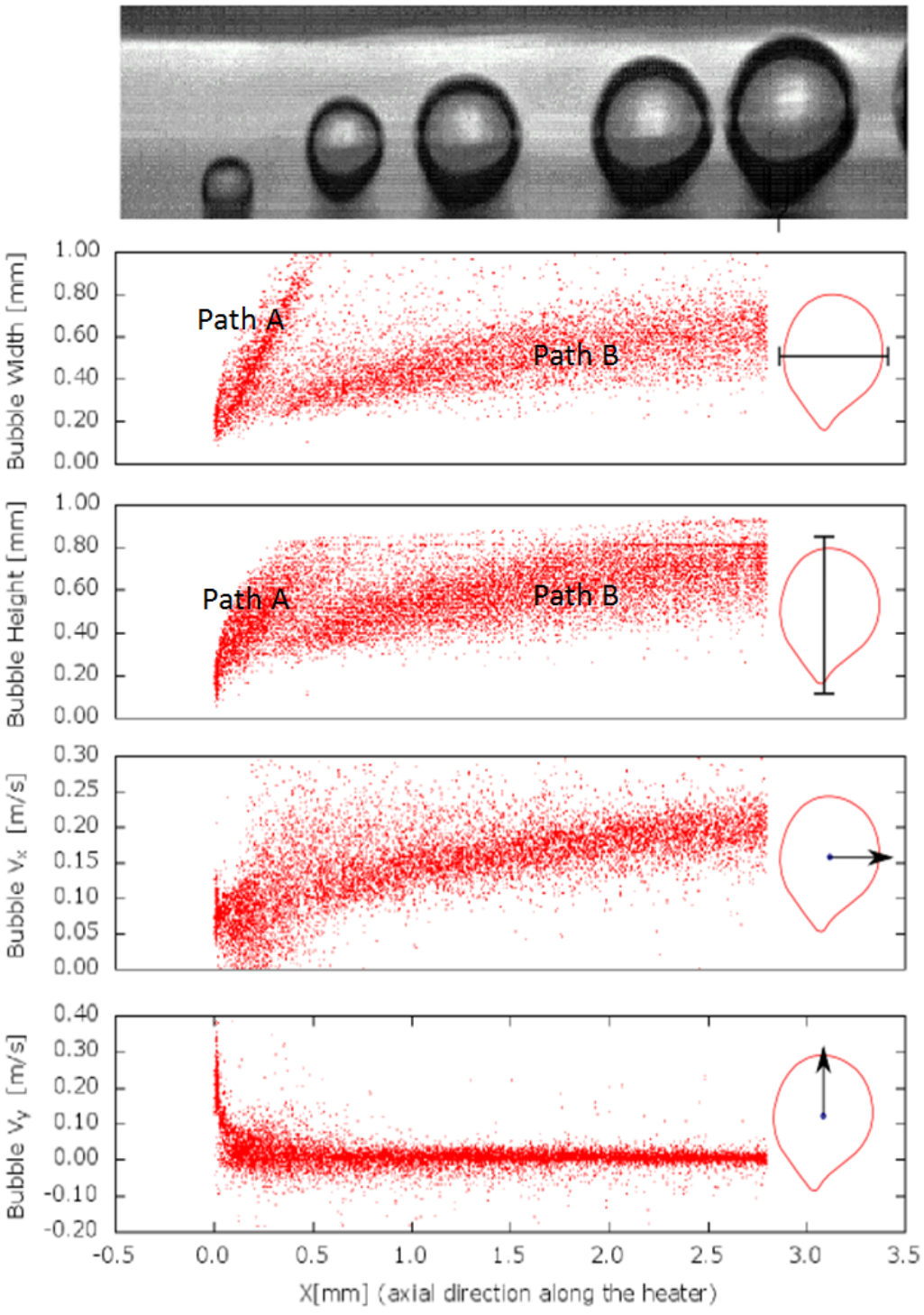

Figure 7.7: Side view high magnification bubble dynamics measurements.

plot of Fig. 7.8 shows the evolution of the probable paths nucleated bubbles may take while sliding through the wall, a uniform dispersion is observed, similar to the spreading of a bubble plume. The second plot of Fig. 7.8 shows the axial velocity of the bubbles, from this plot can be inferred that the terminal velocity of the bubbles is about 0.2 m/s. Bubbles reach to these velocities fairly rapidly, within the first 10mm after nucleation. The velocity component on the direction parallel to the heater (Z direction) is shown in the third plot of Fig. 7.8, This velocity component is very close to zero, however there is a significant increase of this velocity with distance. Sliding bubbles increasing in size reach rapidly to a terminal axial velocity, and show to increase their zigzag motion in the direction parallel to the wall.

7.2.3 Bubble Radius

Statistical analysis form the previous results, allowed the estimation of the bubbles radius as a function of their location along the heater. As shown previously, for these experimental conditions, bubbles slide along the heater gaining size and therefore velocity. The average behavior is seen in Fig. 7.9, where the most probable radius was estimated from the results of the bubbles residence time map, which will be explained in section 7.2.5. As a first approach, the data was fitted to an equation of the form

$$\overline{r\,(x)} = a \cdot x^{b} \tag{7.1}$$

where r is the bubble radius, x is the bubbles axial location at a time t which is the time required to travel a distance x from the nucleation site, i.e. $x = f(t)$, and a and b are fitting constants. Eq. (7.1) was selected because it contains a small number of parameters and it satisfies the fact that at the nucleation site location ($x = 0$),

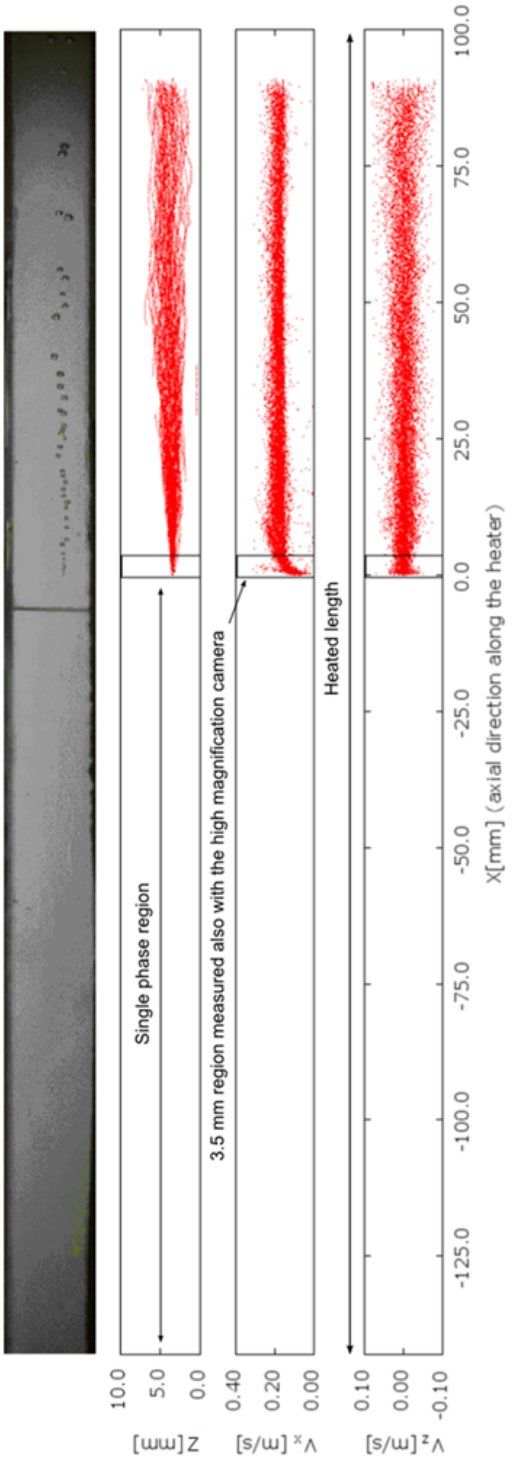

Figure 7.8: Low magnification shadowgraphy visualization for bubble dynamics measurements.

and at the instance just before the nucleation event ($t = 0$) there are no bubbles and therefore the radius may be considered ($r = 0$). The values of the constants a and b may change depending on the experimental conditions.

The fitted equation and the data points are shown in Fig. 7.9. It is important to note, that this data is a good estimation of the local average bubble radius because, as explained before, the used straddling timing provided multiple independent samples of bubbles radius at random locations. The information contained in Fig. 7.9 is essentially different to what is presented in the literature $r(x(t)) \neq r(t)$. However, as can be seen later, this information may be used together with the average bubble velocity to obtain the average bubble growth rate as a function of time.

7.2.4 Bubble Velocities

The bubbles velocities may be estimated by two different approaches. The first approach, is estimating the bubbles centroid velocity (V_{Bc}). This approach provides a single velocity vector for each bubble. The location of the velocity vector coincides with the center of gravity of the bubble. This approach comes naturally when using PTV. Once the object is detected, all object's information are stored in the centroid position, Fig. 7.10a) shows an example of the bubbles velocity measurements by means of the bubble centroid velocity approach. The second approach is the so called bubble binning velocity expressed as V_{Bb}. This approach starts by dividing the bubbles in multiple components or bins, and considering each bin as an independent component. Each bubble component will contribute differently to the bubbles velocity. For example, the top of the bubble, which is farther from the wall, will be exposed to higher liquid velocities and therefore it is expected that it will experience a larger velocity. In the other hand, the bubble neck is expected to travel at lower velocities due to the wall drag and due to the lower liquid velocities in the near wall region.

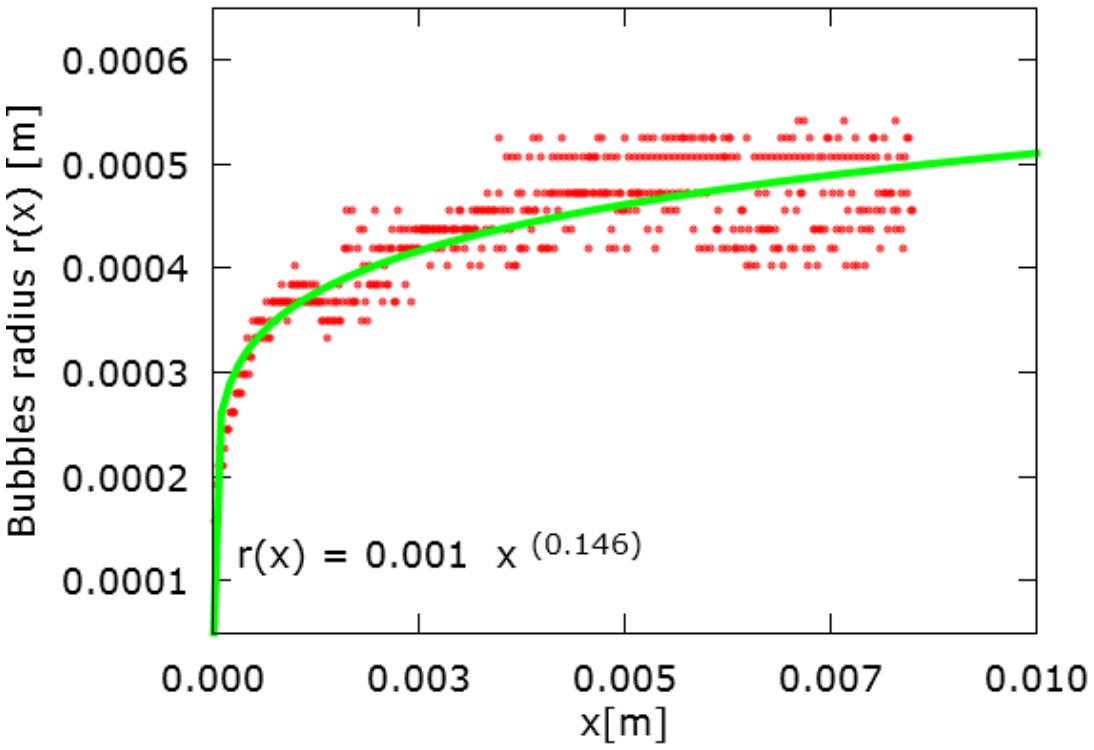

Figure 7.9: Average bubble radius as a function of bubble location from the nucleation site $r = f(x(t))$.

Axial bubbles velocity measurements of wall-normal average profiles at different axial locations (x) are shown in Fig. 7.11. The two approaches to estimate the bubbles velocities are presented in this figure for comparison. The differences between the two approaches is considerably large. These difference are explained by the way the statistics are computed. To obtain a profile, the data has to be divided in bins. and the random vectors within the bins are the source to estimate the average quantities. When considering the bubble centroid velocity approach, the information of the whole bubble's body is collapsed into its centroid, loosing much of the spatial information. This information collapsing gives the following effects on the estimated profiles, first, information is not available for regions bellow or above the minimum and maximum bubble radius. This explains the limits of Fig. 7.11(a) which go from about $y = 0.15$ to 0.5 mm. Indicating the range of bubbles radius. Secondly, it appears that there is a big velocity difference between near-wall and far from the wall bubbles for each axial location, but in reality this large velocity gradient is an indication that larger bubbles have larger velocities than smaller ones, and considering that most of the bubbles are sliding through the wall, it may be useful in this plot to consider the wall-normal location equal to the bubble radius $y = B_r$. In contrast, Fig. 7.11(b) shows the bubble binning velocity approach results. The first striking difference with the bubble centroid velocity approach is the fact that the information provided covers a larger range of y locations, from $y = 0$ to $y = 1.0$ mm. The near-wall information comes from parts of the bubbles neck which touch and slide through the wall. It is noteworthy to mention that at the location $y = 0$ the bubbles velocities are different from zero $V_{Bb} \neq 0$, and in fact, near-wall bubble velocity differ just slightly to the bubble velocity far from the wall. This slight difference of say, bubbles necks and bubbles tops velocities is explained by the influence of the liquid velocity gradient and wall drag. For the sake of understanding the influence that the amount

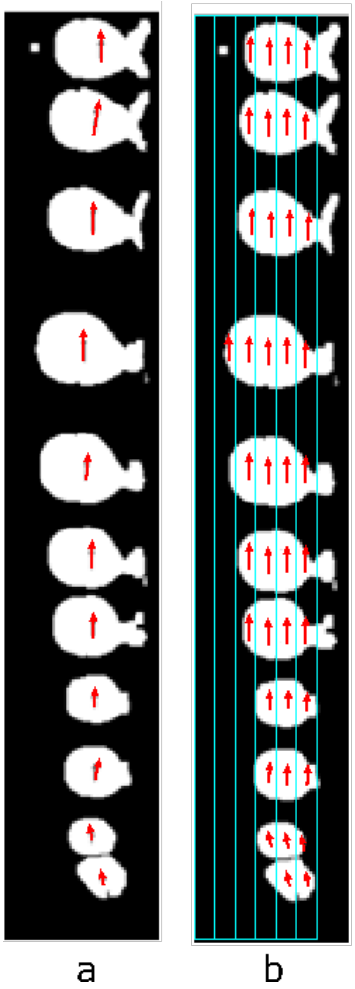

Figure 7.10: Estimation of bubbles velocities by a) bubbles centroid velocity approach, and b) bubbles binning velocity approach.

of void at certain location has on the local liquid turbulence properties, the bubble binning velocity approach results were selected to account for the bubbles dynamics estimation.

From these results, the bubbles average velocities were estimated at different locations along the heater wall. giving the results shown in Fig. 7.12. This information was fitted with an equation of the form

$$V_B\left(x\left(t\right)\right) = c \cdot x^d \tag{7.2}$$

where V_B is the bubble velocity, and c and d are fitting constants. Eq. 7.2 was selected because it satisfies the fact that at the nucleation site location ($x = 0$), and at the instance just before the nucleation event ($t = 0$) there are no bubbles and therefore the velocity may be considered ($V_B = 0$). The values of the constants c and d may change depending on the experimental conditions.

7.2.5 Void Residence Time or Void Fraction

To obtain accurate results of the bubbles residence time or void fraction, we based our analysis similar to what is used on point measuring probes, such as Beattie (1972), on which a definition of the void fraction is given in terms of the bubbles residence time as follows: Consider point values in the fluid that are either gas values or liquid values. The instantaneous description of this flow may be simplified by introducing a binary variable, δ, having the value one (or zero) if the point considered is in the gas (or liquid) region.Âă The ensemble average of this quantity δ at a point in the flow, or the probability that gas is at the point, is the local void fraction α.

$$\overline{\delta} = \alpha \tag{7.3}$$

The cross sectional average of the local void fraction α, differs from a widely used definition of void fraction as the fraction of cross section occupied by the gas phase. In the present notation, the latter definition is in fact δ. Note that the ensemble average of this coincides with α since $\overline{<\delta>} =<\overline{\delta}>=<\alpha>$.

In this work, with binarized images, every pixel is considered as a point probe from which δ can be estimated at each position. The ensamble average of the binary

images will provide a 2D map of $\overline{\delta}$. The results of this procedure is given on the left picture of Fig. 7.2. The 2D ensamble average map shows the overall behavior of the bubbles. It is interesting to note that the maximum residence time is found in the nucleation site location, which is about 80 %, later downstream the bubbles spread and grow on size but reduce on residence time. To gain more insight into the details of the residence time features along the heater, wall-normal profiles of the void residence time are shown in Fig. 7.13. From this figure is clear that the maximum void residence time was reduced from a value of about 80% in the nucleation site to a value of about 45% 7 mm downstream the nucleation site. It was found that the y location of the maximum residence time value coincided with the average bubble radius $\overline{B_r}$ at each axial location (x). This fact is important because the procedure to obtain the void residence time is much simpler than locating and estimating individual bubbles and estimate from there their centroid.

7.2.6 Bubbles Growth Rate as a Function of Time

The bubble growth rate as a function of time dr/dt may be obtained by following an individual bubble during a period long enough to cover its life-time. However, this methodology needs a large number of samples. In this context, one sample will be the equivalent of all the camera frames used to follow a given bubble through its life-cycle. The amount of frames will depend on the camera frame-rate, viewing area and on the experimental conditions, but typically each sample requires from 50 to 200 frames. Furthermore, it is necessary to locate the instances of bubble nucleations to start each sample. This is cumbersome and time consuming, and more importantly it is computational and memory expensive. Previously, it was mentioned that the straddling timing mode provides statistically sufficient number of samples, but any information regarding the timing of the bubbles growth is somehow hidden.

This section shows the procedure to obtain the bubble temporal growth rate from measurements using the straddling timing condition.

We start by considering the relevant information that can be delivered by the straddling timing mode, which include the bubble radius as a function of the axial distance, $r\left(x(t)\right)$, and the bubbles velocity also as a function of the axial distance, $V_B\left(x(t)\right)$. This functions are available from Fig. 7.9 and Fig. 7.12, and were fitted with Eq. (7.1) and 7.2 respectively.

The temporal information is contained in the bubbles velocity expression. The time will depend on the axial location from the nucleation site. With this consideration we can extract the time t_n required to reach certain position x_n with the following procedure.

$$V_B\left(x(t)\right) = \frac{dx}{dt} = c \cdot x^d$$

separating variables and integrating,

$$\int_{x=0}^{x=x_n} x^{-d} dx = \int_{x=0}^{x=t_n} c \cdot dt$$

or, solving for the time,

$$t_n = \frac{x_n^{(1-d)}}{c \cdot (1-d)} \tag{7.4}$$

this simple procedure will allow us to plot r as a function of t. Further validation of this procedure is available when we consider that the temporal bubble growth rate may be expressed as

$$\frac{dr}{dt}\left(x(t)\right) = \frac{dr}{dx} \cdot \frac{dx}{dt} \tag{7.5}$$

Recalling the expression for the bubble radius,

$$r\left(x(t)\right) = a \cdot x^{b}$$

then, we can obtain

$$\frac{dr}{dx} = a \cdot b \cdot x^{(b-1)} \tag{7.6}$$

Also the bubble velocity may be expressed as

$$V_B = \frac{dx}{dt} = c \cdot x^{d} \tag{7.7}$$

substituting the previous equations into Eq. (7.5), we obtain:

$$\frac{dr}{dt} = \left[a \cdot b \cdot x^{(b-1)}\right] \cdot \left[c \cdot x^{d}\right]$$

or

$$\frac{dr}{dt} = a \cdot b \cdot c \cdot x^{(b+d-1)} \tag{7.8}$$

This expression relates the temporal growth rate in terms of fitting constants at a given location x. To test the feasibility of the previous procedure, we can compare with Zuber correlation (Zuber and Findlay, 1965), which is expressed as:

$$r/r_m = (t/t_m)^{1/2}\left(2 - (t/t_m)^{1/2}\right) \tag{7.9}$$

Using the derivative of this correlation we obtain

$$\frac{dr}{dt} = \frac{r_m\left(2 - \sqrt{\frac{t}{t_m}}\right)}{2\sqrt{\frac{t}{t_m}}t_m} - \frac{r_m}{2t_m} \tag{7.10}$$

Now we are in a position to extract the temporal information from our straddling measurements. By doing so, we can plot the comparisons with the Zuber (Zuber and Findlay, 1965) correlation shown in Fig. 7.14.

Surprisingly, there are little discrepancies for both plots (r/r_m and dr/dt). First, considering the comparison of the dimensionless radius (r/r_m), Zubber correlation underestimates in regions of low and high dimensionless times (t/t_m). This discrepancies are expected because Zuber correlation requires a characteristic time and a characteristic radius (t_m and r_m). These should correspond to the values on which the maximum radius is found, just before bubble detachment. We have to recall that in our experiments, no significant bubbles detachment was found, and it appear that the measuring area was not long enough to capture the maximum or terminal bubble sizes.

This satisfactory agreement with theoretical correlations, give us an indication of the correctness of our procedure to estimate average bubbles dynamics.

7.3 Liquid Turbulence Statistics

7.3.1 Average Liquid Velocity

One of the main objectives of the PTV measurements is to obtain detailed information of the liquid velocity close to the heated wall under subcooled boiling conditions. Fig. 7.15 shows the average axial velocity profile at different x axial locations along the heater. The color bar indicate the axial distance from the nucleation site, starting with the light blue for locations on which only single phase flow is located, the darkest blue represents the location after 8 mm downstream the

nucleation site. The influence of the boiling bubbles on the liquid velocity is clear. There is a local peak in the region close to the wall. This local peak is related to the average bubble radius measured at each axial location. Closer examination of the average residence time profiles from Fig. 7.13 gives a clear indication that the bubbles layer do not extend further than 1 mm from the wall. This position coincides with the limit on which the liquid velocity appear to be influenced by the bubbles induced momentum.

To have a better understanding of the liquid behavior, it is always convenient to present these results in dimensionless form. The characteristic length and velocity used for the non-dimensionalization are $y^+ = (yu_\tau)/\nu$ for the characteristic length and u_τ for the characteristic velocity, u_τ is the friction velocity defined as $u_\tau = \sqrt{(\tau_w/\rho)}$. The wall shear stress (τ_w) is obtained experimentally using the approximation for regions close to the wall as $\tau_w = \mu \left.{}^{du}/_{dy}\right|_{y=0}$. From the previous definitions we found a frictional velocity of $u_\tau = 0.0125 m/s$. It is important to note that the heated single phase friction velocity was considered for all cases. Fig. 7.16 shows the non-dimensional form of the axial velocity profile at different axial positions. From this plot it is clear a significant difference from the single unheated case (shown in red). These differences are attributed to the gravity driven flow induced in the vicinity of the heated wall. The effect of the boiling level in the liquid velocity was previously observed (Estrada-Perez and Hassan (2010). However, the present experiments focused in a single nucleation site, allowing to have different void fractions depending on the axial (x) position. Therefore, a single heat flux condition will provide different local void fractions, which simplified greatly the experimental and analysis work. In Fig. 7.16 the red and gray vertical lines represent the limits of the viscous sublayer ($y^+ < 5$) and that of the buffer layer ($5 < y^+ < 30$) respectively. Also, it is clear that the largest influence of the boiling bubbles is confined in the buffer region, but affects

significantly the viscous sublayer. The latter observation may be explained from the analysis of the bubbles dynamics. In the viscous sublayer region a reduced amount of void was found. This region is affected mostly by either really small bubbles or by the bubbles neck which slide through the wall. The liquid in the viscous sublayer experience an induced momentum due to the slower moving bubbles neck, and at the same time, a deceleration due to the wall induced drag. Liquid in the buffer is less affected by the wall drag and experience an induced momentum by the bubbles centroids.

The concomitant velocity increase with distance from the nucleation site (x) is similar to the behavior found previously by Estrada-Perez and Hassan (2010). However, in the present study the profiles variation source is an increase on distance, instead, the profiles variation found in (Estrada-Perez and Hassan, 2010) was due to an increase on heat flux. No matter what is the source of profile variation, either x or q'', in both cases this velocity profile variation seems to be fairly smooth process, with the exception for regions close to the nucleation site. An abrupt change on the velocity profiles was found in the transition from single-phase flow to a two-phase flow condition, i.e. The regions before the nucleation site show an similar velocity profile, and just after the nucleation site region, the liquid velocity profiles are changed abruptly, and transition towards an almost fully developed region far from the nucleation site.

7.3.2 Liquid Turbulence Intensity

The turbulence intensities are a good indication of the turbulence levels and turbulence modification due to the boiling process. In this context, An increase of turbulence is expected due to the induced mixing and stirring of the liquid by the boiling bubbles. Fig. 7.17 shows the non-dimensional axial turbulence intensity profiles

($u'^{+} = u'/u^{*}$) at different axial lengths (x) from the nucleation site. The expected increase in turbulence induced by the bubbles is evident. The axial turbulence intensity behavior is not as smooth as the observed by the liquid velocity, as a matter of fact it is easy to discern the single phase cases to the two phase cases due to the abrupt increase on intensity of the profiles. This abrupt change appeared just after the nucleation site location ($x = 0$). The development of the turbulence intensity profiles from the single phase behavior ($x <= 0$) to a fully developed two phase flow profile happened just after the first 3 mm from the nucleation site ($x > 3\ mm$), after which, no significant increased was observed. Although the velocity profiles showed some similarity to the case of fully developed bubble layer with changing heat fluxes (**?**), the axial turbulence intensities does not. In previous studies ((Estrada-Perez and Hassan, 2010; Roy et al., 2002; Velidandla et al., 1996)), the axial turbulence intensity showed a smooth transition with changes on the heat flux, this is an indication that the heat flux is not the dominant parameter in the induced turbulence, rather, we should look at the behavior of local void properties. The only other parameter that changes abruptly with distance is the bubble diameter. As explained previously the bubbles reach to a terminal size value fairly rapidly, in fact for a bubble to reach this terminal size require it to slide only about 3 mm from the nucleation site. This may explain the abrupt changes of the axial turbulence intensity.

Fig. 7.18 shows the wall-normal turbulence intensity ($v'^{+} = v'/v^{*}$) as a function of the axial distance from the nucleation site. Similar to the axial turbulence intensity behavior, the boiling bubbles brought significant changes to the profiles. However, profile changes were not as abrupt. A smoother transition from the single phase region to the fully developed region was observed. Nonetheless, the difference between the single phase regions and the two phase regions is quiet noticeable. After the nucleation site location, a significant increase in the normal turbulence intensity

was found, thereafter, a smoother development to the fully developed region was observed. The bubble dynamics may play a significant role in this behavior. The liquid surrounding the bubbles is displaced mostly in the normal direction, the liquid displacement intensity will depend on the bubble size and velocity, which do not change much after the very first 3 mm from the nucleation site. Thereafter the bubbles continue to grow but in a much smaller rate, this may explain the smooth and gradual increase on turbulence intensity in regions far from the nucleation site.

7.3.3 Liquid Reynolds Stresses

The Reynolds stresses ($u'v'^{+} = \overline{u'v'}/u^{*2}$) are plotted in Fig. 7.19. As expected, the boiling bubbles brought significant changes to the profiles. The single phase Reynolds stresses behavior (light-blue profiles) is clearly identified, there is an increase in regions close to the wall, and a gradual decrease towards zero at half height of the channel ($y = 5\ mm$). However, for the two phase cases, downstream the nucleation site, there are huge fluctuations on the turbulence intensities and no trend is clearly identified. The reason of this large fluctuations may be due a lack of samples. To estimate the turbulence statistics, it was needed to divide the image not only in the direction normal to the wall (y^{+}), but also in the axial direction (x). This to account for the fact that we are measuring a transitory event that develops along the axial direction. In previous studies Estrada-Perez and Hassan (2010) more samples were available to estimate the Reynolds stresses because the whole image captured regions at fully developed conditions, therefore there was need to divide the data in the axial directions.

7.4 Near-Wall Void Influence in the Liquid Profile

The previous results provided detailed information of the liquid and bubbles parameters with an emphasis to near-wall measurements. With this information is possible to discern the true influence that the bubbles parameters has on the liquid turbulence. Many attempts had tried to develop a two-phase flow function to describe the liquid profiles in terms of local two-phase flow parameters (Beattie, 1972; Končar and Tiselj, 2010; Marie et al., 1997; Sato and Sekoguchi, 1975; Troshko and Hassan, 2001), however the results leave much room for improvement. In this section we explore the feasibility of using the measured liquid and vapor parameters for the model development of the near wall liquid velocity profile specially tailored for subcooled boiling flow. Two approaches are considered, the first approach, rather than giving a formal generalization, provides, based on experimental information, ideas that can be beneficial of future subcooled boiling modeling efforts. The second approach starts with a simplified version of the phenomena to try to approach the problem more physical ground.

7.4.1 First Approach - Empirical Correlation

For the sake of simplicity we started with empirical expressions which holds no physical interpretation, to see how its parameters change and how they can be related to physical quantities.

using the non-dimensional velocity profiles presented previously in Fig. 7.16 it was decided to fit points from the viscous sublayer up until the position on which the largest influence of the bubble layer was located. This position was selected as the average bubble radius. with the following equation:

$$U^{+}_{fit}\left(y^{+}\right) = A1 + B1\left(y^{+}\right)^{1/2} \tag{7.11}$$

Fig. 7.20 shows how the equation fit closely the liquid velocity profiles at three different axial locations. It has to be remembered that depending on the axial location, different two-phase flow parameters are found. This give us the opportunity to see the influence of these parameters on the behavior of the fitting constants.

After the fitting procedure was repeated for fifty different locations along the $x-$axis, the found values for $A1$ and $B1$ are shown in Fig. 7.21. The values of $A1$ and $B1$ show practically no change for the single phase cases, however, when reaching the nucleation site region, the values of both fitting constants are different depending on the location. Since $A1$ presented the largest changes, it was decided to fix the value of the $B1$ parameter to $B1 = 2.0$. After doing so, the fitting procedure was repeated leaving $A1$ as the only fitting parameter. The results showed to be quiet acceptable with little change on fitting strength. The values obtained for the $A1$ parameter slightly changed, although showing a smoother behavior. These values are shown in Fig. 7.22.

Close examination of the parameter $A1$ behavior, suggested similarities to the way bubbles change on size and velocity while they slide and grow through the heated wall (see Fig. 7.9 and Fig. 7.11).

For sake of comparison, the bubble velocity, the bubble radius and the $A1$ parameter were normalized using their maximum values, $r^* = r/r_{max}$, $V_b^* = V_b/V_{b,max}$, and $A1^* = A1/A1_{max}$. and were plotted together in Fig. 7.23. The similarity of $A1$ parameter with the bubbles parameters is remarkable. Showing that Eq. (7.11) may be a good model if some physical significance is given to the parameters $A1$ and $B1$.

7.4.2 Second Approach - A Proposed Physically Based Model

The second approach provides a more physically meaningful model that can predict changes on the liquid velocity due to the local properties of the gas phase. It is

similar in nature to the one proposed by Sato and Sekoguchi (1975), and started from experimental observations on which it appear that the bubble layer acted as a moving wall which induce momentum to the neighboring liquid. This model is represented schematically in Fig. 7.25. The important experimental observations that play a role in the suggested model are as follow. The bubbles while sliding, behave as a moving wall inducing the maximum momentum at the region of the bubbles average radius. Furthermore, the bubble sliding through the wall induce a non-zero velocity in the near-wall region. For the present experimental conditions this slip velocity is always smaller but proportional to the bubbles wall velocity, $u_{slip} < u_b$. Also it is considered that there exist a pressure drop that will keep the liquid moving in the axial direction. The previous model therefore requires local two-phase information, such as bubbles sizes, velocities and void fractions. This information is readily available from the experimental results.

Using the superposition of the solution of the pressure driven laminar flow through a channel, and a Couette flow with one wall moving at the velocity of the bubbles and another wall moving at the slide velocity, we obtain (see Appendix A for derivation):

$$u(y) = (1 - \eta)\left[\xi D_b^2 \eta + u_{slide}\right] + \eta V_b \tag{7.12}$$

where η is the dimensionless length normalized with the bubble radius (r_b), ξ depends on the pressure drop, and gravity forces and is considered constant. u_{slide} is the velocity of the bubbles necks, to simplify the application of this equation, u_{slide} may be considered proportional to the average bubble velocity $u_{slide} \propto V_b$

Although we have all the experimental parameters required to test Eq. 7.12, it can not be directly applied to fit the given experimental conditions. The assumptions made to derive this equation require the addition of artificial parameters to serve as

adjusting factors. The adjusting factors are given next

$$V_b' = A \cdot V_b$$

$$u_{slide}' = B \cdot V_b$$

$$D_b' = C \cdot D_b$$

The adjusting parameters (A, B, and C) were found by using the expressions (Eq. 7.1, and Eq. 7.2) for the bubble parameters as a function of the axial distance, and the fitting procedure described previously.

Constant values for each parameter were found, without hindering much the fitting strength of Eq. 7.12. The fitting performance can be seen in Fig. 7.24, on which the red line represent the fitting equation. The green light dots represent the data fitted. The black vertical line determines the average radius depending on the axial position selected. The black arrow will determine the valid domain of the equation. The gray symbols at the right of the black arrow, shows the behavior of the equation on regions that no bubbles should exist, and therefore the equation should not be valid. The behavior of the proposed model provides an acceptable prediction of the liquid velocity based on the local two phase parameters. This model perform better for the regions on which the bubble layer remains constant, for regions closer to the nucleation site, on which the bubbles are still in their developmental stages, this equation appear to over-predict the liquid velocity.

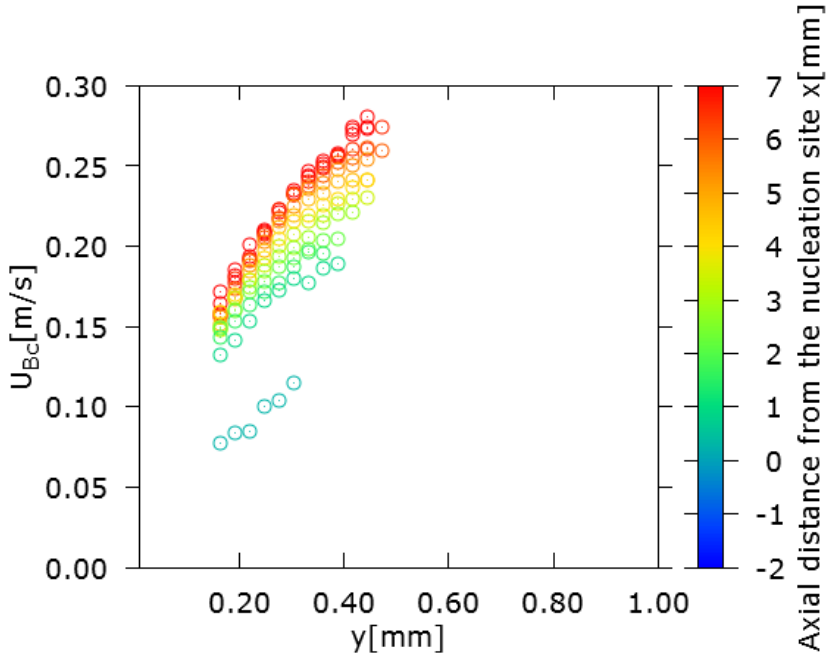

(a)

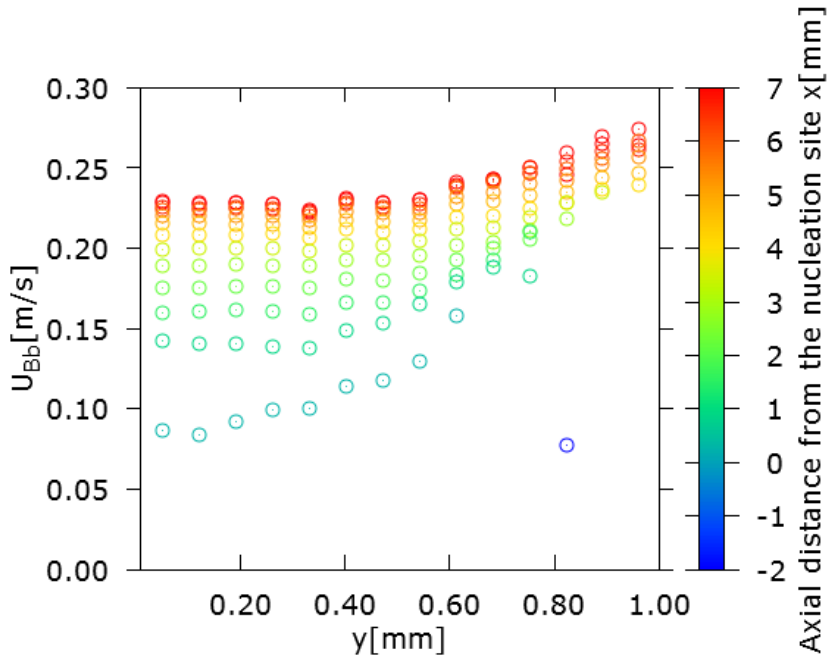

(b)

Figure 7.11: Wall-normal profile of the bubbles axial velocity component, estimated by a) centroid bubble velocity approach, and b) gas binning approach.

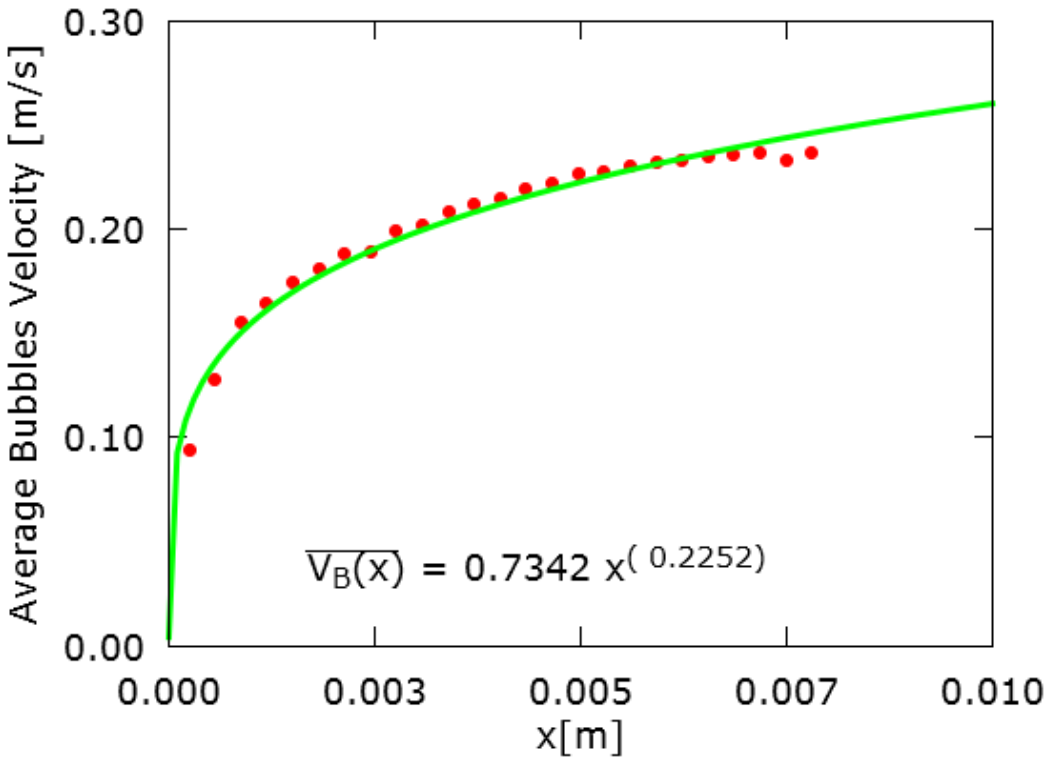

Figure 7.12: Average bubbles velocities in the axial location.

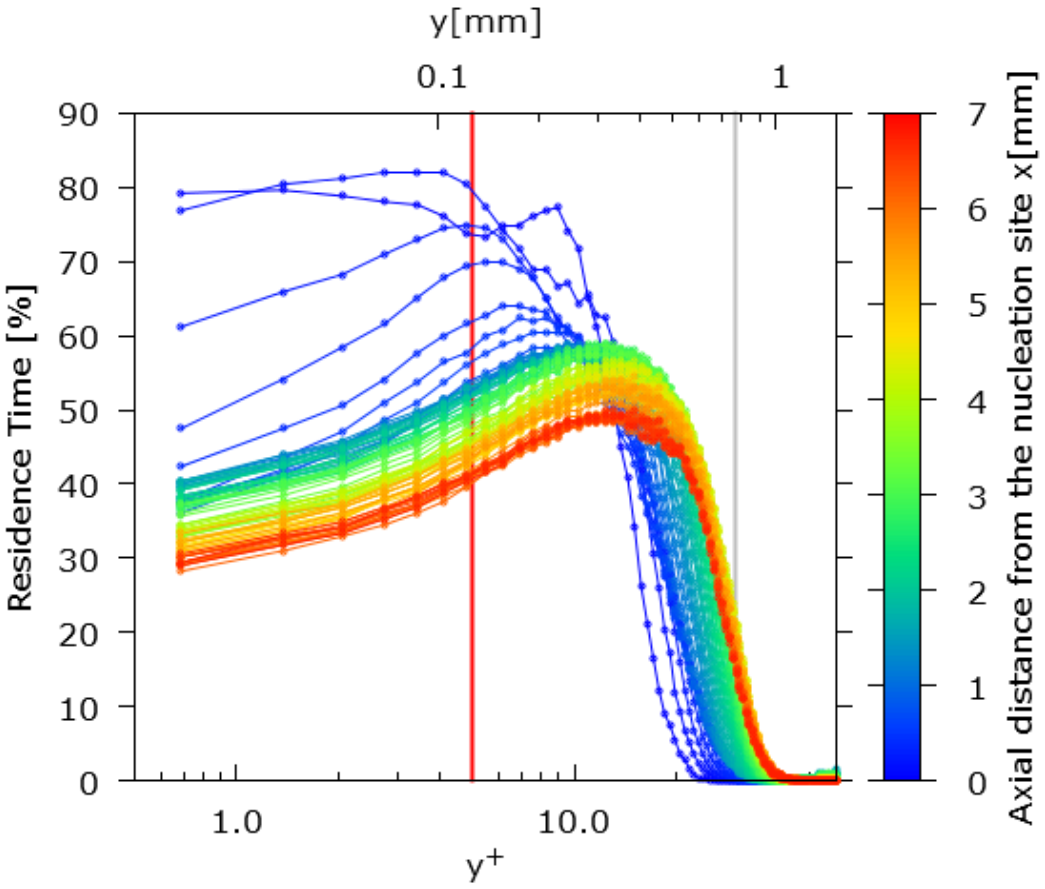

Figure 7.13: Wall-normal profiles of void residence time as a function of the axial location.

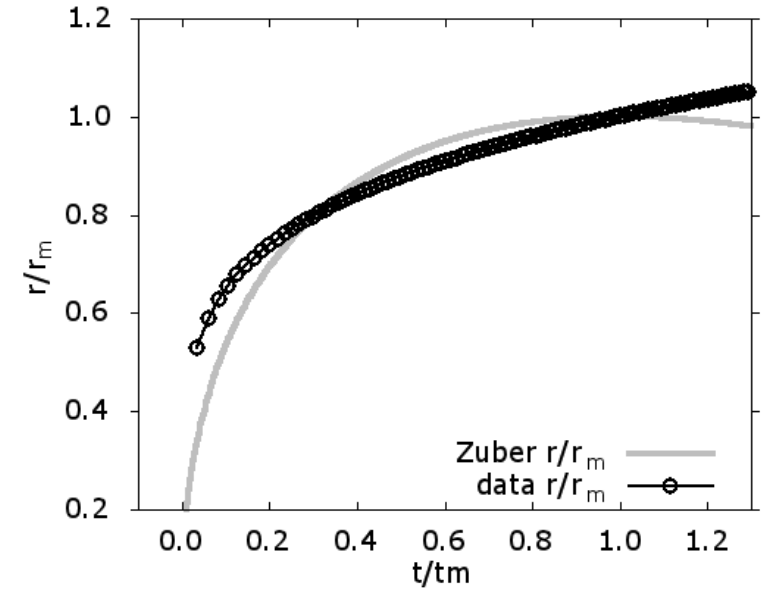

a)

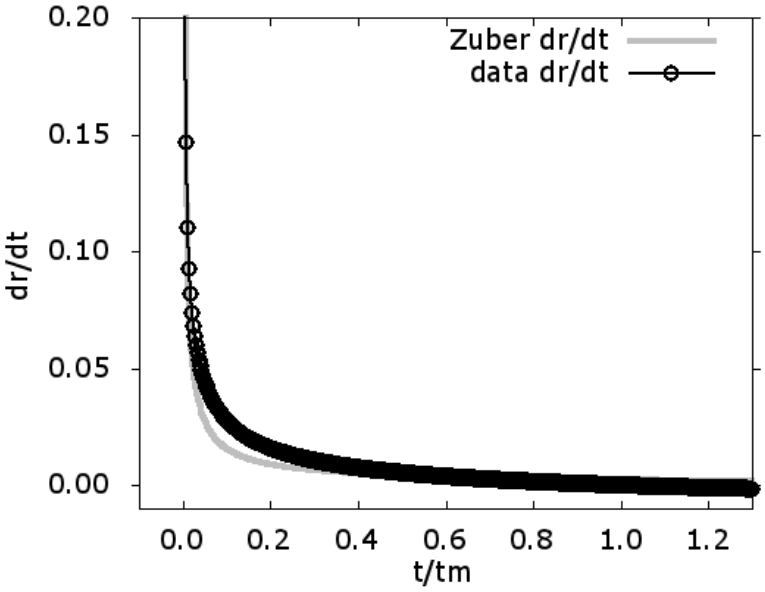

b)

Figure 7.14: Comparison of experimental data with Zuber correlation: a)dr/dt, and b) r/r_m. Both as a function of the dimensionless time t/t_m.

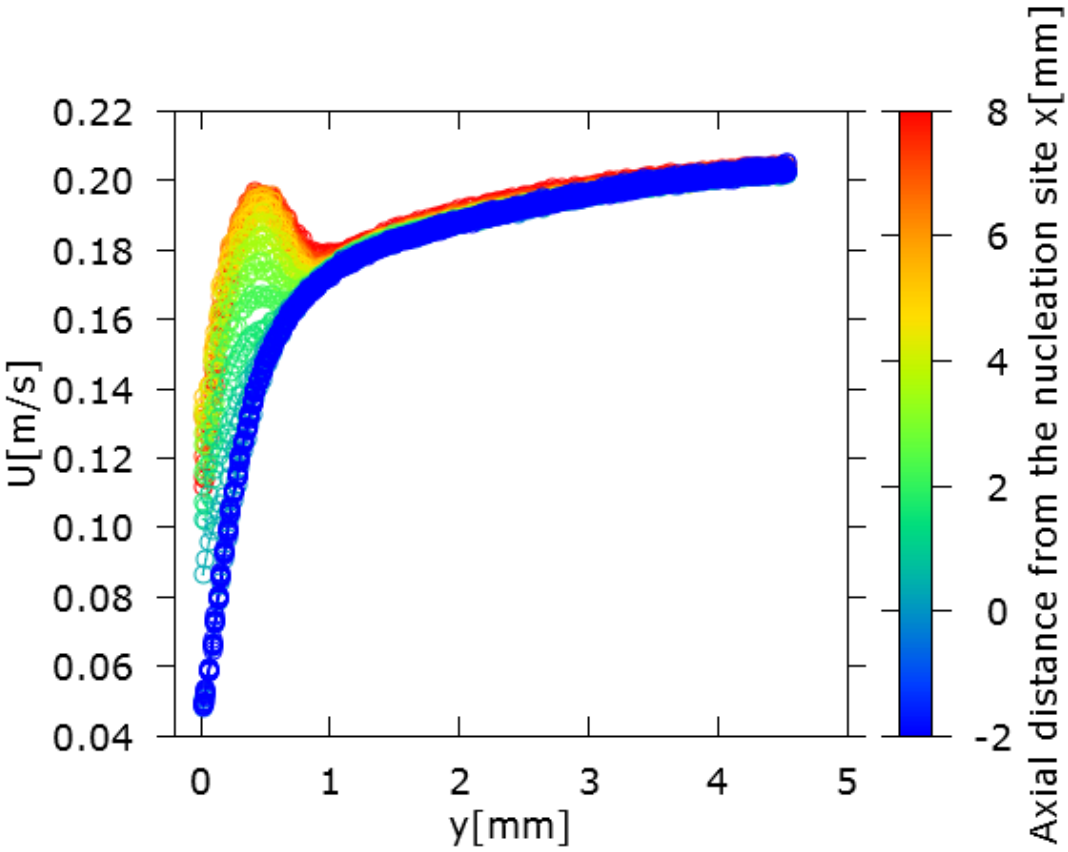

Figure 7.15: Axial liquid velocity profile at different axial positions from the nucleation site.

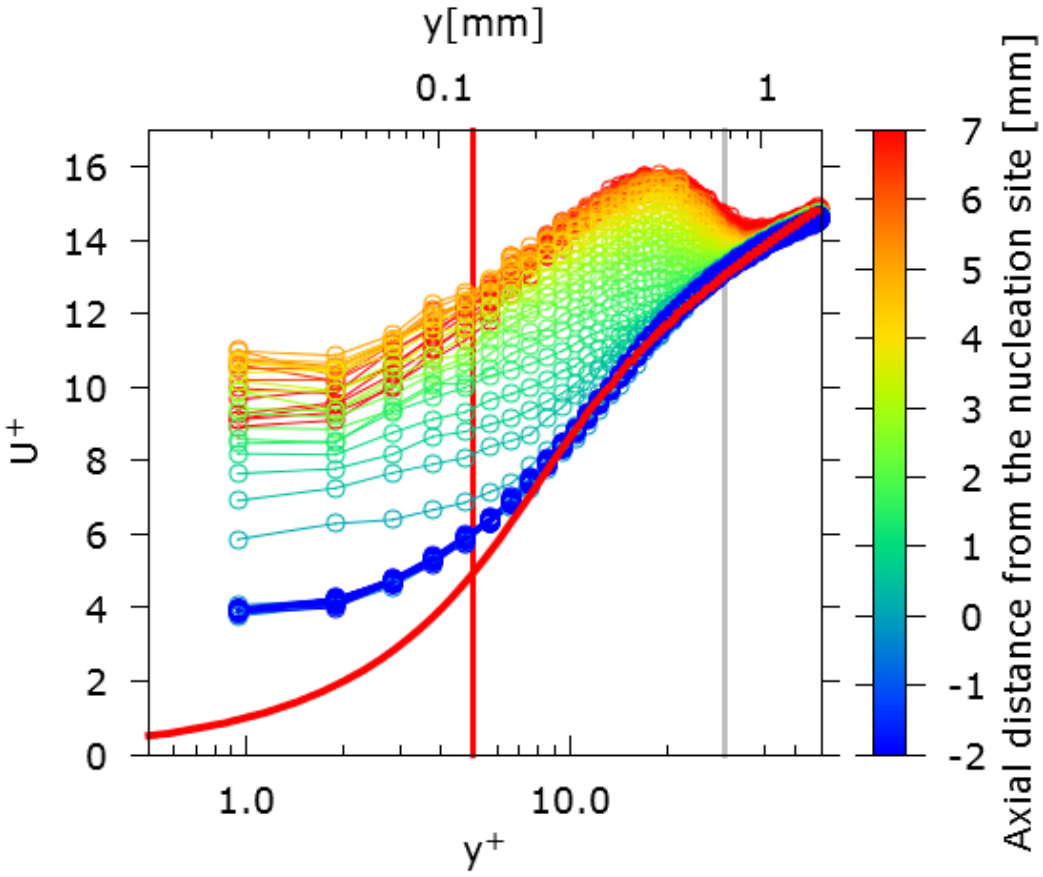

Figure 7.16: Non-dimensional axial liquid velocity profile at different axial positions from the nucleation site and the single phase unheated law of the wall (red-line).

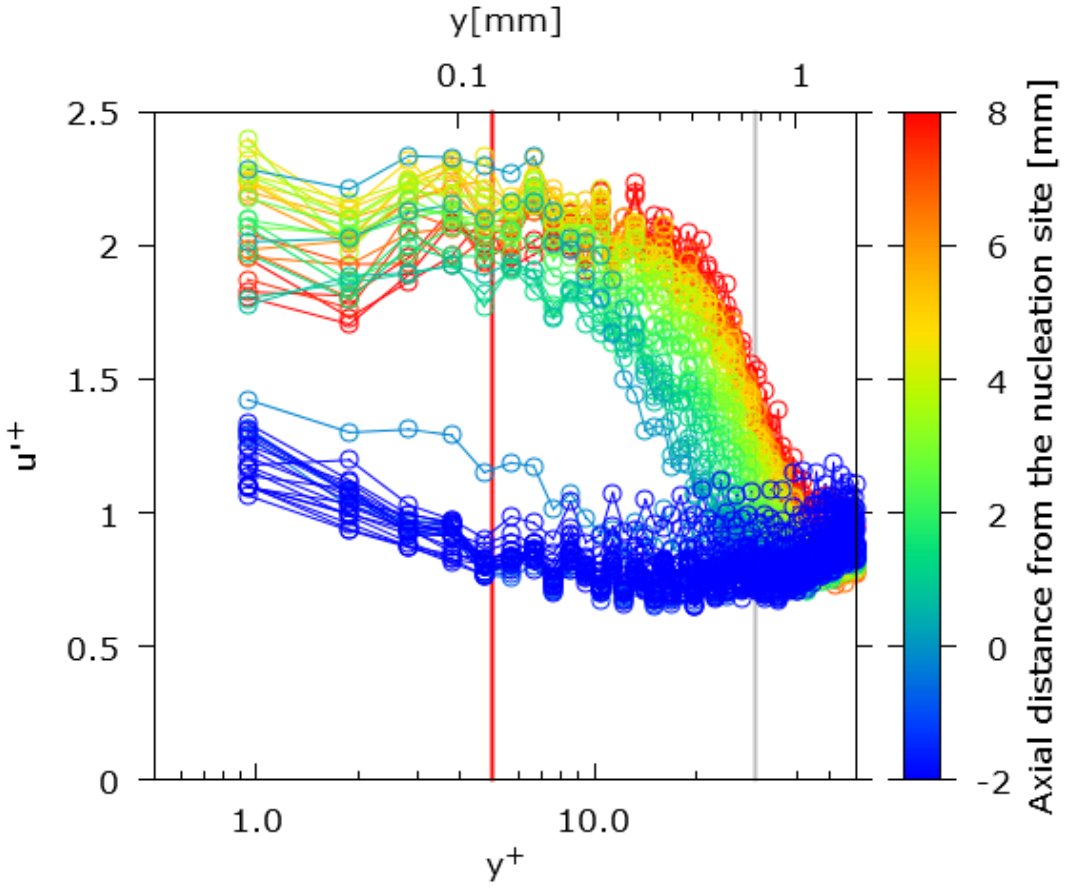

Figure 7.17: Axial turbulence intensity.

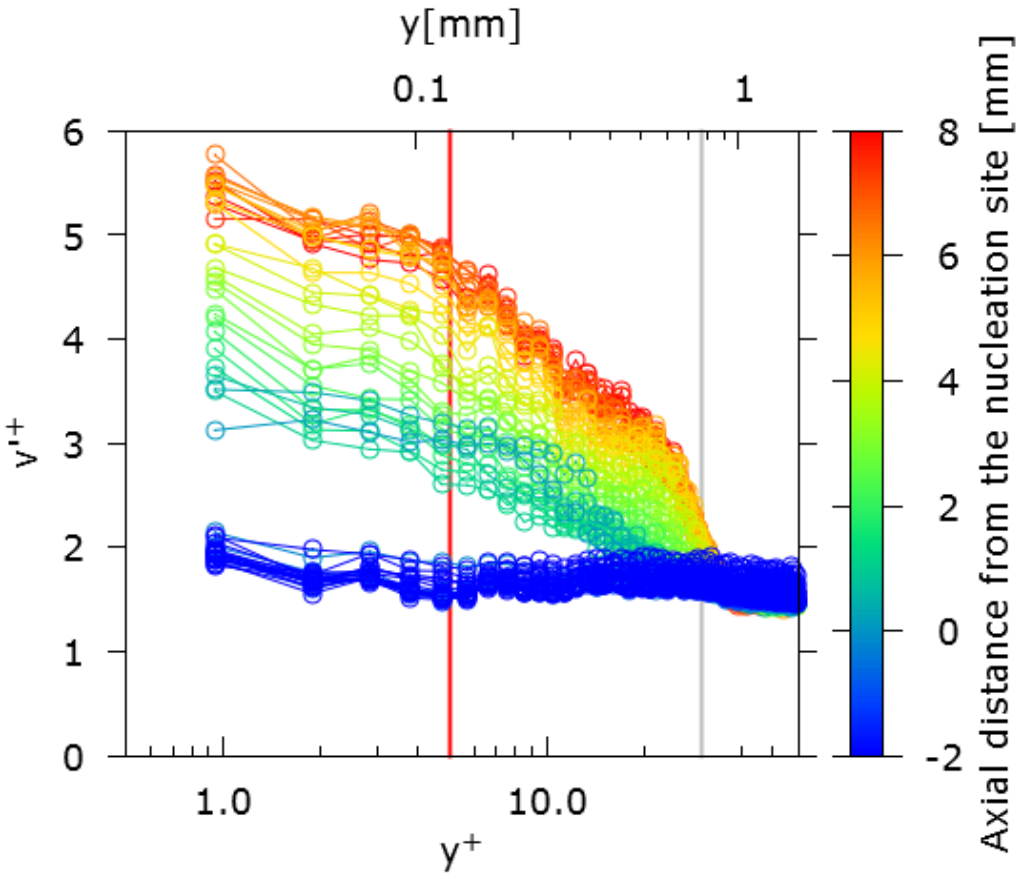

Figure 7.18: Normal turbulence intensity.

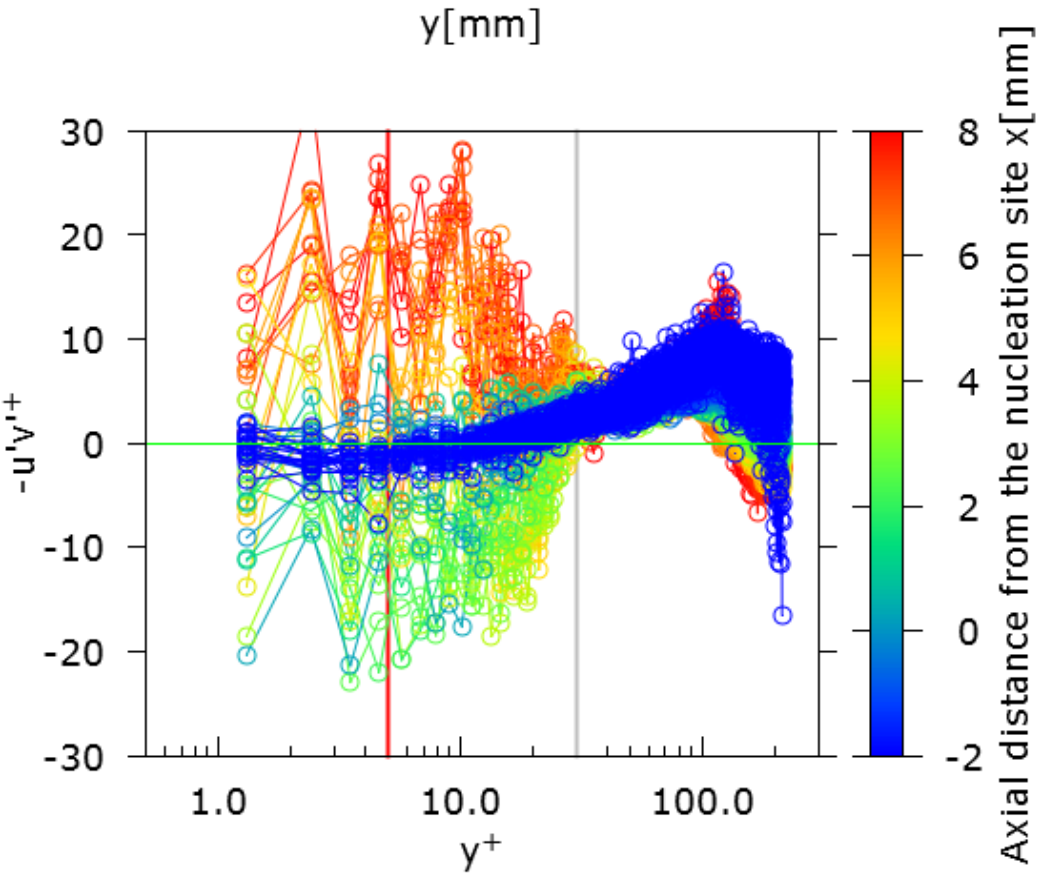

Figure 7.19: Reynolds stresses.

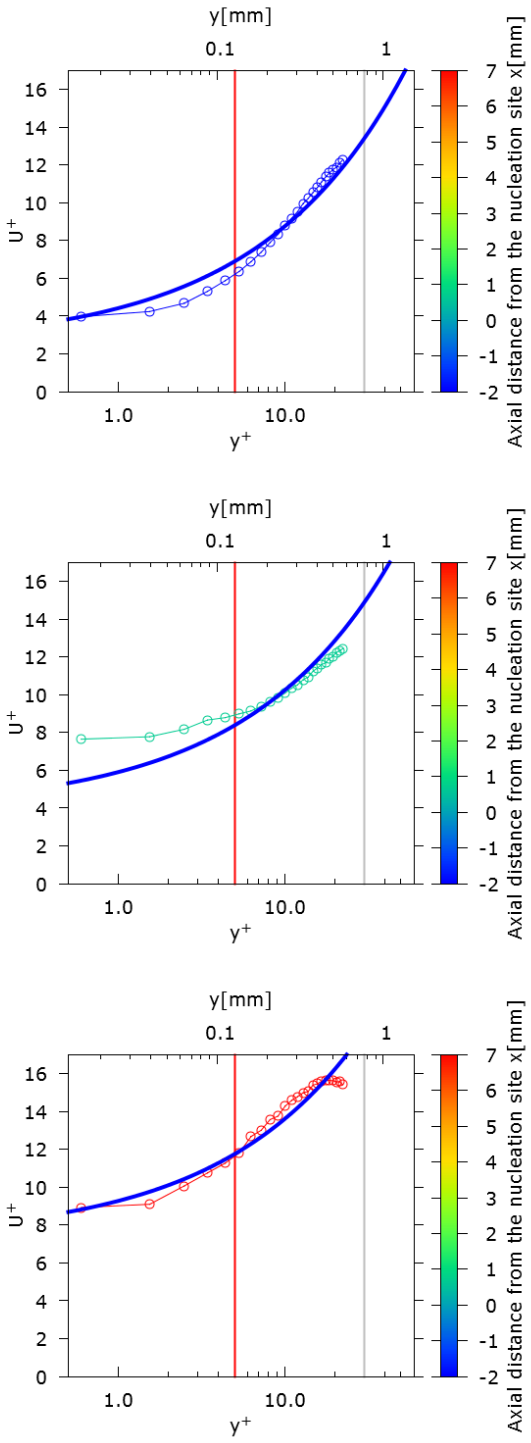

Figure 7.20: Dimensionless axial liquid velocity profile for different axial locations from the nucleation site.

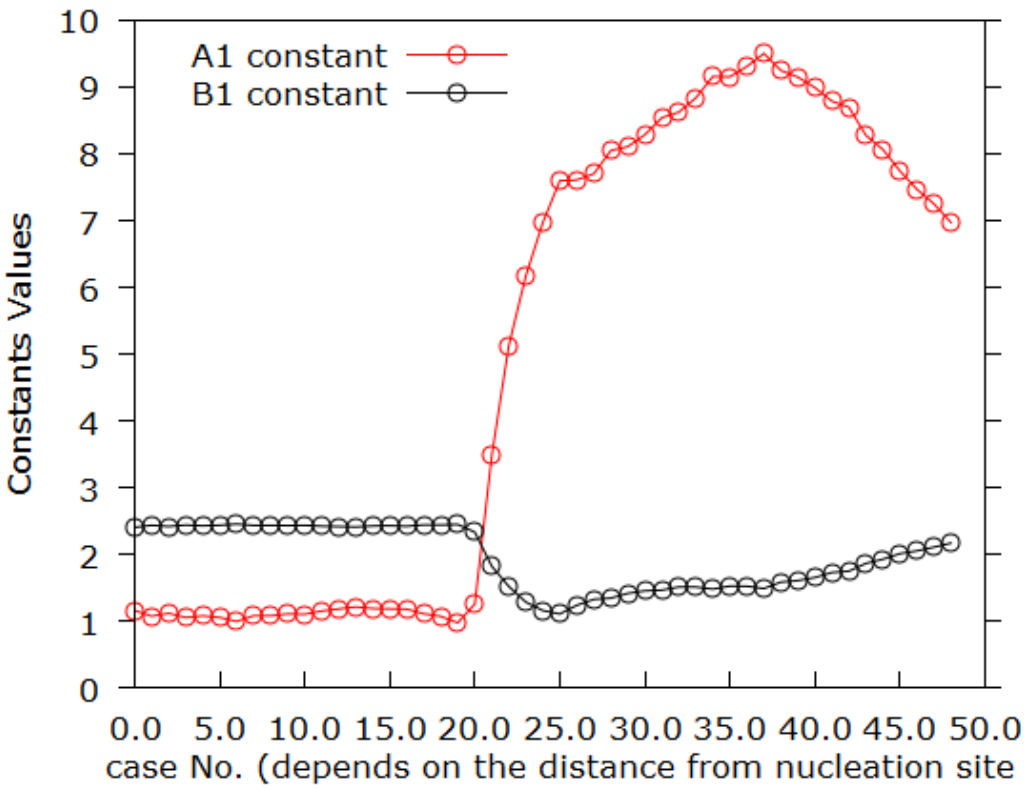

Figure 7.21: $A1$ and $B1$ estimated values from the fitting process along the heater length.

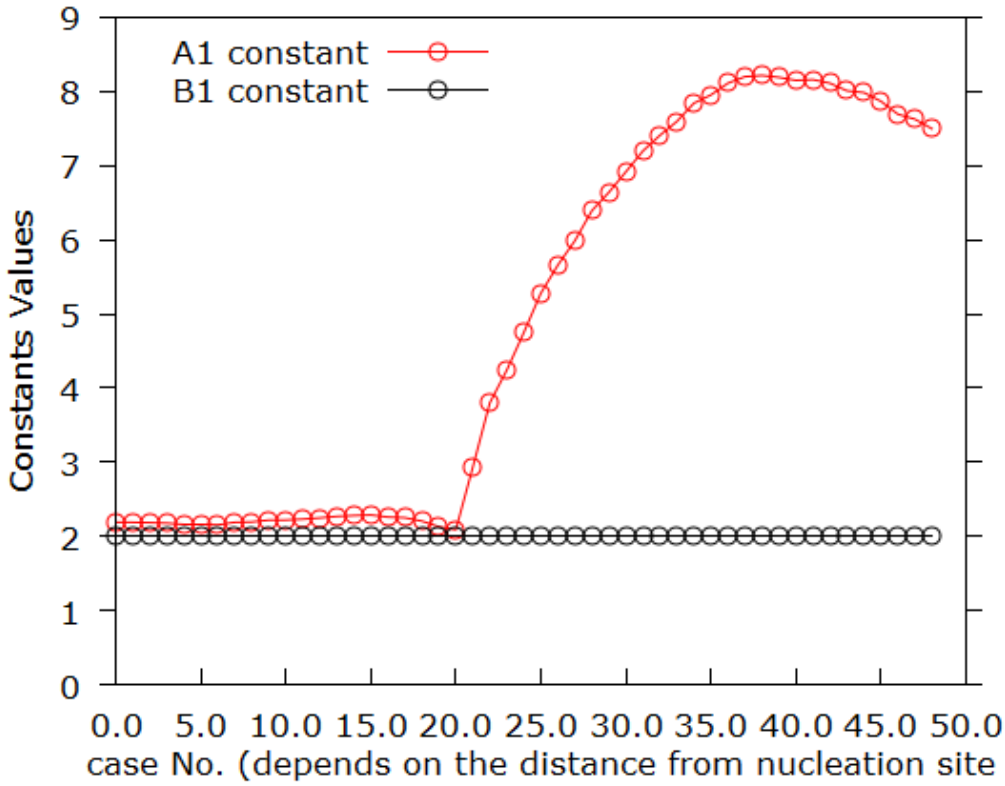

Figure 7.22: $A1$ values for the fitting process from multiple cases along the heater length, with $B1 = 2.0$.

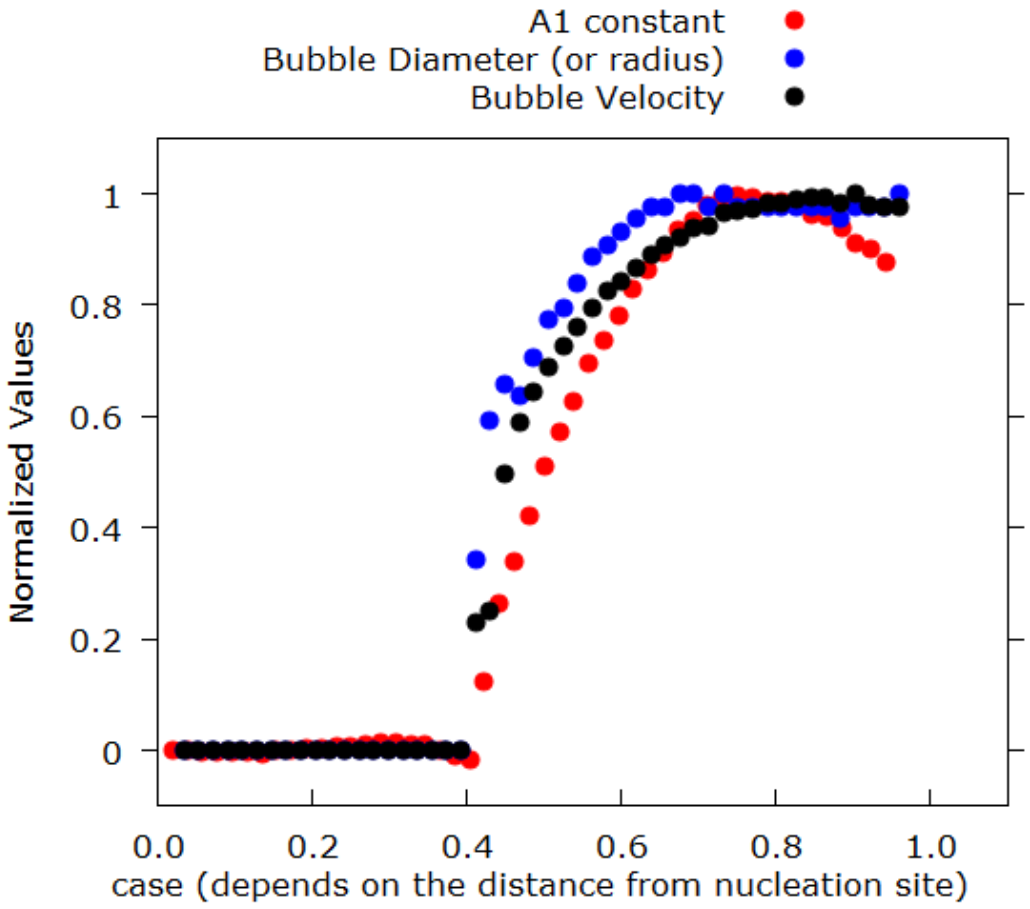

Figure 7.23: Comparison between normalized values of $A1$, r, and V_b .

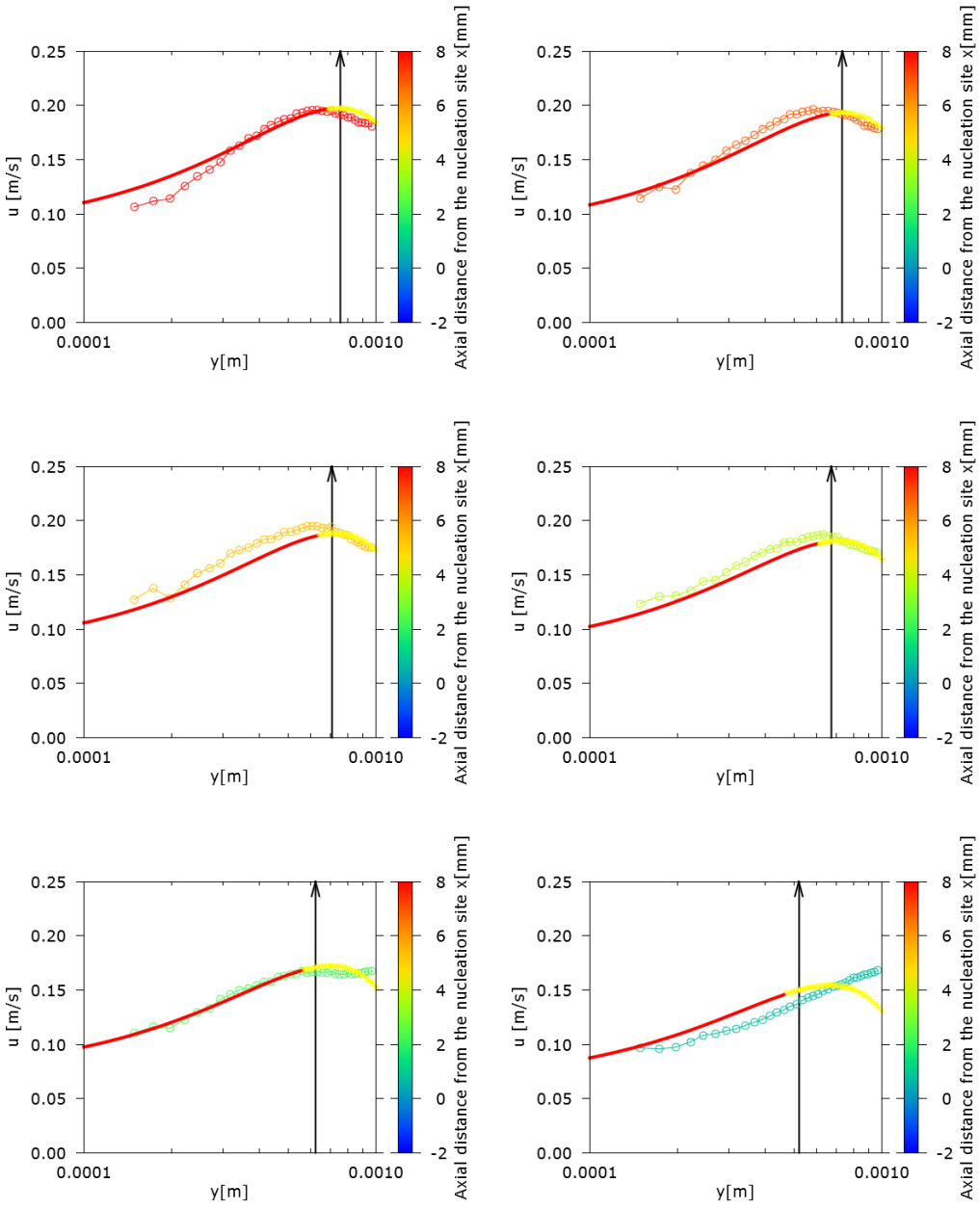

Figure 7.24: Fitting performance of Eq. 7.12.

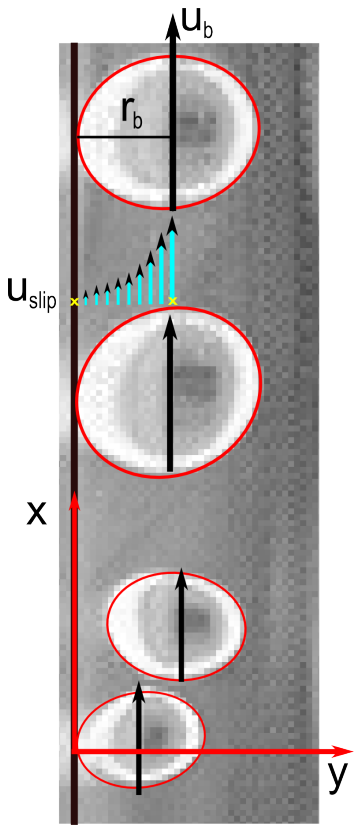

Figure 7.25: Bubbles as a moving wall.

8. CONCLUSIONS

In this work, sensitivity studies were performed to explore the feasible implementation of whole-field visualization techniques such as particle tracking velocimetry, high speed shadowgraphy, and laser induced fluorescence to study subcooled flow boiling through a vertical square channel with a single heated wall. It was found that although each independent technique requires very specific technical demands, with careful experimental system arrangements, the simultaneous implementation of these techniques to study subcooled flow boiling is viable with reasonable uncertainties and high repeatability.

From the PTV perspective several findings/recommendations are highlighted: For typical PTV boiling experiments, the use of high energy lasers in a continuous timing mode has to be used with caution. Laser induced perturbations changed what was considered a stable boiling condition.

Therefore, the use of the straddling timing mode is recommended. The straddling timing mode showed to be superior not only due to the reduced laser induced perturbations, but also provided higher quality long-term flow statistics. The straddling timing allowed more independent samples to be used on the estimation of the time average quantities. This fact was specially important for the shadowgraphy measurements due to the relatively small number of bubbles. Furthermore it is shown that bubble dynamics parameters that are normally acquired using the continuous timing mode can be estimated from the straddling results, as an example, the average bubble growth rate as a function of time was derived by combining straddling results from PTV and Shadowgraphy measurements.

The sensitivity studies performed in this work provided insight into the PTV

uncertainties, special interest was given to subcooled flow boiling conditions. It was found that other than the typical uncertainties of the technique, additional uncertainties inherent to the boiling phenomena were found. These included uncertainties due to thermo-optical distortions, which are highly dependent on position and on experimental conditions. Thermo-optical distortions manifested as a bias uncertainty β_{TOD} and by two random uncertainties σ_{TOD_ρ} and σ_{TOD_b}. The random uncertainties originate from random density fluctuations and due distortions induced by the boiling bubbles. The bias uncertainty is easily corrected by means of side experiments involving a calibration grid, the uncertainty due to random density fluctuations σ_{TOD_ρ} can not be easily corrected, but for the studied conditions did not largely affect the measurements.

It was also found that large uncertainties on the PTV measurements were induced by the boiling bubbles, therefore it is recommended to perform simultaneous PTV/Shadowgraphy experiments. The shadowgraphy experiments will dictate the bubbles domain, from which spurious velocity vectors can be removed to reduce this uncertainties.

The experimental methodology developed in this work, provided whole-field velocity fields of the two phases, bubbles dynamics quantification and heater wall temperature fields in a simultaneous manner with acceptable accuracy and repeatability.

From these results, a two-phase flow model to describe near-wall liquid velocity behavior under subcooled boiling conditions was proposed. Although this model is still in the developmental stages, it was successfully implemented to the experimental data. The proposed model depends on parameters that describe the global liquid flow conditions, and local void parameters such as bubble size and velocity.

The information in this work can be used as an experimental benchmark for

validation of CFD codes and for the improvement and development of models and correlations for a better description of subcooled boiling flow.

REFERENCES

Abdelmessih, A., Hooper, F., Nangia, S., 1972. Flow effects on bubble growth and collapse in surface boiling. International Journal of Heat and Mass Transfer 15 (1), 115–125.

Ahmadi, R., Ueno, T., Okawa, T., 2012. Experimental identification of the phenomenon triggering the net vapor generation in upward subcooled flow boiling of water at low pressure. International Journal of Heat and Mass Transfer 55, 6067–6076.

Alfredsson, P., Johansson, A., Haritonidis, J., Eckelmann, H., 1988. The fluctuating wall-shear stress and the velocity field in the viscous sublayer. Physics of Fluids 31, 1026–1033.

Antonia, R., Teitel, M., Kim, J., Browne, L., 1992. Low-reynolds-number effects in a fully developed turbulent channel flow. Journal of Fluid Mechanics 236, 579–605.

Astarita, T., Cardone, G., 2005. Analysis of interpolation schemes for image deformation methods in piv. Experiments in Fluids 38 (2), 233–243.

Beattie, D., 1972. Two-phase flow structure and mixing length theory. Nuclear Engineering and Design 21 (1), 46–64.

Bibeau, E., Salcudean, M., 1994. A study of bubble ebullition in forced-convective subcooled nucleate boiling at low pressure. International Journal of Heat and Mass Transfer 37 (15), 2245–2259.

Bruchhausen, M., Guillard, F., Lemoine, F., 2005. Instantaneous measurement of two-dimensional temperature distributions by means of two-color planar laser induced fluorescence (PLIF). Experiments in Fluids 38 (1), 123–131.

Castanet, G., Lavieille, P., Lebouché, M., Lemoine, F., 2003. Measurement of the temperature distribution within monodisperse combusting droplets in linear streams

using two-color laser-induced fluorescence. Experiments in Fluids 35 (6), 563–571.

Chaumat, H., Billet-Duquenne, A., Augier, F., Mathieu, C., Delmas, H., 2005. Application of the double optic probe technique to distorted tumbling bubbles in aqueous or organic liquid. Chemical Engineering Science 60 (22), 6134–6145.

Chaumat, H., Billet-Duquenne, A., Augier, F., Mathieu, C., Delmas, H., 2007. On the reliability of an optical fibre probe in bubble column under industrial relevant operating conditions. Experimental Thermal and Fluid Science 31 (6), 495–504.

Chen, C., Li, K., Lie, Y., Lin, T., 2011. Saturated flow boiling heat transfer of R-410A and associated bubble characteristics in a narrow annular duct. International Journal of Heat and Mass Transfer 54 (23-24), 4988–5000.

Chu, I.-C., No, H. C., Song, C.-H., 2011. Bubble lift-off diameter and nucleation frequency in vertical subcooled boiling flow. Journal of Nuclear Science and Technology 48 (6), 936–949.

Coolen, M., Kieft, R., Rindt, C., Van Steenhoven, A., 1999. Application of 2-D LIF temperature measurements in water using a Nd: YAG laser. Experiments in Fluids 27 (5), 420–426.

Coppeta, J., Rogers, C., 1998. Dual emission laser induced fluorescence for direct planar scalar behavior measurements. Experiments in Fluids 25 (1), 1–15.

Dahikar, S., Sathe, M., Joshi, J., 2010. Investigation of flow and temperature patterns in direct contact condensation using PIV, PLIF and CFD. Chemical Engineering Science 65 (16), 4606–4620.

Dominguez-Ontiveros, E., Estrada-Perez, C., Ortiz-Villafuerte, J., Hassan, Y., 2006. Development of a wall shear stress integral measurement and analysis system for two-phase flow boundary layers. Review of Scientific Instruments 77 (10), 105103.

Durst, F., Kikura, H., Lekakis, I., Jovanović, J., Ye, Q., 1996. Wall shear stress determination from near-wall mean velocity data in turbulent pipe and channel

flows. Experiments in Fluids 20 (6), 417–428.

Elsinga, G., van Oudheusden, B., Scarano, F., 2005. Evaluation of aero-optical distortion effects in PIV. Experiments in Fluids 39 (2), 246–256.

Estrada-Perez, C., 2004. Analysis, comparison and modification of various particle image velocimetry (PIV) algorithms. Master thesis, Texas A&M University, USA.

Estrada-Perez, C. E., Hassan, Y. A., 2010. PTV experiments of subcooled boiling flow through a vertical rectangular channel. International Journal of Multiphase Flow 36 (9), 691–706.

Euh, D., Ozar, B., Hibiki, T., Ishii, M., Song, C.-H., 2010. Characteristics of bubble departure frequency in a low-pressure subcooled boiling flow. Journal of Nuclear Science and Technology 47 (7), 608–617.

Feng, Y., Goree, J., Liu, B., 2007. Accurate particle position measurement from images. Review of Scientific Instruments 78, 053704.

Funatani, S., Fujisawa, N., Ikeda, H., 2004. Simultaneous measurement of temperature and velocity using two-colour LIF combined with PIV with a colour CCD camera and its application to the turbulent buoyant plume. Measurement Science and Technology 15 (5), 983–990.

Guasto, J., Huang, P., Breuer, K., 2006. Statistical particle tracking velocimetry using molecular and quantum dot tracer particles. Experiments in Fluids 41 (6), 869–880.

Gui, L., Wereley, S., 2002. A correlation-based continuous window-shift technique to reduce the peak-locking effect in digital piv image evaluation. Experiments in Fluids 32 (4), 506–517.

Günther, A., Papavassiliou, D., Warholic, M., Hanratty, T., 1998. Turbulent flow in a channel at a low reynolds number. Experiments in Fluids 25 (5), 503–511.

Hassan, Y., Blanchat, T., 1991. Flow velocity measurements using digital pulsed laser

velocimetry. Optical Engineering 30 (8), 1220–1227.

Hassan, Y., Blanchat, T., Seeley, C., 1992a. PIV flow visualization using particle tracking techniques. Measurement of Science and Technology 3 (7), 633–642.

Hassan, Y., Blanchat, T., Seeley, C., Canaan, R., 1992b. Simultaneous velocity measurements of both components of a two-phase flow using particle image velocimetry. International journal of multiphase flow 18 (3), 371–395.

Hassan, Y., Gutierrez-Torres, C., Jimenez-Bernal, J., 2005. Temporal correlation modification by microbubbles injection in a channel flow. Int. Com. Heat Mass Transfer 32 (8), 1009–1015.

Hishida, K., Sakakibara, J., 2000. Combined Planar laser-induced fluorescence–particle image velocimetry technique for velocity and temperature fields. Experiments in Fluids 29, 129–140.

Ido, T., Murai, Y., 2006. A recursive interpolation algorithm for particle tracking velocimetry. Flow Measurement and Instrumentation 17 (5), 267–275.

Johansen, J., Castro, A., Carrica, P., 2010. Full-scale two-phase flow measurements on athena research vessel. International Journal of Multiphase Flow 36 (9), 720–737.

Kähler, C. J., Scharnowski, S., Cierpka, C., 2012. On the uncertainty of digital PIV and PTV near walls. Experiments in fluids 52 (6), 1641–1656.

Karasso, P., Mungal, M., 1997. PLIF measurements in aqueous flows using the Nd: YAG laser. Experiments in Fluids 23 (5), 382–387.

Khan, A., 2012. Bubbly flow experiment in channel using an optical probe and tracking algorithm. Master thesis, Texas A&M University, USA.

Khan, A., Estrada-Perez, C., Hassan, Y., 2011. Whole-field velocity measurements of isothermal bubble plume using PTV. In: Proceeding of the 19th international conference on nuclear engineering. Available from: IAEA portal.

Kiambi, S., Duquenne, A.-M., Dupont, J.-B., Colin, C., Risso, F., Delmas, H., 2003.

Measurements of bubble characteristics: comparison between double optical probe and imaging. The Canadian Journal of Chemical Engineering 81 (3-4), 764–770.

Kim, H., Kihm, K., Allen, J., 2003. Examination of ratiometric laser induced fluorescence thermometry for microscale spatial measurement resolution. International Journal of Heat and Mass Transfer 46 (21), 3967–3974.

Kim, T., Kommer, E., Dessiatoun, S., Kim, J., 2012. Measurement of two-phase flow and heat transfer parameters using infrared thermometry. International Journal of Multiphase Flow 40, 56–67.

Klausner, J., Mei, R., Bernhard, D., Zeng, L., 1993. Vapor bubble departure in forced convection boiling. International Journal of Heat and Mass Transfer 36 (3), 651–662.

Končar, B., Matkovič, M., 2012. Simulation of turbulent boiling flow in a vertical rectangular channel with one heated wall. Nuclear Engineering and Design 245, 131–139.

Končar, B., Tiselj, I., 2010. Influence of near-wall modelling on boiling flow simulation. Nuclear Engineering and Design 240 (2), 275–283.

Koyasu, M., Tanaka, T., Sato, Y., Hishida, K., July 2009. Turbulence structure of bubbly upward flow (high spatial and temporal resolution measurements using high speed time series PTV). Transactions of the Japan Society of Mechanical Engineers (in Japanese) 75 part B (755), 1446–1453.

Lavieille, P., Delconte, A., Blondel, D., Lebouche, M., Lemoine, F., 2004. Non-intrusive temperature measurements using three-color laser-induced fluorescence. Experiments in Fluids 36 (5), 706–716.

Lavieille, P., Lemoine, F., Lavergne, G., Lebouché, M., 2001. Evaporating and combusting droplet temperature measurements using two-color laser-induced fluorescence. Experiments in Fluids 31 (1), 45–55.

Lavieille, P., Lemoine, F., Lavergne, G., Virepinte, J., Lebouché, M., 2000. Temperature measurements on droplets in monodisperse stream using laser-induced fluorescence. Experiments in Fluids 29 (5), 429–437.

Lavieille, P., Lemoine, F., Lebouché, M., 2002. Investigation on temperature of evaporating droplets in linear stream using two-color laser-induced fluorescence. Combustion Science and Technology 174 (4), 117–142.

Lavoie, P., Avallone, G., De Gregorio, F., Romano, G., Antonia, R., 2007. Spatial resolution of PIV for the measurement of turbulence. Experiments in Fluids 43 (1), 39–51.

Lee, T., Park, G., Lee, D., 2002. Local flow characteristics of subcooled boiling flow of water in a vertical concentric annulus. Int. J. Heat Mass Transfer 28 (8), 1351–1368.

Lemoine, F., Antoine, Y., Wolff, M., Lebouche, M., 1999. Simultaneous temperature and 2D velocity measurements in a turbulent heated jet using combined laser-induced fluorescence and LDA. Experiments in Fluids 26 (4), 315–323.

Lima Neto, I., Zhu, D., Rajaratnam, N., 2008. Bubbly jets in stagnant water. International Journal of Multiphase Flow 34 (12), 1130–1141.

Lindken, R., Merzkirch, W., 2002. A novel piv technique for measurements in multiphase flows and its application to two-phase bubbly flows. Experiments in fluids 33 (6), 814–825.

Marie, J., Moursali, E., Tran-Cong, S., 1997. Similarity law and turbulence intensity profiles in a bubbly boundary layer at low void fractions. International journal of multiphase flow 23 (2), 227–247.

McKenna, S., McGillis, W., 2002. Performance of digital image velocimetry processing techniques. Experiments in Fluids 32 (1), 106–115.

Mikielewicz, D., 2003. Hydrodynamics and heat transfer in bubbly flow in the turbulent boundary layer. International journal of heat and mass transfer 46 (2), 207–220.

Mudde, R., Harteveld, W., Van den Akker, H., 2008. Uniform flow in bubble columns. Industrial & Engineering Chemistry Research 48 (1), 148–158.

Natrajan, V., Christensen, K., 2009. Two-Color Fluorescent Thermometry for Microfluidic Systems. Measurement Science and Technology 20, 015401.

Nobach, H., Honkanen, M., 2005. Two-dimensional gaussian regression for sub-pixel displacement estimation in particle image velocimetry or particle position estimation in particle tracking velocimetry. Experiments in Fluids 38 (4), 511–515.

Ortiz-Villafuerte, J., Hassan, Y., 2006. Investigation of microbubble boundary layer using particle tracking velocimetry. Journal of Fluids Engineering 128, 507.

Pringsheim, P., Schulman, J., 1950. Fluorescence and phosphorescence. Physics Today 3, 35.

Rensen, J., Roig, V., 2001. Experimental study of the unsteady structure of a confined bubble plume. International journal of multiphase flow 27 (8), 1431–1449.

Revankar, S., Ishii, M., 1992. Local interfacial area measurement in bubbly flow. International journal of heat and mass transfer 35 (4), 913–925.

Ross, D., Gaitan, M., Locascio, L., 2001. Temperature measurement in microfluidic systems using a temperature-dependent fluorescent dye. Anal. Chem 73 (17), 4117–4123.

Roy, R., Kang, S., Zarate, J., Laporta, A., 2002. Turbulent subcooled boiling flow experiments and simulations. J. Heat Transfer 124, 73.

Roy, R., Velidandla, V., Kalra, S., 1997. Velocity field in turbulent subcooled boiling flow. J. Heat Transfer 119, 754.

Ruan, X., Zhao, W., 2005. A novel particle tracking algorithm using polar coordinate system similarity. Acta Mechanica Sinica 21 (5), 430–435.

Sakakibara, J., Adrian, R., 1999. Whole field measurement of temperature in water using two-color laser induced fluorescence. Experiments in Fluids 26 (1), 7–15.

Sakakibara, J., Adrian, R., 2004. Measurement of temperature field of a Rayleigh-Bénard convection using two-color laser-induced fluorescence. Experiments in fluids 37 (3), 331–340.

Sakakibara, J., Hishida, K., Maeda, M., 1997. Vortex structure and heat transfer in the stagnation region of an impinging plane jet (simultaneous measurements of velocity and temperature fields by digital particle image velocimetry and laser-induced fluorescence). International Journal of Heat and Mass Transfer 40 (13), 3163–3176.

Sathe, M. J., Thaker, I. H., Strand, T. E., Joshi, J. B., 2010. Advanced piv/lif and shadowgraphy system to visualize flow structure in two-phase bubbly flows. Chemical Engineering Science 65 (8), 2431–2442.

Sato, Y., Sekoguchi, K., 1975. Liquid velocity distribution in two-phase bubble flow. International Journal of Multiphase Flow 2 (1), 79–95.

Seüntiens, H., Kieft, R., Rindt, C., Van Steenhoven, A., 2001. 2D temperature measurements in the wake of a heated cylinder using LIF. Experiments in Fluids 31 (5), 588–595.

Situ, R., Hibiki, T., Sun, X., Mi, Y., Ishii, M., 2004. Flow structure of subcooled boiling flow in an internally heated annulus. Int. J. Heat Mass Transfer 47 (24), 5351–5364.

Stellmacher, M., Obermayer, K., 2000. A new particle tracking algorithm based on deterministic annealing and alternative distance measures. Experiments in Fluids 28 (6), 506–518.

Sutton, J., Fisher, B., Fleming, J., 2008. A laser-induced fluorescence measurement for aqueous fluid flows with improved temperature sensitivity. Experiments in Fluids 45 (5), 869–881.

Takehara, K., 1998. A study on particle identification in ptv particle mask correlation

method. Journal of Visualization 1 (3), 313–323.

Takehara, K., Etoh, T., 1999. A study on particle identification in PTV –particle mask correlation method–. J. Visualization 1 (3), 313–23.

Thorncroft, G., Klausnera, J., Mei, R., 1998. An experimental investigation of bubble growth and detachment in vertical upflow and downflow boiling. International Journal of Heat and Mass Transfer 41 (23), 3857–3871.

Troshko, A., Hassan, Y., 2001. Law of the wall for two-phase turbulent boundary layers. International journal of heat and mass transfer 44 (4), 871–875.

Udrea, D., Bryanston-Cross, P., Moroni, M., Querzoli, G., 2000. Particle tracking velocimetry techniques. Kluwer Academic Publishers, The Netherlands.

Ünal, H., 1976. Maximum bubble diameter, maximum bubble-growth time and bubble-growth rate during the subcooled nucleate flow boiling of water up to 17.7 mn/m^2. International Journal of Heat and Mass Transfer 19 (6), 643–649.

Vejražka, J., Vecer, M., Orvalho, S., Sechet, P., Ruzicka, M., Cartellier, A., 2010. Measurement accuracy of a monofiber optical probe in a bubbly flow. International Journal of Multiphase Flow.

Vejražka, J., Večeř, M., Orvalho, S., Sechet, P., Ruzicka, M. C., Cartellier, A., 2010. Measurement accuracy of a mono-fiber optical probe in a bubbly flow. International Journal of Multiphase Flow 36 (7), 533–548.

Velidandla, V., Putta, S., Roy, R., 1996. Turbulent velocity field in isothermal and heated liquid flow through a vertical annular channel. Int. J. Heat Mass Transfer 39, 3333–3346.

Westerweel, J., Dabiri, D., Gharib, M., 1997. The effect of a discrete window offset on the accuracy of cross-correlation analysis of digital piv recordings. Experiments in Fluids 23 (1), 20–28.

Willert, C., Gharib, M., 1991a. Digital particle image velocimetry. Exp. Fluids 10 (4),

181–193.

Willert, C., Gharib, M., 1991b. Digital particle image velocimetry. Experiments in Fluids 10 (4), 181–193.

Yun, B.-J., Bae, B.-U., Euh, D.-J., Song, C.-H., 2010. Experimental investigation of local two-phase flow parameters of a subcooled boiling flow in an annulus. Nuclear Engineering and Design 240 (12), 3956–3966.

Yun, B.-J., Park, G.-C., Julia, J. E., Hibiki, T., 2008. Flow structure of subcooled boiling water flow in a subchannel of 3× 3 rod bundles. Journal of Nuclear Science and Technology 45 (5), 402–422.

Zaruba, A., Krepper, E., Prasser, H.-M., Reddy Vanga, B., 2005. Experimental study on bubble motion in a rectangular bubble column using high-speed video observations. Flow Measurement and instrumentation 16 (5), 277–287.

Zhou, T., Duan, J., Hong, D., Liu, P., Sheng, C., Huang, Y., 2013. Characteristics of a single bubble in subcooled boiling region of a narrow rectangular channel under natural circulation. Annals of Nuclear Energy 57, 22–31.

Zuber, N., Findlay, J., 1965. Average volumetric concentration in two-phase flow systems. Journal of Heat Transfer 87 (4), 453–468.

APPENDIX A

NEAR-WALL LIQUID VELOCITY MODEL FOR SUBCOOLED FLOW BOILING

Multiple efforts have been focused on the development of a subcooled boiling analytical model that can predict the liquid behavior close to the heated wall. Most of the developed models use the assumption that a logarithmic law should describe the liquid behavior even in the presence of the gas phase (Končar and Tiselj, 2010; Marie et al., 1997; Mikielewicz, 2003; Sato and Sekoguchi, 1975; Troshko and Hassan, 2001). Although relative success has been obtained with these models, there is still room left for improvement. The modeling of the close to the wall liquid velocity under subcooled boiling conditions is still on a developmental stage due to the complex interaction of the parameters involved. In this work, experimental based semi-empirical models are suggested. The analysis of these semi-empirical models can led to the identification of the parameters that are required for a better modeling of subcooled boiling.

From a laminar, steady state, incompressible, fully developed channel flow, and assuming that the boiling bubbles will produce the same effect as a moving wall which induce momentum to the nearby liquid, (see Fig. 7.25), we have:

$$\mu \frac{\partial^2 u(y)}{\partial y^2} = -\rho_l f_x - \frac{\partial p}{\partial x}$$

$$\frac{\partial^2 u(y)}{\partial y^2} = -\frac{1}{\mu}\left[\rho_l f_x + \frac{\partial p}{\partial x}\right]$$

integrating

$$u(y) = -\frac{y^2}{2\mu}\left[\rho_l f_x + \frac{\partial p}{\partial x}\right] + C_1 y + C_2$$

using the first boundary condition as follows:

$u(0) = u_{slide} = C_2$

$$u(y) = -\frac{y^2}{2\mu}\left[\rho_l f_x + \frac{\partial p}{\partial x}\right] + C_1 y + u_{slide}$$

using the second boundary condition as follows:

$u\left(r_b\right) = V_b$

$$u(r_b) = V_b = -\frac{r_b^2}{2\mu}\left[\rho_l f_x + \frac{\partial p}{\partial x}\right] + C_1 r_b + u_{slide}$$

solving for C_1 we have

$$C_1 = \frac{1}{r_b}\left[V_b + \frac{r_b^2}{2\mu}\left[\rho_l f_x + \frac{\partial p}{\partial x}\right] - u_{slide}\right]$$

then

$$u(y) = -\frac{y^2}{2\mu}\left[\rho_l f_x + \frac{\partial p}{\partial x}\right] + \frac{y}{r_b}\left[V_b + \frac{r_b^2}{2\mu}\left[\rho_l f_x + \frac{\partial p}{\partial x}\right] - u_{slide}\right] + u_{slide}$$

rearranging

$$u(y) = -\frac{y^2}{2\mu}\left[\rho_l f_x + \frac{\partial p}{\partial x}\right] + V_b\frac{y}{r_b} + \frac{r_b^2}{2\mu}\frac{y}{r_b}\left[\rho_l f_x + \frac{\partial p}{\partial x}\right] - \frac{y}{r_b}u_{slide} + u_{slide}$$

$$u(y) = \frac{r_b^2}{2\mu}\left[\rho_l f_x + \frac{\partial p}{\partial x}\right]\left(\left\{\frac{y}{r_b}\right\} - \left\{\frac{y}{r_b}\right\}^2\right) + \left\{\frac{y}{r_b}\right\} V_b + u_{slide}\left(1 - \left\{\frac{y}{r_b}\right\}\right)$$

knowing that the body forces in the liquid face are given by $f_x = -g_x$

$$u(y) = \frac{r_b^2}{2\mu}\left[\frac{\partial p}{\partial x} - \rho_l g_x\right]\left(1 - \left\{\frac{y}{r_b}\right\}\right)\left\{\frac{y}{r_b}\right\} + \left\{\frac{y}{r_b}\right\} V_b + u_{slide}\left(1 - \left\{\frac{y}{r_b}\right\}\right)$$

assuming that $\left[\frac{\partial p}{\partial x} - \rho_l g_x\right]/2\mu = \xi$ =constant,

$$u(y) = \left(1 - \left\{\frac{y}{r_b}\right\}\right)\xi r_b^2\left\{\frac{y}{r_b}\right\} + \left(1 - \left\{\frac{y}{r_b}\right\}\right) u_{slide} + \left\{\frac{y}{r_b}\right\} V_b$$

simplifying in terms of the dimensionless length $\eta = y/r_b$

$$u(y) = (1 - \eta)\left[\xi r_b^2 \eta + u_{slide}\right] + \eta V_b \tag{A.1}$$

This equation can be compared with the experimental results presented in this work.